Review: Insights on Hard Carbon Materials for Sodium-Ion Batteries (SIBs): Synthesis – Properties – Performance Relationships

Camélia Matei Ghimbeu, Adrian Beda, Bénédicte Réty, Hamza El Marouazi, Alen Vizintin, Blaž Tratnik, Loic Simonin, Julie Michel, John Abou-Rjeily, Robert Dominko

To cite this version:

Camélia Matei Ghimbeu, Adrian Beda, Bénédicte Réty, Hamza El Marouazi, Alen Vizintin, et al.. Review: Insights on Hard Carbon Materials for Sodium-Ion Batteries (SIBs): Synthesis – Properties – Performance Relationships. Advanced Energy Materials, 2024, 14 (19), 10.1002/aenm.202303833 . hal-04671213

HAL Id: hal-04671213
https://univ-pau.hal.science/hal-04671213v1

Submitted on 14 Aug 2024

Review: Insights on Hard Carbon Materials for Sodium-Ion Batteries (SIBs): Synthesis - Properties - Performance Relationships

Camélia Matei Ghimbeu[1,2,3]*, Adrian Beda[1,2, 3], Bénédicte Rety[1,2,3], Hamza El Marouazi[1,2], Alen Vizintin[4], Blaž Tratnik[4], Loic Simonin[6], Julie Michel[6], John Abou-Rjeily[7], Robert Dominko[4,5,8]

[1]*Université de Haute-Alsace, Institut de Science des Matériaux de Mulhouse (IS2M), CNRS UMR 7361, F-68100 Mulhouse, France*

[2]*Université de Strasbourg, F-67081 Strasbourg, France*

[3]*Réseau sur le Stockage Electrochimique de l'Energie (RS2E), CNRS FR3459, 33 Rue Saint Leu, 80039 Amiens Cedex, France*

[4]*National Institute of Chemistry, Hajdrihova 19, 1000, Ljubljana, Slovenia*

[5]*Faculty of Chemistry and Chemical Technology, University of Ljubljana, Večna pot 113, 1000, Ljubljana, Slovenia*

[6]*Université Grenoble Alpes, CEA, LITEN, DEHT, LM 17 rue des Martyrs, 38054 Grenoble cedex 9, France*

[7] *Tiamat Energy, HUB de l'Energie, 15 Rue Baudelocque 80000 Amiens, France*

[8]*ALISTORE-European Research Institute, CNRS FR 3104, Hub de l'Energie, Rue Baudelocque, 80039, Amiens Cedex, France*

*Corresponding author:

E-mail: camelia.ghimbeu@uha.fr

Tel: + 33 (0) 3 89 60 87 43

Summary

Graphical Abstract

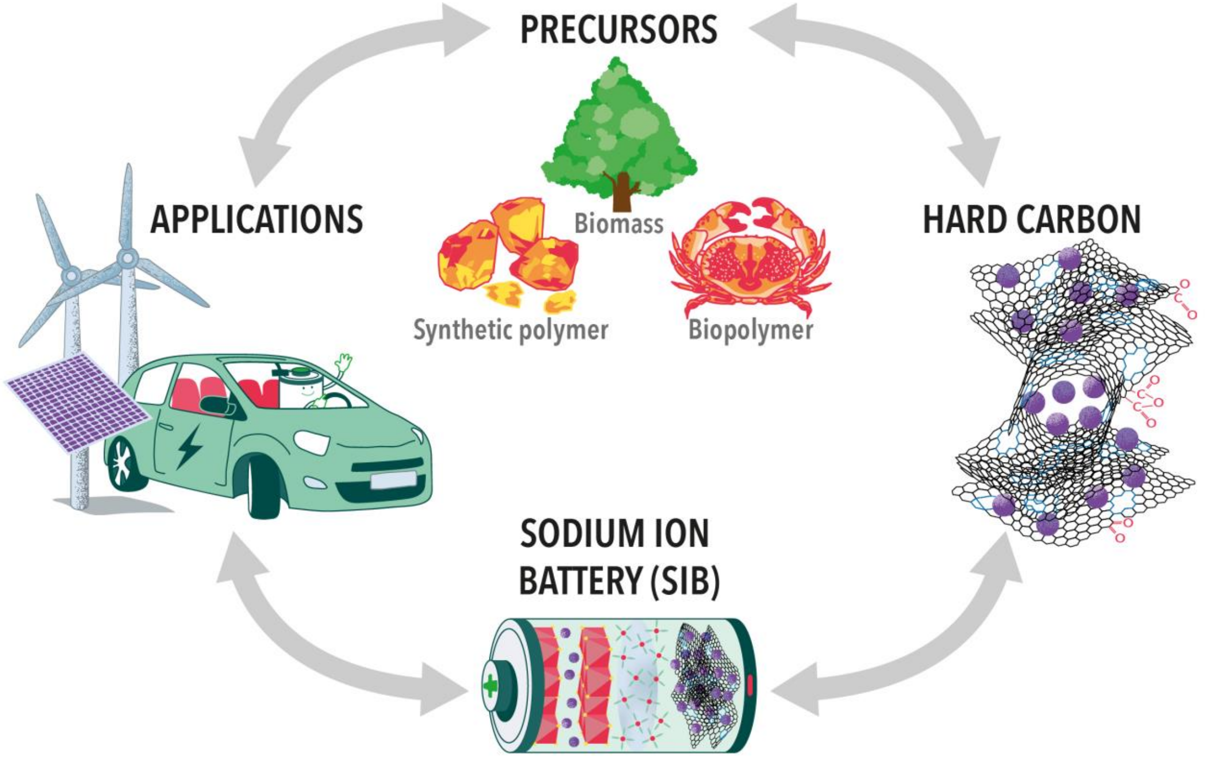

This work provides a comprehensive view of the optimal design of hard carbon anodes and the key properties to improve their performance in sodium-ion batteries (SIBs). Several synthesis-property-performance relationships are established and insights into Na-ion storage mechanisms and solid electrolyte interphase (SEI) formation are provided. The performance in full-cell devices is discussed along with the SIB prototypes and enterprises.

Abstract

Sodium ion batteries (SIBs) have attracted a significant amount of interest in the past decade as a credible alternative to the lithium-ion batteries (LIBs) widely used today. The abundance of sodium, along with the potential utilization of electrode materials without critical elements in their composition, led to the intensification of research on SIBs. Hard carbon (HC), was identified as the most suitable negative electrode for SIBs. It can be obtained by pyrolysis of eco-friendly and renewable precursors, such as biomasses and biopolymers, and synthetic polymers. Distinct HC properties can be obtained by tuning the precursors and the synthesis conditions, with a direct impact on the performance of SIBs. In this Review, an in-depth overview of how the synthesis parameters of HC affect their properties (porosity, structure, morphology, surface chemistry, and defects) is provided. Several synthesis-property relationships are established based on a database created using extensive literature data. Moreover, HC properties were correlated with the electrochemical performance (initial Coulombic efficiency and reversible capacity) *vs.* Na, in half-cells. The solid electrolyte Na-ion storage mechanisms and interphase (SEI) formation are discussed along with the HC performance in full-cell devices as well as the SIB prototypes and the history of SIBs enterprises.

Keywords: hard carbon; sustainable precursors; Na-ion batteries; capacity; efficiency;

1 Introduction

Renewable energy resources (e.g., wind, solar, and geothermal) and the implementation of zero-emission electric vehicles have gained considerable popularity over the last 5 years [1] as viable solutions to limit carbon dioxide emissions. The development of efficient, inexpensive, and improved mobile and stationary energy storage systems (ESSs) is crucial for the next step of the energy transition. The expected increase in population growth of 2 billion in the next 20 years [2] and industrial development contribute to the increased demand for ESSs. The role of batteries in the economic and environmental landscape will play a key role in the future (>2030) thanks to their potential to reduce carbon dioxide emissions by approximately 60% [3, 4] and global warming effects by 1.0 °C [5, 6].

Today, Li-ion batteries (LIBs) are considered one of the most advanced technologies for energy storage with wide applications in different fields, such as electronics, telecommunication, and transport. Taking into account different scenarios, the implementation of LIBs in zero-emission electric vehicles (EV) will significantly increase their demand by 2030 to reach an order of magnitude larger than today (Figure 1.a) [7]. In parallel, the implementation of stationary grid installations that are able to store and deliver intermittent renewable energy from solar, wind, and/or tides will also increase. Therefore, the development of both electric vehicles and stationary large-scale ESSs will play a crucial role in transport decarbonization and storage of excess renewable energy. Consequently, lithium availability is becoming a serious limitation due to a lack of resources, which has been estimated to be insufficient to satisfy the overall demands by 2030 [8]. In addition, the main battery component resources are unequally localized worldwide (e.g., 70% in non-EU countries [9]), while the depletion of cobalt (Co), copper (Cu), and graphite (G) (Figure 1.b) [10] has raised serious concern over the last decade [11],[12].

Alternative metal-based resources (LiOH *vs.* Li_2CO_3) were explored [13], along with the intensification of metal recycling after the end of battery life [14]. These pathways alone are not sufficient to fulfil future requirements. Therefore, intensive efforts to find long-lasting and sustainable alternative energy storage options for LIBs have been tremendously studied [15]. Consequently, increased efforts have been made in recent years to overcome these limitations and to find sustainable alternatives to LIBs. New technologies based on sodium (Na), calcium (Ca), zinc (Zn), or aluminium (Al) ions present many challenges, but among them, Na-ion batteries (SIBs) are considered one of the most promising [16].

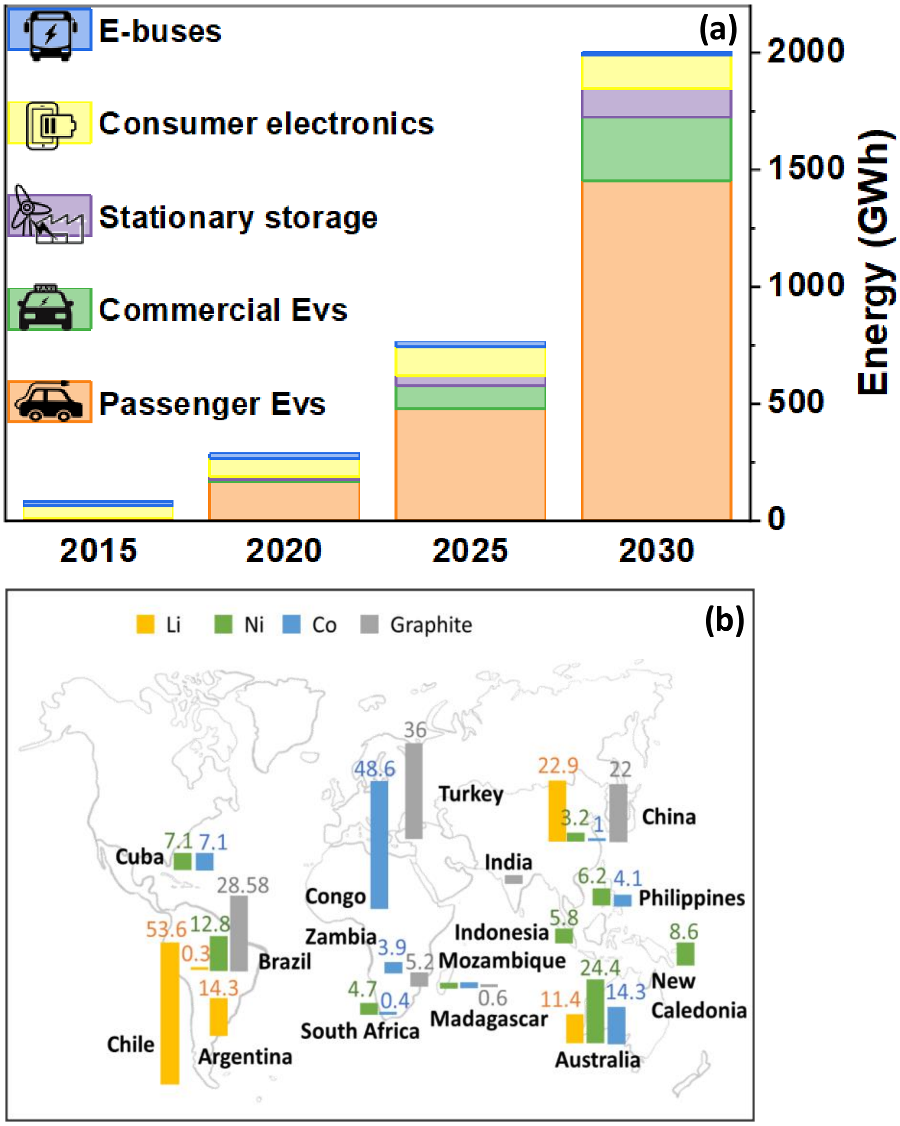

Figure 1: (a) Estimation of LIB energy demands over the next few years for different devices. Readapted from [7] *using original source: BloombergNEF Avicenne, and (b) the repartition of the main resources of battery components (Li, Ni, Co, graphite) across the world. Readapted from* [10]*, with permission, Copyright 2019, Elsevier.*

SIBs have attracted considerable attention in the last 10 years, and their development is highly motivated by the "unlimited" resources of Na in seawater and the promising electrochemical performance (see Figure 2.a) [15, 16]. The possibility of using a cheaper and lighter Al current collector (Figure 2.b) instead of Cu used in LIBs [17] is another advantage of this technology (Table 1) [17, 18]. In addition, SIBs can be discharged close to 0 V (zero energy); therefore, they are safer for transportation than LIBs [19]. On the other hand, Na^+ has a larger size compared to Li^+ (0.97 *vs.* 0.68 Å), a lower potential and lower gravimetric capacity (Table 1), which could lead to a lower energy density for SIBs than for LIBs but higher energy density than for the other technologies (Figure 2.a). Therefore, SIBs can be considered more suitable for applications where the weight requirement is less important, such as stationary grids for fluctuating renewable energy storage. These large devices require a large amount of materials, and thus, the cost and availability of the battery components involved are of paramount importance. Therefore, SIBs represent a feasible, cost-effective and long-term energy storage alternative to accompany the fossil-to-renewable energy transition.

Table 1: Advantages and limitations of Na vs. Li technologies [17, 18]

	Sodium (Na)	**Lithium (Li)**	
Distribution	Everywhere	70%, South America	**Advantages** **SIBs *vs*. LIBs**
Carbonates ($/ton)	120	4000	
Current collector ($/ton)	Al (1920)	Cu (6755)	
Cation radius (Å)	0.97	0.68	**Limitations** **SIBs *vs*. LIBs**
E^0 (V *vs*. SHE)	-2.70	-3.04	
Capacity (mAh g^{-1}), metal	1165	3829	

By shifting from LIB technology to SIB technology, the anode and cathode host materials traditionally used in LIBs are no longer efficient in SIBs. In particular, Na insertion into graphite (the common anode of LIBs) led to a low storage capacity in SIBs (31 mAh g^{-1} in carbonate ester-based electrolytes) [20] due to the weak interaction of Na with graphite [21] and its narrow graphitic interlayer space (d_{002}). By using ether-based electrolytes, the capacity of graphite can be increased (150 mAh g^{-1}) [22] due to the Na^+-solvent co-intercalation, however, the performance is still insufficient for practical applications. Consequently, other types of carbon materials have been evaluated for SIBs, such as porous carbon, graphene, doped carbon, and hard carbon (HC). The latter has gained much interest as viable anodes for SIBs due to their higher delivered capacity (~300 mAh g^{-1}). However, it remains a challenge to design sustainable and low-cost HCs that exhibit charge storage capacity with performance comparable to that of graphite anodes in LIBs (370 mAh g^{-1}) [15].

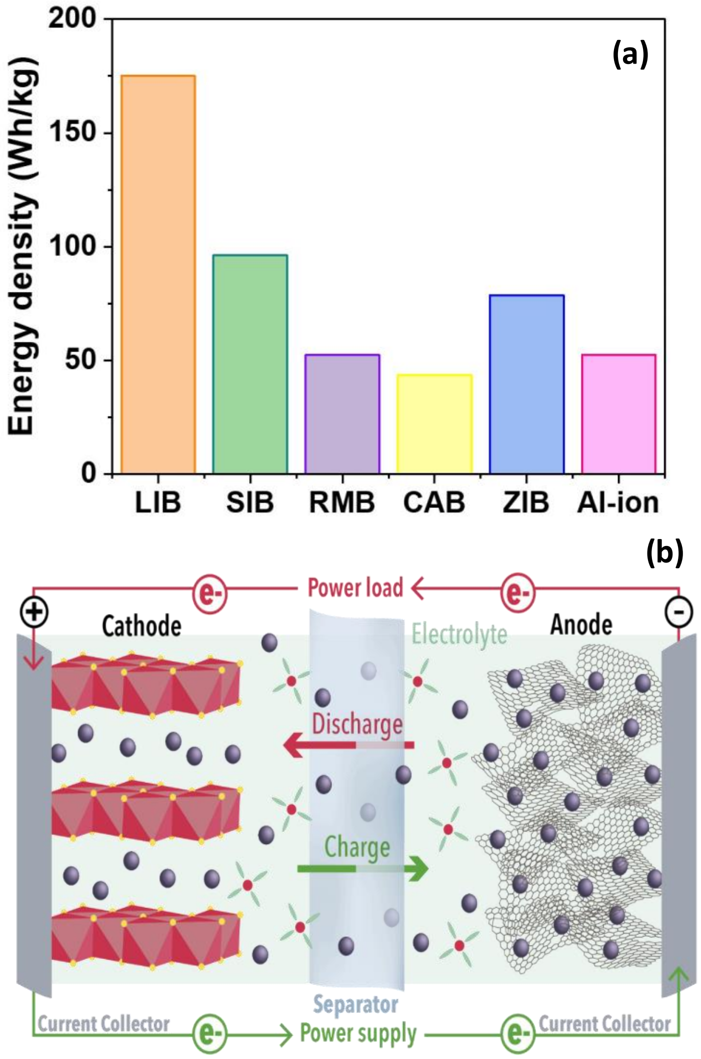

Figure 2: (a) Comparison of the energy density of LIBs with different novel battery technologies (RMB-Mg battery, SIB- Sodium ion battery, CAB-Ca battery, ZIB-Zn battery and Al-ion battery). Readapted from [16] with permission under the terms of CC BY-NC-ND 4.0 DEED licence, Copyright 2019, The Authors. Published by Elsevier B.V. and (b) scheme of a SIB, as proposed by the authors of this work.

HCs display a structure composed of a mixture of disordered and pseudo-graphitic domains that are randomly oriented, with some micropores placed between them, resembling a “house of cards”, as proposed by Stevens and Dahn [23]. They are produced by thermal pyrolysis of widely available precursors, such as biomass waste [24-27], biopolymers [28-31] and synthetic polymers [32-34]. Usually, simple pyrolysis at temperatures between 1000 and 2000 °C for a short time (one to few hours) in an oxygen-free atmosphere is sufficient to transform any of these parent materials into HCs. The lower temperature and duration of thermal treatment for the production of HC is advantageous compared to graphite (3000 °C for several weeks). Along with the eco-friendly, renewable and cheaper HC resources (biomass/waste *vs*. petrochemical for graphite), the CO_2 footprint and price of HC should be lower than graphite. However, although the CO_2 footprint is lower for HC than graphite [35, 36], the HC production market should be better developed to effectively benefit of lower cost HC, its cost being two-three times higher than graphite [37,35].

Sometimes, however, a pre- or post-pyrolysis step is required to adjust the physico-chemical properties of the final product. The choice of the parent material is often primarily dictated by its abundance and cost and secondly by its chemical composition and structure, even if the latter two have an obvious influence on the physico-chemical properties and the yield of the resulting HC. In addition, the main HC properties are significantly impacted by the applied synthesis conditions (synthesis method, pyrolysis temperature, etc.) [38-42]. Therefore, the control of hard carbon properties is of prime importance to achieve good electrochemical performance.

A good compromise between the initial Coulombic Efficiency (iCE), reversible capacity, and long-term cyclability has been determined and can be achieved only when several carbon properties are reunited. The HC graphitic interlayer space, specific surface area (SSA), closed porosity, and surface functionalities have been shown to have an important role in dictating electrochemical performance. A clear relationship between the characteristics of HCs and their electrochemical performance (versus Na metal) is difficult to draw due to the lack of “standard protocols” (a standard procedure that can be used worldwide for battery assembly and testing) among different laboratories. Moreover, despite the differences between materials used and various analytical techniques, some insightful observations have been made in the literature [40, 43-46]. In addition, Na-ion storage in HCs is still controversial, and no consensus has been found thus far. The proposed storage mechanisms include Na^+ adsorption in open pores and/or defects, Na^+ insertion between graphene layers, and/or Na^+ filling in closed pores [47, 48]. However, no common agreement has been reached on the attribution of these processes in a specific region (sloping/plateau) of the galvanostatic charge/discharge profile.

Several review articles have been published on SIBs and have focused mainly on general aspects of battery components [49-53], on state-of-the-art anodes [18, 54], or more specifically on HC materials. Regarding the hard carbon reviews, they have presented insights related to the synthesis, performance and storage mechanisms in most cases [55-58], and few have focused on specific topics, that is, hard carbon biomass [59, 60], the Coulombic efficiency of hard carbons [61] and their storage mechanisms [47]. This review attempts to provide a comprehensive view of how the synthesis conditions affect hard carbon properties and the electrochemical performance in SIBs. Several synthesis-property-performance relationships have been obtained for three classes of precursors (i.e., biomass, biopolymers and polymers) and different pyrolysis temperatures (i.e., 600-2000 °C) by studying more than 300 articles. Nevertheless, the Na-ion storage mechanisms and SEI formation are reviewed and are correlated to the hard carbon properties. The overall insights given within this review provide a clear picture of the optimal design of hard carbon anodes, of the key features of hard carbon to enhance the performance, and of further development required in this field.

2 From precursor to hard carbon

Based on many reports in the literature, hard carbons may be synthesized from a variety of inexpensive and readily available sources, which makes it economically viable and provides the opportunity to tailor its properties. These precursors can be classified into three main groups: raw biomass, biopolymers, and synthetic polymers. As shown in Figure 3.a, raw biomass dominates the precursors explored for hard carbon synthesis, accounting for 42%. This may be linked to the variety and accessibility of different wastes, such as trees, plants, and agriculture. Different publications have reported hard carbon anodes obtained from a wide variety of biomass precursors (Figure 3.b), including corn cobs [62, 63], lotus [26], various nut shells [24, 64, 65], pine [66], and different tree woods [67, 68]. However, drawbacks, such as high amount of inorganic impurities, the intrinsic complex structure, low carbon yield, and seasonal/geographical factors, make their use challenging in some cases.

The second category of resources used for hard carbon preparation, after biomass, is biopolymers, accounting for ~32%; see Figure 3.a. These sustainable precursors are used to develop innovative materials for energy storage applications. Plant-derived biopolymers, such as sucrose [69], cellulose [31], glucose [70] and lignin [71], are the main precursors used for the synthesis of hard carbons (81%); see Figure 3.c. However, animal-derived biopolymers (chitosan, chitin, gelatine) [29, 72] have also been explored but to a relatively limited extent. Generally, biopolymers have a less complex composition than biomass and lower impurity content, and in some cases, they may present a high carbon yield that can reach ~50% (in the case of lignin [30]).

The last category of precursors is synthetic polymers, at approximately 26% (Figure 3.a). The primary benefit of these precursors is their high adaptability to synthesize high-purity carbon materials at high carbon yields with regulated microstructures and morphologies.

Various synthetic polymers are used to synthesize hard carbon materials, such as pitch [73], polyvinyl chloride [74], polyacrylonitrile [75], and phenolic resin [38]. The latter alone accounts for a fifth of the polymeric precursors used for hard carbon synthesis; see Figure 3.d. The great advantage of these polymers is their high carbon yield (~ 50%) and their solubility in different solvents, which allow them to be used in wet chemistry to obtain different carbon architectures (fibres, spheres, etc.). However, most synthetic precursors have a negative environmental impact due to their petroleum-based feedstock and synthesis processes based on toxic precursors (phenol, formaldehyde). However, few reports of polymeric precursors obtained from natural resources and green synthesis routes are available in the literature [32]. If at the academic level the biosourced precursors (biomass + biopolymers) are mainly used for HC production (~ 75% based on the review study presented herein), at an industrial level the petrochemical resources (synthetic polymers) are dominant (75%) [37]. The advancements of Na-ion technology will certainly allow one to inverse this paradigm.

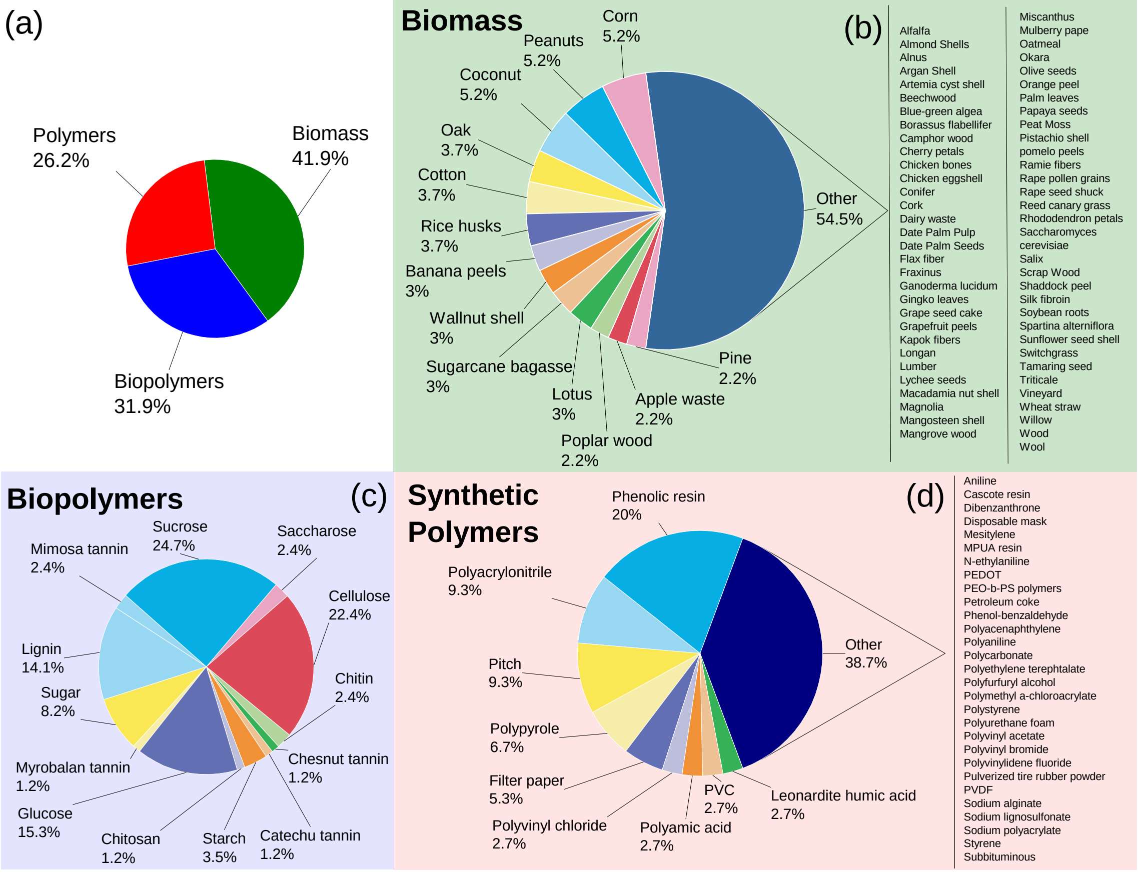

Figure 3: Graphical representation of different categories of precursors used to synthesize hard carbon materials: (a) repartition of precursors (%) into three main categories and the raw materials used in each class of precursors: (b) biomass, (c) biopolymers and (d) synthetic polymers. The % are based on the studied publications listed in the Tables 2 to 4.

From precursors to active materials, different strategies have been adapted to synthesize hard carbons depending on the precursor type and the desired final structure, morphology, and surface chemistry. The generally adopted routes for HC preparation are illustrated in Figure 4 and consist of pyrolysis processes under inert atmospheres (absence of oxygen), associated or not with a pre- and/or post-treatment. Whether on a laboratory or industrial scale, the simplest, fastest, and most economical way to obtain HCs is direct pyrolysis. The precursor source (e.g., biomass, biopolymer or synthetic polymer) is usually heated in the range of 1000-1700 °C in the presence of an atmosphere of N_2 or Ar [31, 39, 76, 77]. Some authors have reported higher pyrolysis temperatures of 2000-3000 °C [41, 75, 78, 79]. However, the carbon structure is strongly affected, and the interlayer distance d_{002} diminishes ($\leq \sim 0.34$ nm), which impedes the intercalation of Na^+ ions.

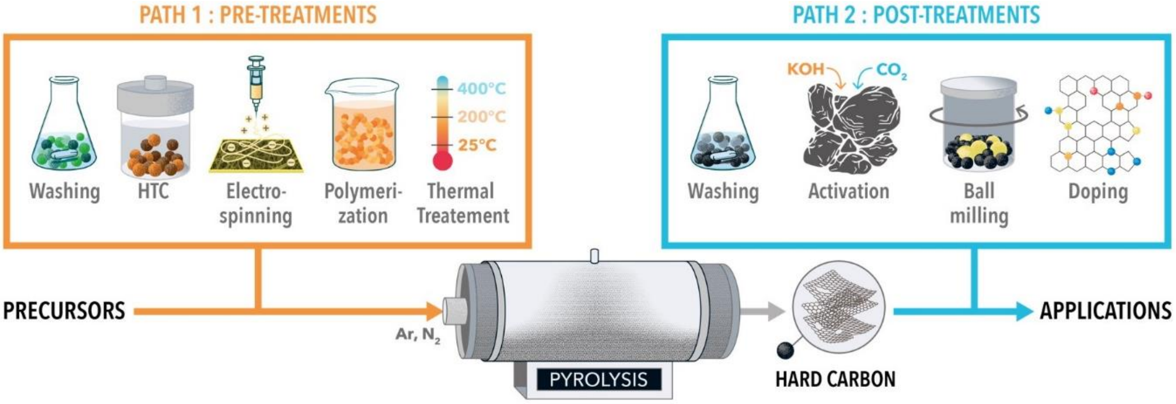

Figure 4: Schematic representation of hard carbon synthesis based on pyrolysis, pre- and/or post-treatment processes, as proposed by the authors of this work.

In addition to pyrolysis, pre- and/or post-treatments are widely applied during HC synthesis to adjust the properties of the material and thus achieve improved sodium storage. The pre-treatment process is used to control the structural, textural, chemical and morphological properties of HC, and various strategies can be adopted.

Carbon washing is one of the most common strategies used to remove inorganic and organic impurities from precursors, particularly biomass. Other pre-treatments are used to activate the carbon (increase its porosity) or dope it (introduce heteroatoms in its structure). For this purpose, acids (HCl [80, 81], H_2SO_4 [82], HF [83] and H_3PO_4 [84]), bases (KOH [64, 85], NaOH [86, 87]) and solvents (water, acetone, and ethanol) [24, 80, 88] are used alone or by combining them in different steps. For example, Dahbi et al. [24] synthesized hard carbon from argan shells and evaluated the influence of HCl acid washing pre-treatment on inorganic impurities (i.e., alkali metals and transition metals). Potassium impurities were successfully removed, while heavy metals (i.e., Ni, Co, Fe, Mn, and Zn) could not be eliminated. This treatment also leads to an increase in C-yield (from 24 wt% to 32 wt%) and specific surface area (from 2.6 m^2 g^{-1} to 24 m^2 g^{-1}). Other pre-treatments that involve HF washing on pollen [66] and rice husk [89] precursors were used to eliminate inorganic impurities from the structural composition of the obtained HC. Some greener ways to remove alkaline inorganic impurities involve the use of hot water [30]. Na-based impurities (Na_2CO_3) could be efficiently removed by this treatment and allowed at the same time a decrease in the specific surface area from 180 m^2 g^{-1} to ~6 m^2 g^{-1} and an improvement of electrochemical performance. Alkaline impurities (Na, K and Ca-based) are known to favour the activation of carbon, therefore, their removal may limit the specific surface area development during pyrolysis. Dou et al. [90] showed that prolonged acid treatment improves the hard carbon structure by creating crystalline domains at lower pyrolysis temperatures, thus reducing the synthesis costs. The authors used phosphoric acid (H_3PO_4) as a pre-treatment medium (1 to 14 days) for peanut shells, followed by pyrolysis (Figure 5.a). Longer acid treatment leads to modification of the macromolecular composition (e.g., lignin, cellulose, and hemicellulose), i.e., destruction of the basic structure of the precursor. This caused an increase in HC structural order (I_D/I_G decreased from 1.41 to 1.20 and 0.98 for 1 day, 6 days, and 14 days of treatment, respectively) and resulted in mesoporosity.

The washing step is also used as a post-treatment after the synthesis of carbon to remove impurities. Zhang et al. [91] demonstrated that post-treatment of pinecone-derived HC with an aqueous solution of KOH and then with HCl at 60 °C significantly eliminates HC inorganic impurities (Si-based) and therefore improves the C/O ratio (from ~12 to ~17). Several authors used the similar procedure of washing [92, 93] and showed effective elimination of impurities, however, their type is not mentioned. Other post-treatments have also been used involving several acids, that is, HNO_3/HCl [94] or $H_2SO_4/HNO_3/HCl$ [80].

Hydrothermal pre-treatment (or hydrothermal carbonization - HTC) is widely used to control the morphology of carbon and to avoid precursor volume expansion during pyrolysis. HTC consists of a low thermal treatment (180-230 °C) under the auto-generated pressure of a precursor dissolved or immersed in a solvent (generally water). Biopolymers, such as sucrose [95-97] and glucose [98, 99], are the most commonly used for this purpose because of their high solubility and versatility for obtaining particles with different sizes and interconnectivity. For example [100], glucose was treated at 200 °C for 12 h, followed by further pyrolysis (1000-1500 °C) and a spherical morphology (200 nm) was obtained compared to direct pyrolysis, producing irregular particles of varying sizes (Figure 5.b). Cellulose [101] and complex biomass (wood, lotus leaves, etc.) [102, 103], which are not soluble in water, have also been explored by HTC. Qatarneh et al. [102] studied the impact of various driftwood biomasses (Alnus, Conifer, Fraxinus, Populus, and Salix), HTC temperatures (180, 200 and 220 °C) and HTC residence times (4, 6 and 12 h) on the properties and performance of the resulting hydrochar and hard carbon. The produced hydrochar presented lower ash content than the raw biomass, and the C-yield and C amount were found to increase with temperature and residence time. However, the synthesis conditions did not lead to a significant difference in HC porosity or interlayer space, but primarily, differences in impurity level and morphologies were observed. The Alnus bark material which has the highest amount of impurity ($CaCO_3$ and CaC_2) presented the lowest performance *vs.* Na^+/Na, while the others reached a capacity of ~300 mAh g^{-1} at C/10. Zheng and coauthors [104] used a holly leaf precursor by HTC at 160 °C for 10 h followed by a pyrolysis step at 800 °C. This led to larger open nanopores (1.1 nm) compared to directly pyrolyzed precursors (0.5 nm) and improved Na-ion storage capacity.

Another synthesis pathway explored is electrospinning. Typically, a solution of polymer is passed through a metallic needle submitted to a high voltage (15-20 kV), which allows one to obtain a polymer film with fibrous morphology. One of the most widely used polymers is polyacrylonitrile (PAN) dissolved in N,N-dimethylformamide. Zhao et al. [105] used the PAN polymer and fulvic acid to fabricate electrospun hard carbon nanofibers in a pyrolysis range between 800 and 1500 °C. The material made at 1300 °C had the highest reversible sodium capacity (248 mAh g^{-1} at 100 mA g^{-1}). They associated these results with the rich oxygen functional groups, large interlayer spaces, and stable morphologies compared to those of other materials. In another work [75], PAN was used to obtain binder-free and self-standing HC films in a wide temperature range of 650 °C to 2800 °C. It is worth mentioning that PAN polymers require a stabilization step at low temperature (~ 200-300 °C) prior to the pyrolysis step to increase cyclization and avoid the melting of PAN during the thermal treatment. The authors studied the Na-ion mechanisms in these materials and identified three distinct mechanisms, depending on the temperature range. At low temperature (650-950 °C), adsorption mechanisms with O and N functional groups, active sites and porosity are predominant; at intermediate temperature (1100-1550 °C), a combined mechanism based on adsorption and insertion between graphene layers has been proposed, while at high temperature (2000-2800 °C), a close pore filling mechanism has been suggested. The best temperature range was found to be the intermediate range since it allows the benefit of two mechanisms, i.e., adsorption and insertion. Ding et al.[106] combined a PAN polymer with melamine (Figure 5.c) to obtain a flexible carbon nanofabric with high performance in SIBs that was suitable for the development of wearable devices. Bai et al. [74] used polyvinyl chloride (PVC) in tetrahydrofuran and dimethylformamide solvents to prepare PVC nanofibers at 600−800 °C. The materials delivered a higher reversible capacity (271 *vs*. 206 mAh g^{-1}) and higher initial Coulombic efficiency (69.9% *vs.* 60.9%) than materials obtained by direct pyrolysis of PVC. Furthermore, good cycling stability and rate performance were demonstrated by the electrospun HC. Another approach involved the use of electrospinning to synthesize polycaprolactone nanofibers, which served as a template to obtain N-doped hollow porous carbon nanofibers, through the polymerization of polycaprolactone and polypyrrole [107]. The as-prepared material exhibited a reversible capacity of 160 mA h g^{-1} after 100 cycles at a current density of 0.05 A g^{-1}.

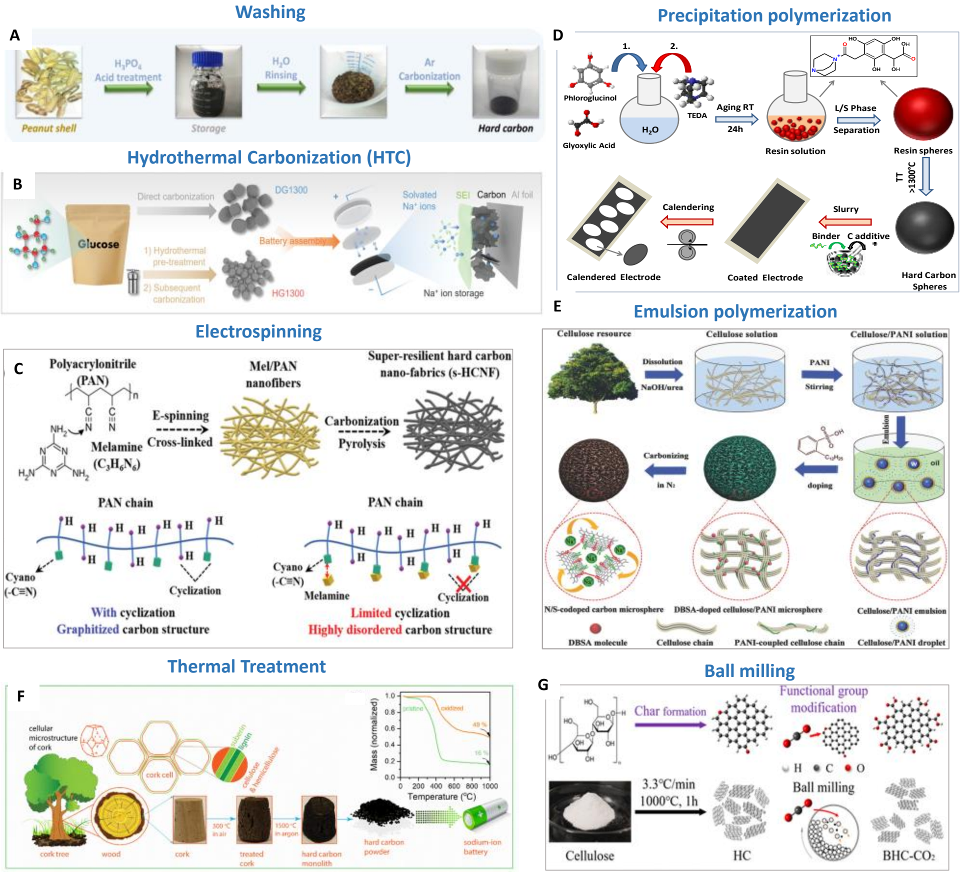

Figure 5: Schematic representation of the main classes of pre-treatments and post-treatments used for hard carbon synthesis: (a) washing, reproduced with the permission from [90], Copyrights 2018, John Wiley and Sons, (b) hydrothermal carbonization, reproduced from [100] under the terms of CC BY 4.0 DEED licence, Copyright 2022, The Authors. Published by Wiley-VCH GmbH, (c) electrospinning, reproduced with the permission form [106], Copyrights 2020, John Wiley and Sons, (d) precipitation polymerization, reproduced with the permission from [98], Copyrights 2021, Royal Society of Chemistry (e) emulsion polymerization, reproduced with the permission from [108], Copyrights 2016, John Wiley and Sons, (f) thermal treatment, reproduced under the terms of CC BY 4.0 DEED licence [109], Copyright 2022. The Authors. Published by Elsevier B.V. and (g) ball milling, reprinted with permission from [110]. Copyright ~~(~~2019~~)~~, American Chemical Society.

Polymerization reactions have also been widely explored for hard carbon synthesis. The approach most often involves the synthesis of phenolic resins. Hasegawa et al. [111] used a sol-gel process to synthesize resorcinol-formaldehyde (RF) gels and subsequently thermal pyrolysis at high temperature (800–3000 °C) to obtain hard carbon materials. The initial Coulombic efficiency was significantly increased between 800 and 1600 °C and then remained stable at a high value (~ 92%) at elevated temperatures. The authors explained that the higher temperature renders hard carbons less porous and defective, which effectively improves the initial CE. The reversible capacity increases to ~ 350 mAh g^{-1} up to 2000 °C and then decreases significantly at 2500 and 3000 °C. Using similar RF resins, the same authors fabricated binder-free monolithic electrodes with tuned macropore sizes by varying the volume of ethanol solvent in the reaction mixture [79]. They showed that improvement of the initial Coulombic efficiency requires a decrease in the surface area related to mesopores and macropores. Qiu et al. [46] used phenol with formaldehyde polymerization in the presence and absence of a soft template (Pluronic F127) to obtain nonporous and micro-mesoporous carbon. They observed different electrochemical behaviours; a sloping and plateau region was observed in the galvanostatic charge discharge for nonporous material, and a sloping region was observed only in the case of porous carbon. Based on these results, they concluded that the plateau region is not related to the Na filling of pores. Wang et al. [112] synthesized codoped hard carbon phosphorus/sulphur using a resorcinol-formaldehyde resin, a hard silica sacrificial template, and P-red and S powders as doping agents. The materials showed high Na-ion storage performance, i.e., a high iCE of 88.7%, a high-reversibility capacity of ~ 450 mA h g^{-1} after 140 cycles at 0.2 A g^{-1} and long-term cycling stability of 276 mA h g^{-1} after 3000 cycles at 10 A g^{-1}. The doping of S increased the interlayer spacing of graphite, while the doping of P promoted the formation of C-S-P and P-O bonds, which can contribute to abundant structural defects, and the presence of redox reaction sites contributes to capacitive reactions at a high rate and stability.

Some works reported the use of phenol-formaldehyde phenolic resin followed by a pre-oxidation treatment in air at low temperatures (<300 °C) before the pyrolysis step [113, 114]. This treatment allows better cross-linking of the phenolic resin and, therefore, a lower specific surface area of the resulting HC but also introduces several oxygen functionalities, which lead to a more disordered structure and larger graphitic interlayer space. These properties induced improved Na-ion storage performance. As most phenolic resin synthesis relies on toxic phenol or formaldehyde precursors, much greener precursors, such as phloroglucinol, tannin and glyoxylic acid, have been proposed (Figure 5.d), with obtained hard carbon materials showing high performance *vs.* Na^+/Na (~ iCE of ~92% and reversible capacity of ~300 mA h g^{-1} at C/10) [32, 98, 115].

Other polymers, such as polyaniline (PANI), have also been used to obtain hard carbon materials. Cao et al. [116] synthesized hollow carbon nanowires through the pyrolysis of a hollow polyaniline (PANI) nanowire precursor. The latter was obtained by polymerization and self-assembly of aniline molecules with DL-tartaric acid micelles, which acted as a sacrificial template. The material delivered a reversible capacity of 251 mAh g^{-1} *vs.* Na^+/Na and a capacity retention of 82.2% over 400 cycles. The good Na-ion insertion was associated with the short diffusion distance provided by the carbon nanowire and the large interlayer distance (0.37 nm) between the graphitic sheets. Based on theoretical calculations, the authors concluded that such an interlayer distance ensures Na-ion insertion in carbon materials. In another work [117], polymerization of aniline in the presence of a calcium carbonate ($CaCO_3$) template, followed by acid washing and carbonization, resulted in the formation of nitrogen-rich mesoporous carbon. The as-obtained material delivered a higher capacity **(**338 *vs.* ~213 mAh g^{-1} at 30 mA g^{-1}) and better iCE (54.2% *vs.* 49.6%) compared to its counterpart prepared in the absence of $CaCO_3$. The better sodium storage performance of the nitrogen-rich mesoporous carbon was attributed to the disordered structure having a large interlayer distance, the interconnected porosity, and the richer surface chemistry in nitrogen. N/S co-doped carbon microspheres were obtained using cellulose/PANI precursors *via* an emulsion polymerization pathway (Figure 5.e) in the presence of dodecyl benzene sulfonic acid (DBSA), which served as the S-source [108]. The N and S heteroatoms induced defects and expanded the interlayer space in the carbon structure, favouring Na storage. Therefore, a high capacity (280 mA h g^{-1} at 30 mA g^{-1}) and long cycle life of more than 3000 cycles has been reported for such materials. Petrochemical-derived Pitch was also used for the synthesis of hard carbon; however, pre-oxidation treatments or mixtures with precursors containing oxygen (lignin, phenolic resin, reduced graphite oxide) have been used to avoid the graphitization of pitch and formation of soft carbon [118-121].

In several works, thermal pre-treatments, such as oxidation [84, 109, 122], pre-carbonization [94, 123], and dehydration [28, 124], have been explored to modify the carbon properties (interlayer space, functionalities, and porosity), to increase the C-yield, or to avoid expansion of the precursor during the pyrolysis step (Figure 5.f).

Most post-treatments involve washing with different chemicals to remove inorganic impurities (alkali and transition-metal based: carbonates, hydroxides and oxides), as described above. Other treatments, such as activation, intend to increase the porosity of the carbon. Chemical activation (KOH) [125] and physical activation (with CO_2 and air) [28, 126] are used for this purpose. Using a sucrose precursor and activation process with CO_2 under different conditions, Bommier et al. [28] obtained a series of porous materials that showed evidence of a relationship between the porosity (BET surface area and pore volume) and the reversible/irreversible capacity. Therefore, higher reversible and lower irreversible capacities are achieved when the porosity measurable by N_2 adsorption is low. Indeed, other studies have shown low iCE (50-65%) when the carbons are activated and possess a high specific surface area.

Ball milling is often employed as a post-treatment to reduce the particle size of HC to be suitable for electrode preparation [127, 128]. However, the impact of such treatment on the performance of SIBs has been rarely studied. For example, the effect of ball milling time at a constant speed of 500 rpm on the porosity of HC and the performance of SIBs was investigated [129]. The authors measured a significant increase in open porosity and a decrease in closed porosity with an increase in ball milling time, which therefore showed a decrease in reversible Na^+ storage. In addition, Zr-based impurities that came from the jar were found to increase with milling time. Ball milling at 500 rpm with dry ice (CO_2) was used to modify the hard carbon oxygen-based functionalities (Figure 5.g) [110]. The amount of oxygen was significantly increased (from 12.1 to 19.3 at. %); in particular, carboxylic acid groups were introduced, and this had a positive impact on the reversible capacity, which increased compared to the unmodified material. However, iCE is still low for practical applications (~ 40%).

The carbon yield is a key parameter in the precursor selection for hard carbon development in terms of cost, synthesis time, efficiency, and sustainability. It represents the proportion of carbon derived from a certain precursor after thermal treatment under an inert atmosphere (i.e., Ar, N_2 or vacuum). The most common method used to determine the C-yield is thermogravimetric analysis (TGA). This technique provides information on precursor conversion into carbon by monitoring the mass change as a function of temperature under a controlled inert atmosphere. According to Dou et al. [130], during thermal annealing, the precursors undergo different chemical reactions that occur at various temperatures, including evaporation, condensation, dehydrogenation, H transfer, and isomerization. Depending on the temperature at which these reactions take place, three decomposition domains have been reported mainly in the literature [131, 132]. The first weight loss occurs at low temperature (up to 150 °C), related to solvent and/or moisture evaporation. The second region at approximately 400 °C, known as the pyrolysis phase, corresponds to the decomposition of precursors and the release of volatiles and is characterized by high weight loss. The third region, at higher temperatures (above 600 °C), where the mass loss becomes approximately constant, is associated with oxygen-/nitrogen-based functional group desorption, hydrogen removal and structural reorganization. As shown in Figure 6, the final C-yield is highly dependent on both the macromolecular composition of the precursors (i.e., biomass (Figure 6.a), biopolymers (Figure 6.b) or synthetic polymers (Figure 6.c), as well as on the pyrolysis temperature, especially for biomass precursors (Figure 6.a). Another way to determine the C-yield, in particular, at high temperatures (1400 °C to 1600 °C) difficult to assess by TGA, is by weighing the sample before and after pyrolysis. Using this approach, higher carbon yields are generally obtained from biopolymers and synthetic polymers (18 to 40 *wt.* %) compared to biomass precursors (18 to 35 *wt.* %); see Figure 6.

Wang et al. [25] observed a decrease in C-yield from 54.7 to 31.8 *wt.*% when increasing the pyrolysis temperature from 800 °C to 1600 °C for the mangosteen shell precursor. A similar effect was observed when rice husks were used as hard carbon precursors [133]. In this case, an increase in temperature from 900 °C to 1600 °C reduced the carbon yield from ~30 to 20 *wt.*%. Furthermore, Rios et al. [44] explained that a lower carbon yield for the biomass precursor can be attributed to the lower C/O ratio and the presence of large amounts of intrinsic impurities, such as Na, Si, Zn, Mg, and Cl. In particular, a higher degree of ash (i.e., the inorganic residue resulting after combustion) indicates that the precursor has a significant amount of impurity and therefore a low carbon content after pyrolysis [134], [135]. Moreover, during the pyrolysis process, high oxygen functionalities (such as –OH and R–O–R′ groups) with lower C/O ratios breakdown more easily, resulting in a lower carbon yield due to the volatile by-products they produce. Susanti et al. [136] attributed this behaviour to the lower bonding energies of the oxygenated functionalities compared to C=C aromatic bonds. Importantly, such impurities (functional groups and/or metal-based impurities) can affect the process cost, the environment (i.e., CO_x emission) and the application for which the HC is intended, i.e., irreversible reactions with Na^+ [137]. Unlike biomass resources, the C-yield resulting from the pyrolysis of biopolymers and synthetic polymers is less affected by the pyrolysis temperature. Wu et al. [83] found constant values while heat-treating lignin (44 *wt.*%) and microcrystalline cellulose (12 *wt.*%) biopolymers in the temperature range of 1000 °C to 1600 °C. The same behaviour was reported by Beda et al. [98] for a heat-treated phenolic resin polymer in the range 1300-1600 °C (~40 *wt.*% C-yield). However, the authors noticed that the C-yield highly depends on the synthesis conditions. For example, the resin obtained using ethanol as a solvent led to a higher C-yield than when water was used (~33 *vs.* 31 wt%), while drying in an oven was more efficient than freeze-drying to achieve higher C-yields (~33 *vs.* ~25 wt%).

(a) Biomasses

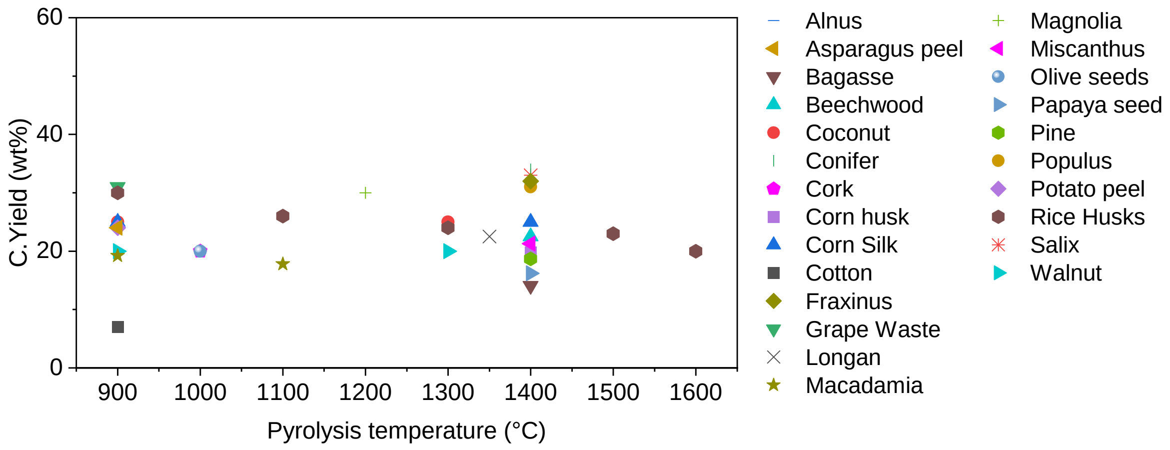

(b) Biopolymers

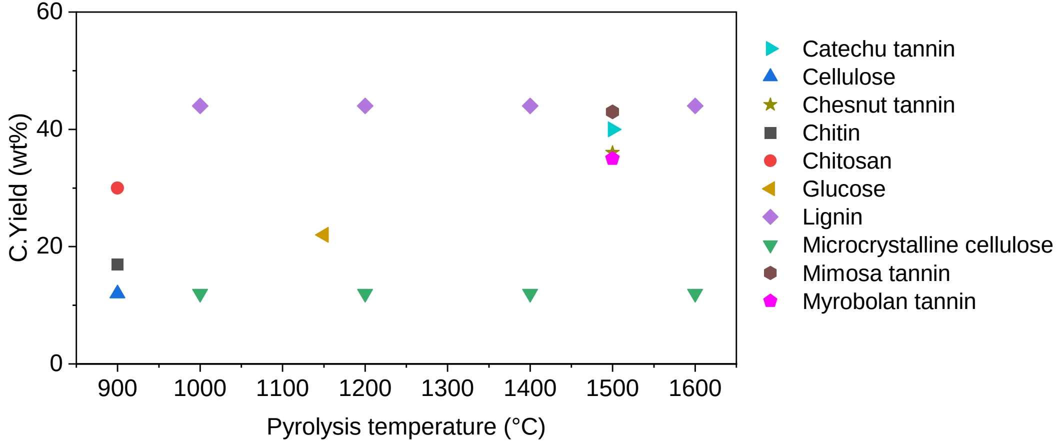

(c) Synthetic polymers

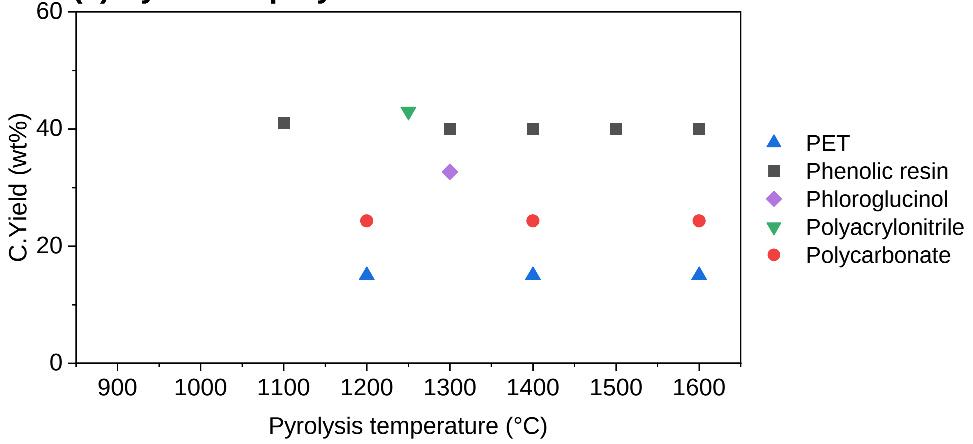

Figure 6: Carbon yield obtained by pyrolysis of several types of precursors by weighing the sample or by TGA analysis: (a) biomass-based precursors, (b) biopolymers and (c) synthetic polymers. The graphs were built based on the references presented in Tables 2 to 4.

3 Relationship between synthesis parameters and hard carbon properties

Several parameters are known to affect the formation of hard carbon and its properties (i.e., morphology, structure, chemical composition (heteroatoms/impurities), etc. Among them, the precursor type, pyrolysis conditions, and synthesis pathways have been reported to have a considerable impact on the HC properties. Therefore, the next section aims to provide an overview of how the main carbon properties are affected by the synthesis conditions and the precursor types. The literature review focuses on the three main classes of precursors: biomass, biopolymers, and polymers.

3.1 Hard carbon morphology

Generally, a hard carbon derived from a given precursor preserves its natural morphology. Many hard carbon morphologies, from (0D) to (3D) structures, including nanoparticles [138], spheres [139], nanosheets [140], nanofibers [141], and porous carbon structures [92], have been reported using different precursors and/or altering the synthesis procedures. However, the majority of explored natural precursors do not have a particular morphology, and a random-like shape is usually obtained.

To obtain (0D) to (3D) morphologies, specific synthesis routes are applied to help shape the precursor prior to the pyrolysis process, or the precursor already has an inherent specific morphology. Among (0D) architectures, the spherical shape is particularly interesting for hard carbons. Here, the synthesis route (HTC, polymerization, etc.) is more important than the precursor type. Spherical particles can be obtained by a hydrothermal method by using different hard carbon sources, such as natural biopolymers and synthetic polymers (e.g., glucose [142], sucrose [143], phenolic resin [144]) with good control over the particle size and shape. The precursor type, solution concentration, and temperature/time/pressure used have a strong impact on tuning the sphere properties. For example, Wang and co-authors [144] synthesized spherule-shaped hard carbon with a particle size of 1 to 8 µm from phenolic resin using HTC (500 °C for 12 h), followed by pyrolysis (800 °C to 1500 °C for 3 h, under N_2 flow). Väli et al. [142] reported a similar 2-step procedure to prepare HC spheres. Specifically, the glucose precursor was first pre-treated by HTC at 180 °C for 24 h and then pyrolysed at 1100 °C for 2 h under Ar flow. As a result, linked micrometre-sized carbon spheres (approximately 3 µm) with restricted size distribution and smooth surfaces were formed. In another study, Pol et al. [139] synthesized spherical carbon particles (4 ± 0.3 µm) using an autogenic decomposition process in a sealed autoclave (700 °C, 33.1 bar) under argon by using either mesitylene or polyethylene precursors (see Figure 7.a). The authors highlighted the advantages of spherical HCs when used as host materials for SIBs: high energy density, minimization of SEI build-up, and optimization of electrolyte consumption due to their regular morphology and edge-free structure. In some cases, the HTC of the biomass (e.g. Fraxinus driftwood biomass) [102] leads to some spherical particle formation, but the morphology is more heterogeneous, in particular, because solid precursors with complex structures are used.

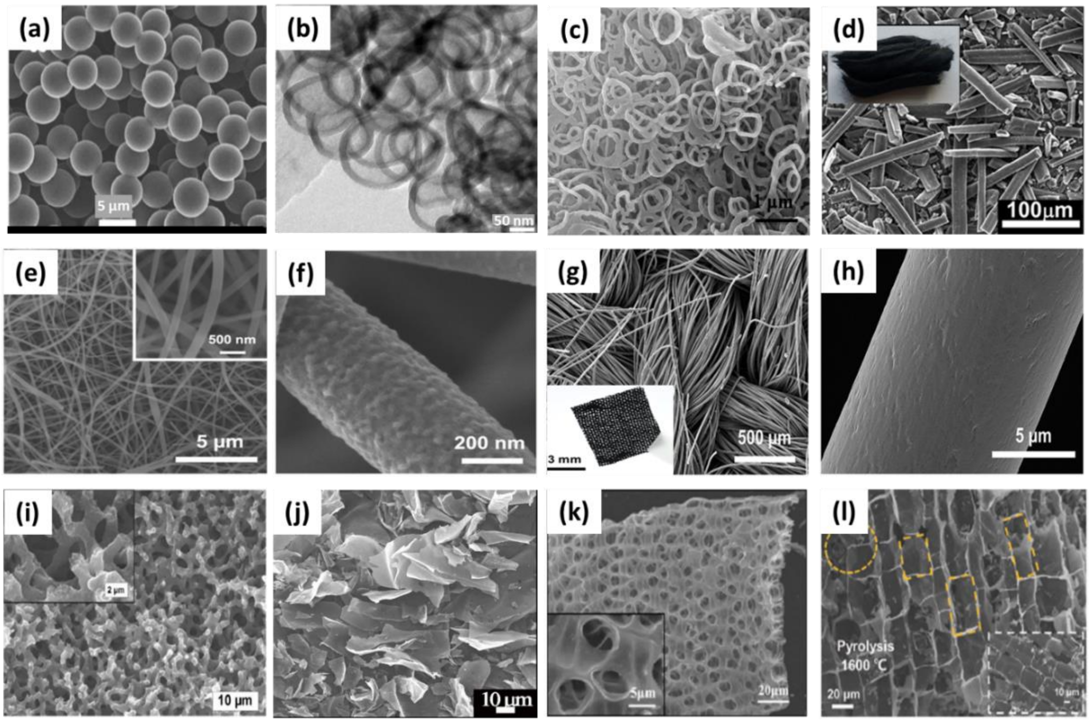

Figure 7: SEM images of hard carbons exhibiting different morphologies: (a) sphere-like, Reprinted with permission from [139], Copyright 2014, Elsevier (b) TEM image of hollow spheres, Reprinted with permission from [145] Copyright 2012, John Wiley and Sons, (c) twisted microfibers, Reprinted with permission from from [146], Copyright 2012, Elsevier, (d) unwoven microfibers, Reprinted with permission from [86], Copyright 2016, Elsevier (e)-(f) unwoven nanofiber-like, Reprinted with permission from [147], Copyright 2016, John Wiley and Sons, (g)-(h) woven microfibers, Reprinted with permission from [78], Copyright 2019, American Chemical Society (i) interconnected microfibrous HCs, Reprinted with the permission from [148], Copyright 2011, Royal Society of Chemistry, (j) random sheets, Reprinted with permission from [86], Copyright 2016, Elsevier, (k) macroporous HCs with spherical pores, Reprinted with permission from [92], Copyright 2012, American Chemical Society and (l) macroporous HCs with rectangular pores, Reprinted with permission from [149] Copyright 2019, John Wiley and Sons.

Although HTC is highly employed, the process has some limitations, including the need for heating (temperature) and high pressure, which are aspects that increase the cost for industrial production. Thus, eco-friendlier approaches are of great interest. For example, Beda et al. [98, 115] adopted a low-energy approach and successfully prepared HC spheres at ambient temperature and pressure using a green phenolic resin and a cross-linker. The synthesis was based on a simple sol-gel process and a thermopolymerization step followed by thermal annealing.

Another type of morphology, i.e., hollow spheres, has also been synthesized for hosting Na ions. In 2012, Tang et al. [145] reported for the first time the utilization of such a morphology as an HC anode for SIBs. The authors used hydrothermal carbonization of glucose in latex templates (Figure 7.b). The resulting hollow spheres were interconnected and possessed an internal diameter of ~125 nm and a thickness of ~12 nm. Additionally, the (0D) morphology explored for the HC electrodes also includes carbon quantum dots. Xie et al. [101] reported carbon dots derived from cellulose by directly drying and then carbonizing (1300-1500 °C) the supernatant (i.e., liquid phase) obtained after the HTC process (0.04 $g.mL^{-1}$ cellulose solution at 200 °C for 12 h). The materials exhibited a high specific capacity of 300 mA h g^{-1} and enhanced iCE (91%) at 30 mA g^{-1}; therefore, they had better performance than the HC materials obtained by pyrolysis of the solid phase resulting from HTC.

Depending principally on the synthesis pathway rather than the precursor type, a variety of (1D) morphologies could be obtained, including rods, fibres, nanowires, and tubes. The advantages of these shapes lie in the low volume-to-surface ratio, the short ionic diffusion length, the richness in reactive sites, the reduction of the volume expansion effect, and the improved electrochemical performance for SIB anodes [150, 151]. In this context, various precursors have been used, such as polyaniline [116] polyacrylonitrile [152], pyrrole [146], polyvinyl chloride [74], natural cotton [153], and corn silk [154]. Wang et al. [146] successfully synthesised uniformly shaped cross-linked nanofibers with a diameter of ~ 100 nm. To obtain this (1D) structure, the authors used synthetic polypyrrole nanofibers as precursors, followed by carbonisation at 600 °C for 2 h under N_2 (Figure 7.c). Jiang et al. [86] showed that HC rods retain the silk-like form of carbonised ramie fibres (700 °C for 3 h, under Ar). To ensure that the fibres maintained their dimensions during the carbonisation process, the authors first stabilised them at 200 °C under air for 1 h. Hence, unwoven, long and randomly oriented microfibers were obtained with a similar diameter distribution of approximately 10 µm (Figure 7.d) [86]. In a different study, Wang et al. [147] prepared unwoven N-doped porous carbon nanofibers (N-CNF) *via* an indirect carbonisation process of a nanofibrous polymeric precursor made by electrospinning of polyamic acid (Figure 7.(e-f)). Choi et al. [78] reported the synthesis of woven carbon microfibers (PP-CFs) from natural waste silk fabric *via* a direct pyrolysis process at different temperatures ranging from 800 to 2800 °C (Figure 7.(g-h)). Another strategy to attain the desired morphology (i.e., fibrous) is by using a template. By employing a template of hierarchically porous silica, mesophase pitch was successfully converted into highly linked microfibrous HC [148] *via* carbonisation (Figure 7.i), followed by template removal (i.e., washing).

Hard carbon (2D) structures (e.g., nanosheets, films, nanoflakes, and nanowalls) attract much interest owing to their advantages, e.g., a large surface-to-volume ratio, enhanced electronic transfer, and high ionic diffusion efficiency [155]. Previous research implied a variety of precursors to prepare nanosheet structures. For example, corncobs were used [86] to synthesise (2D) hard carbon nanosheets *via* carbonisation at 700 °C under an argon atmosphere, Figure 7.j. A similar morphology was obtained by Xia et al. [140] by using a synthetic polymer obtained by polymerisation of aniline monomer with resorcinol and a very low amount of graphene oxide as a structuring agent. Hence, an open structure of HC nanosheets was obtained through carbonisation at various temperatures (900 °C to 1100 °C) under an Ar atmosphere.

Concerning the (3D) morphology, usually the particles have a random-like shape and size, which is often reported for hard carbon. In some cases, meso- and macro-pores can be present. In this context, Ding et al. [92] successfully synthesised hard macroporous carbon material with spherical pores using a peat moss pyrolysis process at 1100 °C (Figure 7.k). Furthermore, Li et al. [149] synthesised hard carbon with a (3D) macroporous morphology from cork. The authors demonstrated that the microstructure of the material can be altered simply by adjusting the pyrolysis temperature from 800 °C to 1600 °C: the initial geometry of the hexagonal pores was reshaped into rectangular pores (Figure 7.l).

3.2 Hard Carbon Structure

The hard carbon structure is of prime importance for Na-ion insertion. This can be impacted by several parameters, as will be discussed in this section. X-ray diffraction (XRD), a nondestructive analysis technique, is usually used to obtain structural information about materials on a large scale and thus provide a global overview of the sample's structural features. The diffracted incident X-ray beam provides information on the graphene interlayer distance, crystallinity, impurities, and other valuable structural parameters. The typical hard carbon XRD pattern shows broad diffraction peaks, a sign of a low degree of graphitization, and asymmetric (hk0) crystallographic planes (Figure 8.a) [41]. In addition, there is often a rising background at low two-theta (< 20°) due to the presence of fine structural microporosity [130].

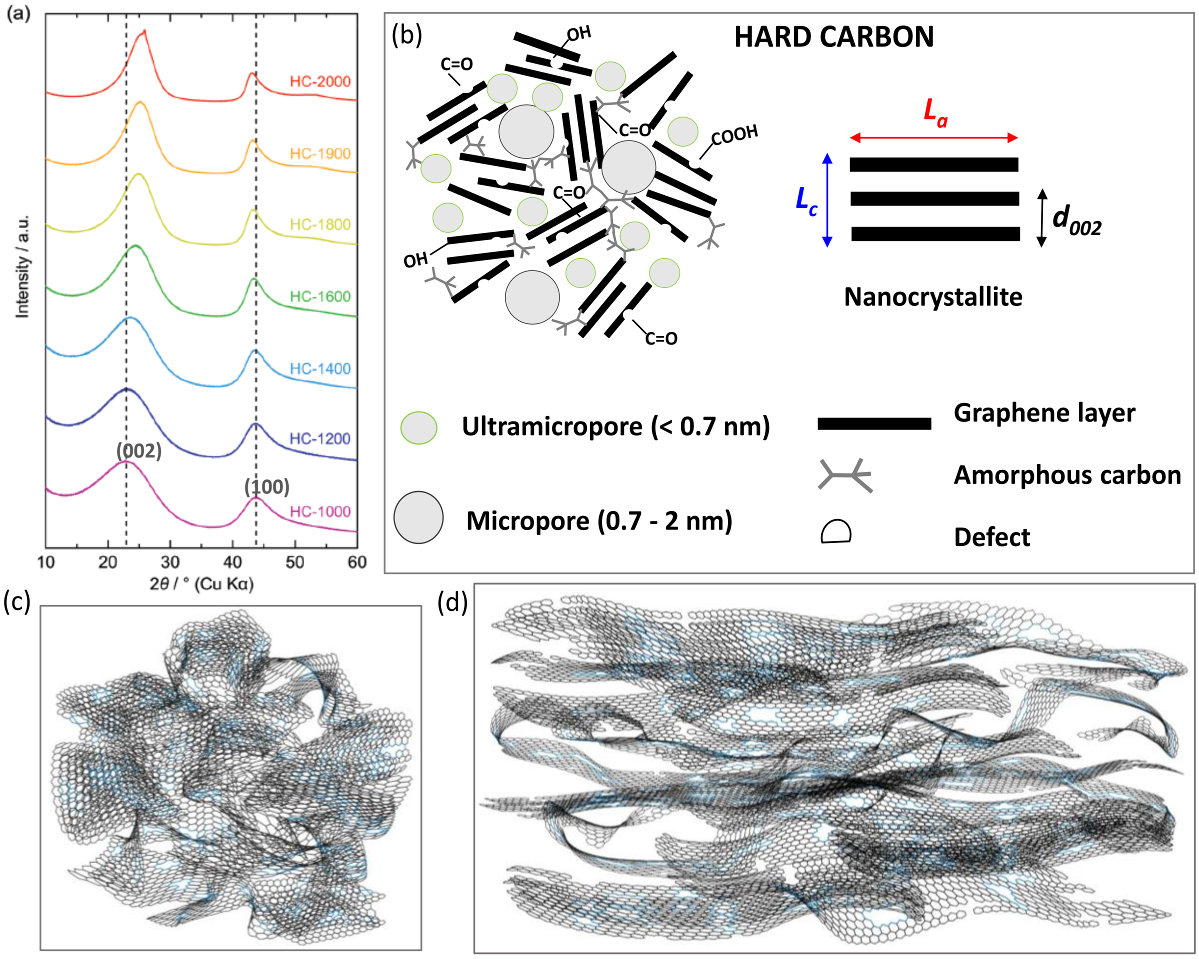

Figure 8 : (a) Wide-angle XRD diffraction patterns of hard carbons derived from sucrose heated at temperatures ranging between 1000 and 2000 °C. Reprinted with the permission from [41], Copyright 2020, John Wiley and Sons. (b) Schematic drawing of the hard carbon structure showing the main specific parameters that can be deduced from the XRD diffractograms (interlayer spacing, d_{002}, crystallite height, L_c and crystallite length, L_a). Adapted with the permission from [40], Copyright (2018), Elsevier. (c) 3D and (d) 2D representation of hard carbon structure as proposed by the authors of this work.

Hard carbon materials have a non-graphitizable and disordered structure, which includes various structural defects, amorphous regions, pseudo-graphitic domains (short turbostratic stacked graphene layers) and nanopores (Figure 8.b). The HC structure is very complex, and several 2D [23, 156] and 3D[157-160] hard carbon models have been reported in the literature to describe it, as nicely detailed in the review of Passerini et al.[130]. Figures 8 c and d show a representation of these structures. Stevens and Dahn[23] model is the most accepted one, although improvements are still required. It consists of a mixture of pseudo-graphitic micro-crystallites (short turbostratic stacked graphene layers; sp^2-hybridized) and amorphous regions (defective graphene layers; sp^3-hybridized). The pseudo-graphitic regions have lateral dimensions (L_a) of ~ 40 Å which are stacked in 2–3 parallel layers, therefore, a crystallite height (L_c) of about 10-12 nm. Further work showed that the L_a and L_c dimensions can be much larger depending on the synthesis conditions (see Figure 10). Despite the local stacking of pseudo-graphitic domains, the orientation of graphene layers is rather disordered at larger scale, resulting in nanovoids and pores[130].

Concerning the structural parameters, the so-called d-spacing (d_{002}) corresponds to the apparent distance between the graphene layers along the perpendicular (002) direction, as calculated by Bragg's law. The thickness (L_c) and width (L_a) of the pseudo-graphitic nanodomains, also known as crystalline height and length, respectively, can be estimated using (002) or (100) diffraction peaks by implying the Debye-Scherer formula: $L_{(a,c)} = k \cdot \lambda / (\mathrm{FWHM} \cdot \cos(\Theta))$, where k = 1.84 for L_a and 0.9 for L_c; FWHM is the full width at half-maximum intensity, corresponding to each particular diffraction peak; λ is the X-ray wavelength [44]. Moreover, the average number of stacked graphene layers can be deduced as follows: $(L_c/d_{002}) + 1$.

In general, as the pyrolysis temperature increases (Figure 8.a), a shift of the peaks towards higher 2θ diffraction angles is observed along with an increase in intensity. This translates into a decrease in the interlayer distance and an improved structural organisation. It is worth mentioning that a larger d_{002} space facilitates sodium ion intercalation and improves capacity, as demonstrated by Gomez-Martin et al. [45]. Figure 9 shows an overview of the literature data on the evolution of the d-spacing for various hard carbon-based resources (i.e., biomass, biopolymers, and synthetic polymers) subject to thermal treatment between 600 °C and 2000 °C. In general, at low pyrolysis temperatures, all precursors lead to HCs with large d_{002}; however, when the temperature increases, the HCs derived from biomass precursors present higher interlayer spaces (i.e., 4.15 Å at 1000 °C (peanut-shell [83]) to 3.55 Å at 1600 °C (spartina alterniflora [161]), Figure 9.a) compared to HC from biopolymers (i.e., 4.13 Å at 1000 °C (microcrystalline cellulose [83]) to 3.46 Å at 1600 °C (sucrose [162]), Figure 9.b) and synthetic polymers (i.e., 4.17 Å at 1000 °C (resorcinol [38]) to 3.43 Å at 1700 °C (PVC [163]), Figure 9.c). Feng et al. [164] attributed this tendency to the natural presence of heteroatoms (oxygen, nitrogen and/or sulphur) in the structure of biomass precursors, which create strong covalent crosslinks with carbon.

Interestingly, Qian et al. [165] synthesized hard carbon materials by pyrolysis of sulphur-doped polyacrylonitrile at various pyrolysis temperatures (800 °C to 1200 °C). The authors reported that the increase in pyrolysis temperature triggers the enlargement of d_{002} from 3.53 Å to 3.66 Å. This outcome was explained by the fact that a higher temperature is able to promote sulphur binding to the carbon backbone, resulting in an increase in d-spacing. The same finding was reported by Kong et al. [166], where fluorine doping could expand the interlayer distance of commercial hard carbon material from 3.86 Å to above 4.00 Å. Moreover, the presence of some inorganic species might also impact the interlayer space [137].

Furthermore, as the temperature increases, the average thickness (L_c) and width (L_a) of the graphitic nanodomains increases. Among the three categories of precursors, biomass persistently showed the highest values (Figure 9). This tendency is related to the improved graphitization with increasing temperature but also due to the local graphitization induced by the presence of inorganic impurities (Fe, Ca, K and Si-based) in such materials [135, 137]. This leads to the formation of larger graphitic zones and a greater number of stacked graphene layers. For example, Si in grape waste-derived HCs led to a greater number of stacked graphene layers (15-24), in contrast to Si-free asparagus- and potato peel-derived HCs, for which a small number of stacked graphene were observed (<5 sheets) [137].

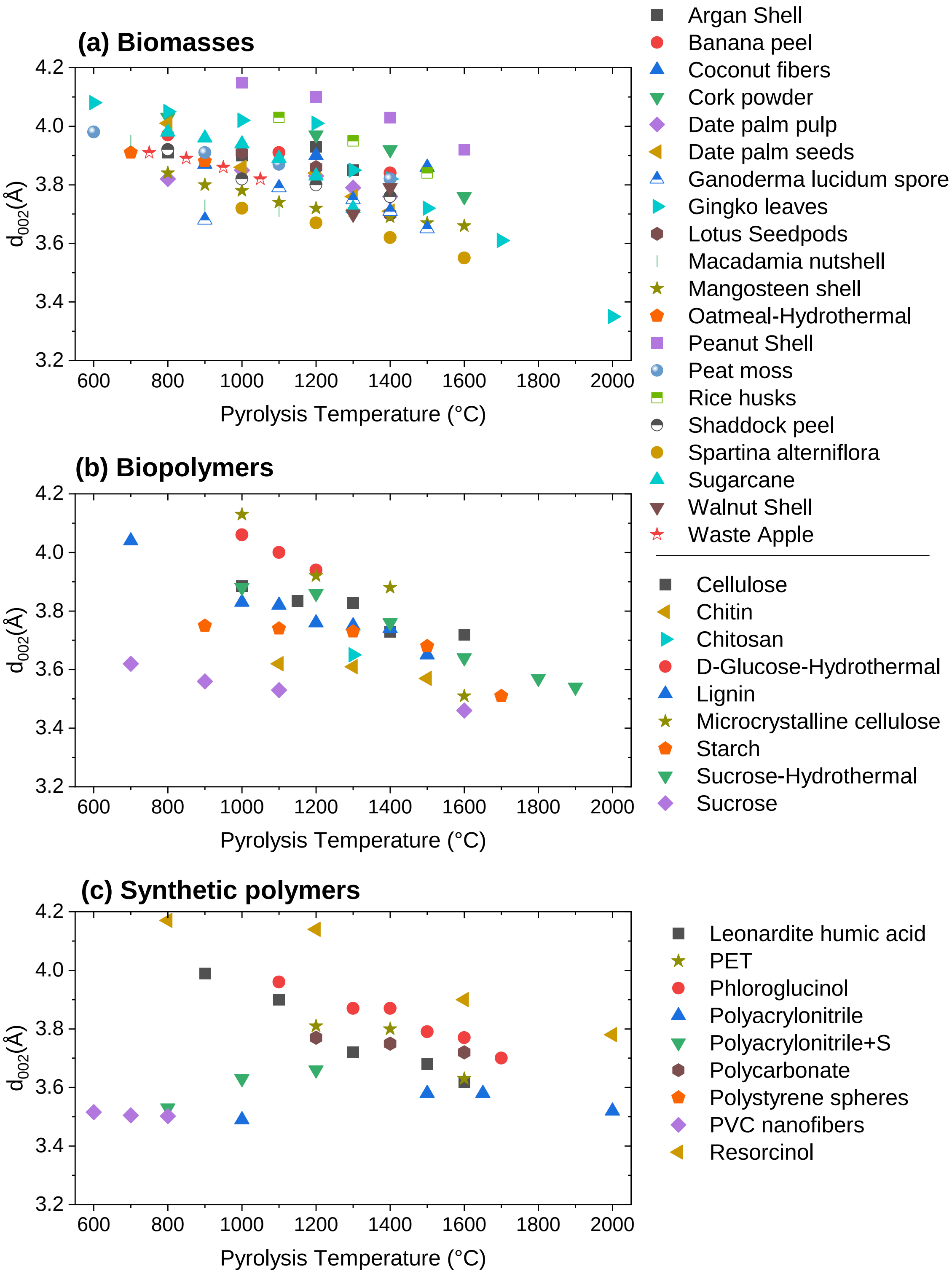

Figure 9: Evolution of the hard carbon interlayer space (d_{002}) with the pyrolysis temperature for the different classes of precursors: (a) biomasses, (b) biopolymers, and (c) synthetic polymers. The graphs were built based on the references presented in Tables 2 to 4.

Additionally, for biomass-derived HC materials, we note the wide dispersion of data; see Figure 10.a. The L_c is between ca. 1 nm (for corn silk at 1300 °C [154]) and ca. 8.1 nm (for ginkgo leaves at 1700 °C [167]). This can be related to the wide variety of chemical and macromolecular compositions of biomass (i.e., cellulose, hemicellulose, lignin, etc.) [168] and the variety of inorganic fractions present (e.g., Na, K, Ca, Mg, Si, etc.)[135]. In the case of biopolymers (Figure 10.b), the L_c and L_a values are much lower (less than ~ 2.5 nm and ~ 6 nm, respectively) and less dispersed compared to those of biomass precursors. Kubota et al. [69] showed that hard carbon synthesised from the sucrose precursor exhibits two crystallite width behaviours: constant L_c values (~ 0.7 nm) when the pyrolysis temperature was varied from 700 °C to 1300 °C and a significant increase between 1300 °C and 2000 °C, reaching a value as high as 1.3 nm. Last, for the synthetic polymer-derived HCs (Figure 10.c), the values fall between those of biomass and biopolymers. In fact, for polymer precursors, the structures are often made of aromatic units (pitch [119], phenolic resin [98], PET [169]) and/or do not contain oxygen in their composition (polyaniline (PANI) [116], polyacrylonitrile (PAN) [170], polyvinyl chloride (PVC) [74]). For these reasons, the L_c and L_a values of polymers are higher than those of biopolymers, which are mainly made up of glucose units rich in oxygen (starch [171], chitosan [29], and cellulose [31]) or aromatic units with rich oxygen groups (lignin [30] and tannin [172]).

Oxygen-based groups are well known to impede graphitization, thus leading to a larger interlayer space and lower L_a and L_c [73, 173].

(a) Biomasses

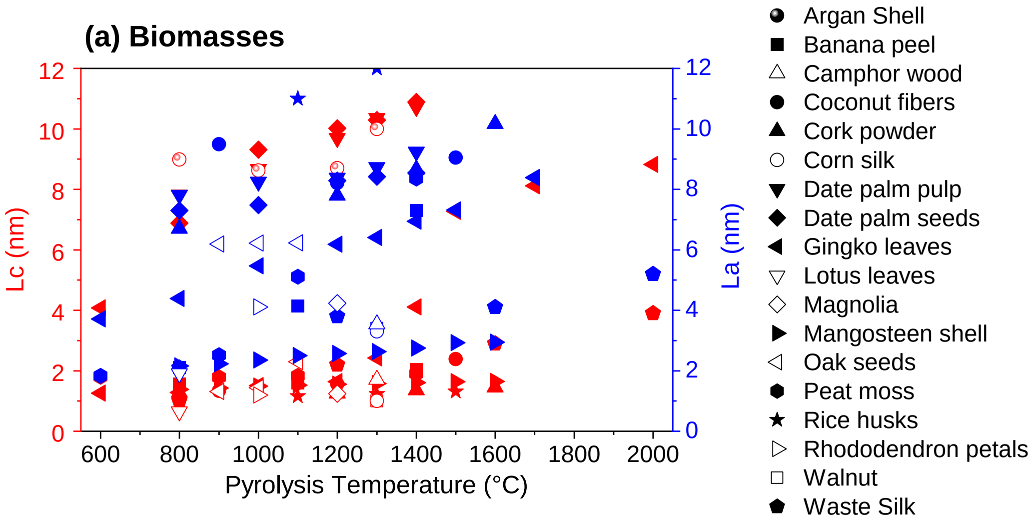

(b) Biopolymers

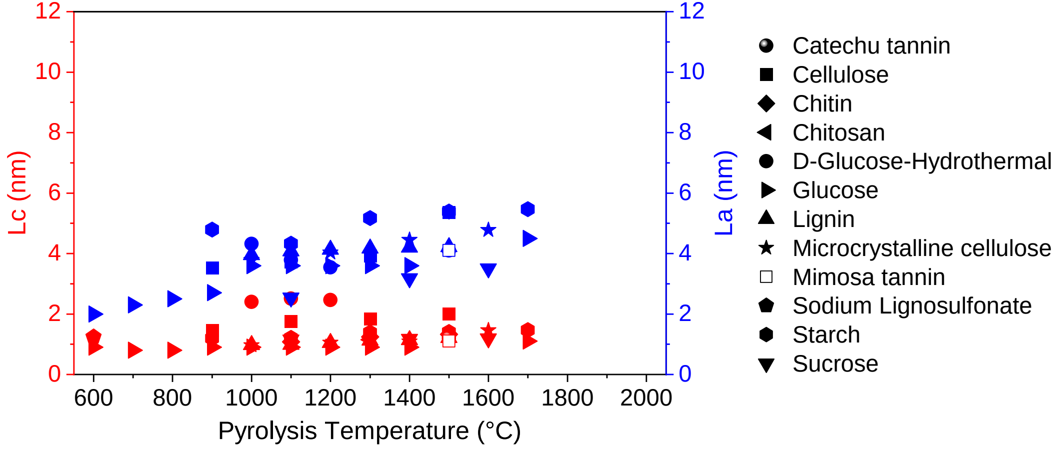

(c) Synthetic polymers

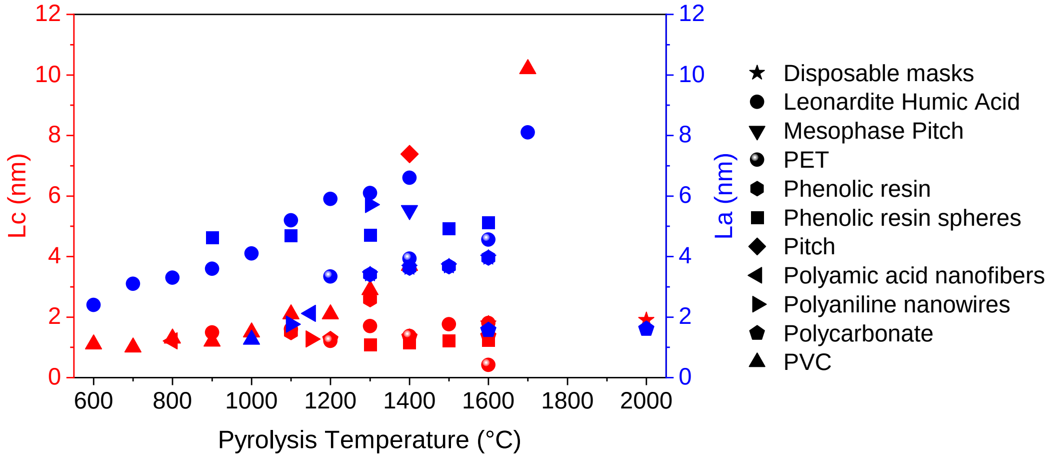

Figure 10: Evolution of hard carbon crystallite size along the c-axis (L_c) and the lateral size of graphene (L_a) with the pyrolysis temperature for the different classes of precursors: (a) biomasses, (b) biopolymers and (c) synthetic polymers. The graphs were built based on the references presented in Tables 2 to 4.

High-resolution transmission electron microscopy (HR-TEM) is another effective technique for exploring nanoscale aspects of hard carbon structures: graphitization and disorder (number, dimensions, arrangement, and d-spacing of graphene layers), porosity (open and closed pores), and the presence of impurities and defects (Figure 11).

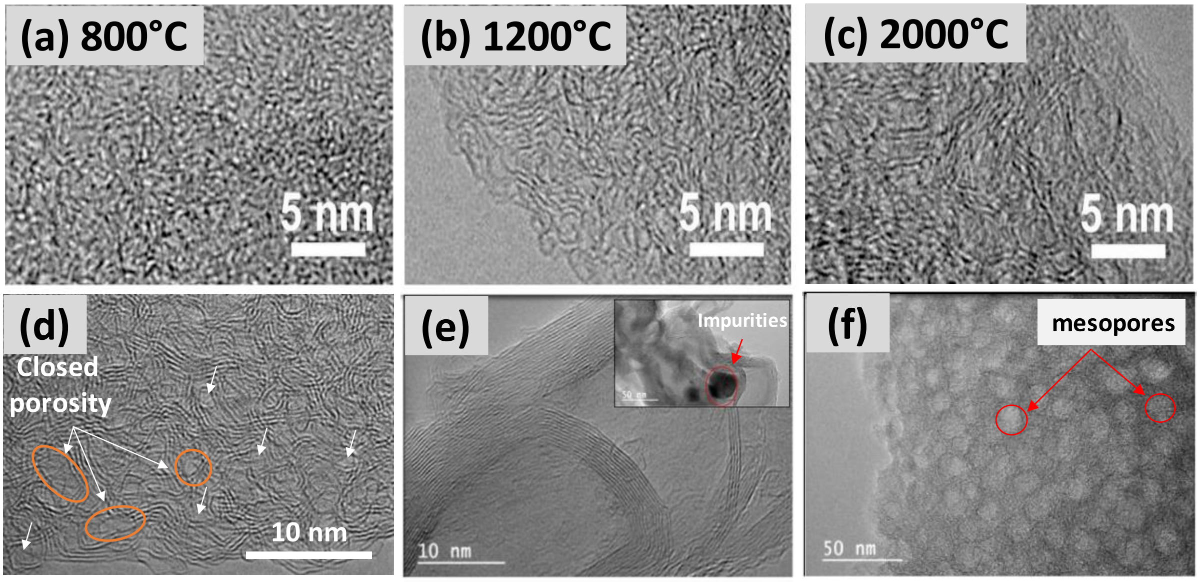

Figure 11: HR-TEM images of hard carbons from (a-c): phenolic resin obtained by pyrolysis at different temperatures from 800 °C to 2000 °C. Reprinted with permission from [79]*, Copyright 2016, Elsevier, (d) biopolymer, reprinted with permission from* [174]*, Copyright 2023, American Chemical Society, (e) grape waste and (f) asparagus peel, reprinted with permission from* [137] *Copyright 2020,, Elsevier.*

The pyrolysis temperature has an important influence on the microstructural properties of hard carbon materials. Figure 11.(a-c) clearly show that by increasing the carbonisation temperature, the disordered aspect of the HC structure decreases. This disordered appearance is caused by the random packing of curved and disoriented layers of graphene. Hasegawa et al. [79] identified graphene fragments of less than 1–2 nm at 800 °C (Figure 11.a). Upon increasing the temperature from 1200 °C to 2000 °C, the layered structure becomes more developed (> 2 nm), resulting in approximately 5 graphene sheets that are encrusted and stacked; see Figure 11.(b-c). The same behaviour was reported by Zhen et al. [175] by increasing the pyrolysis temperature from 900 °C to 1300 °C using a sucrose precursor. The authors observed a transition from a disordered to a localized ordered structure of HC due to the rearrangement of carbon atoms. Most hard carbons reveal a similar tendency of structure modification with pyrolysis temperature.

Another interesting structural feature highlighted by HR-TEM is the formation of closed porosity, as presented in Figure 11.d. The appearance of closed pores is generated by the local voids created between graphitic and disordered zones. This type of porosity is prevalent when the precursor is pyrolyzed at temperatures greater than 1300 °C [23]. Stevens and Dahn [23] first proposed the model of micropore closure in HC as a function of annealing temperature. According to the authors, an increase in the pyrolysis temperature led to open porosity closure, reorganization of the graphene sheets, and the formation of slightly larger pores between the graphene sheets, known as closed pores. More details about this type of porosity will be given in the next section.

As mentioned above, inorganic impurities have an impact on the HC structure, mainly reducing the d-spacing due to catalytic-induced graphitization (Figure 11.e). HR-TEM better highlights these modifications. Ghimbeu's group studied the impact of these impurities on the HC structure by using different biomass precursors (i.e., asparagus peel, potato peel, and grape waste) and a pre- or post-annealing washing step [137]. Notably, grape waste displayed increased graphitization and graphene stacking (Figure 11.e). One can note many graphitic zones composed of several stacked graphene layers (15-20) around the impurity particles (black zone, *inset* Figure 11.e). This phenomenon was explained by the high and persistent Si concentration (Si = 1.9 wt.% even after washing), which acts as a catalyst and induces graphitization at high pyrolysis temperatures. The same behaviour was observed by Nita et al. [154] when using coconut shells, walnut shells, and corn silk precursors. In particular, the HC obtained from corn silk was more graphitized and had a pronounced stacking aspect (10-20 graphene layers). This feature is due to the higher wt.% of Si impurities in corn silk, which is three times greater than that in walnut shells and coconut shells (0.85 at.% in corn silk *vs*. 0.3 at.% in coconut shells *vs.* 0 at.% in walnut shells). Moreover, Rios et al. [135] observed the growth of SiC wires due to the presence of large amounts of Si in grass biomass. Last, Figure 11.f shows numerous spherical white areas related to mesopores in the HC structure, as revealed by HR-TEM. This feature was reported to arise from the elimination of inorganic impurities *via* washing post-pyrolysis [137], which leads to porous free spaces.

3.3 Hard Carbon Porosity

The textural properties of hard carbon materials, including the pore volume, pore size distribution and architecture, and specific surface area (SSA), are of high importance for improving the performance of electrochemical storage systems. As has been well documented, by reducing the specific surface area, a lower electrode-electrolyte contact surface is achieved, thus improving the initial Coulombic efficiency (iCE) [27, 61] and the cycling life in SIBs [29, 89]. Furthermore, porosity has a direct influence on the ionic diffusion pathways and thus the reversible capacity [28]. Consequently, optimization of this parameter is always needed.

The porosity of a given solid material, particularly a hard carbon, can be divided into open porosity (also known as accessible porosity) and confined pores, which are referred to as closed porosity (inaccessible pores to probe gases) (Figure 12.a).

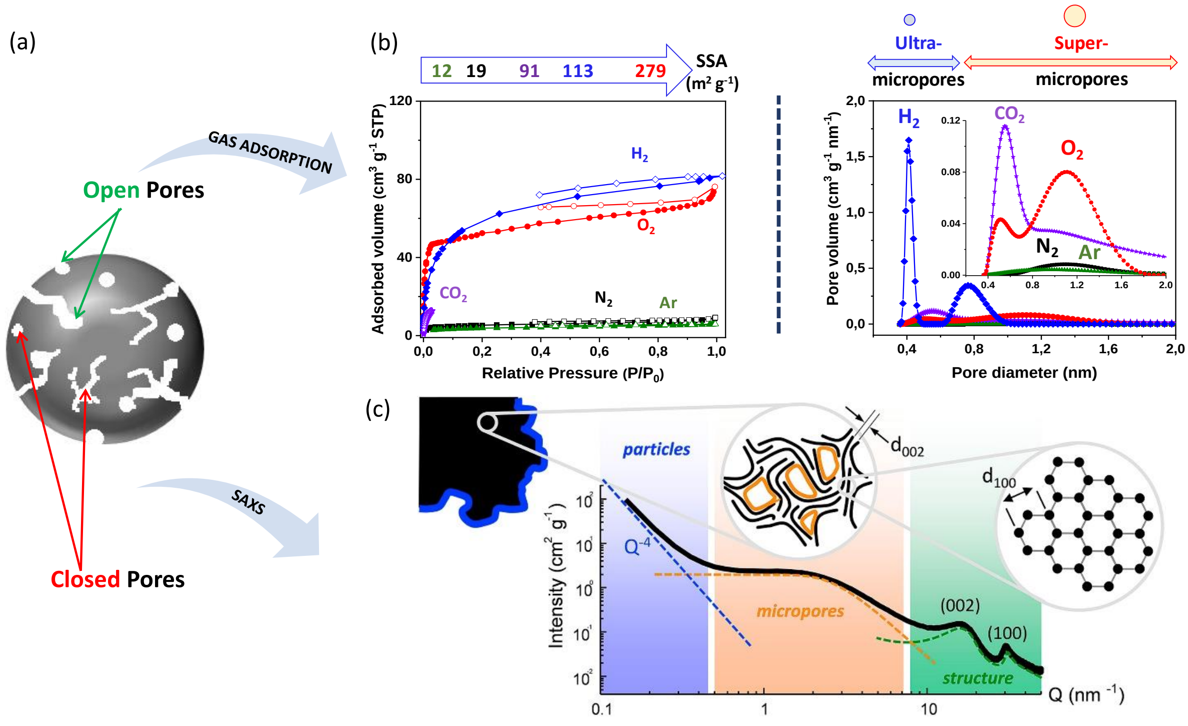

Figure 12: (a) Schematic representation of a hard carbon particle illustrating open and closed porosity. Reprinted with permission from [98], Copyright 2021, Royal Society of Chemistry. (b) Gas adsorption isotherms measured at 77K for all gases except CO_2 (273K) and pore size distribution used to evaluate the open porosity of hard carbon. Reprinted with permission from [176]. Copyright 2021, Royal Society of Chemistry. (c) SAXS patterns show the approach used to determine the hard carbon porosity (open and closed). Reprinted under the terms of CC BY-NC-ND 4.0 DEED licence [177]. Copyright 2019. The authors. Published by Elsevier B.V.

Adsorption/desorption of a probe gas molecule is the traditional method for investigating open pore structures and for determining the SSA of solid materials (see Figure 12.a). In this context, N_2 adsorptive molecules at 77 K are widely used to evaluate the open porosity, namely, the micropores (< 2 nm) and the mesopores (2-50 nm), and to determine the Brunauer–Emmett–Teller (BET) SSA of hard carbon materials. However, precise characterization of the narrow micropores present in the HC structure (< 0.7 nm) is not possible by N_2 due to its large size (inaccessible into tiny pores) and slow diffusion kinetics in the complex structure of hard carbon [176]. IUPAC recommends Ar as a better alternative to N_2 due to its null quadrupole momentum [178], which prevents any interactions between carbon and gas molecules. However, in regards to HCs, Ar is not more effective than N_2 on such complex structures (Figure 12.b) [176].

Instead, CO_2 at 273 K has been revealed to be more suitable for accessing the tiny pores of HC and to determine the so-called ultramicroporosity of <0.7 nm (Figure 12.b) [40, 176]. This is related to the fast diffusion kinetics of the CO_2 molecule induced by the high adsorption temperature compared to N_2. Additionally, the SSA found is significantly higher in most cases, meaning that the probed surface area is gas dependent and misleading information can be revealed by using N_2 gas only. CO_2 gas at 273 K cannot be used to characterize pores larger than 2 nm, and therefore, it must be used in complement with another probe molecule. Another drawback of CO_2 is its high quadrupole moment (higher than that of N_2), making it unsuitable for determining the porosity of materials containing polar sites, due to the possible interactions with CO_2 that improve its adsorption and thus leads to the difficulty of discriminating between the contribution of effective porosity and that of surface chemistry [179].

Recently, other particular probe molecules, such as O_2 and H_2 at 77K, have been reported to be efficiently approached for the evaluation of hard carbon porosity [176]. The authors revealed that such gases allow one to gain in-depth insight into the existence of pores (Figure 12.b) otherwise undetected by the previously mentioned gases (i.e., N_2, Ar, CO_2). More precisely, the obtained isotherms show significantly higher adsorbed volumes for both H_2 and O_2 compared to conventional gases. The same was observed when the SSAs were determined, e.g., 279 m^2 g^{-1} by O_2 *vs.* 19 m^2 g^{-1} by N_2 (*vs.* 113 m^2 g^{-1} by H_2) [176]. Ghimbeu and her team concluded that H_2 represents a better alternative to CO_2 to evaluate the narrow ultramicroporosity of hard carbon materials due to both its smaller size and its low quadruple momentum (Figure 12.b). On the other hand, the O_2 molecule, which has a larger size but a smaller quadrupole momentum, is the only gas capable of accessing the entire range of pores, that is, ultramicropores (<0.7 nm) and supermicropores (0.7 nm < dp < 2.0 nm); thus, it is a suitable candidate for the precise characterization of HC porosity. However, the analysis time is very long (~ 5 days) due to the slow diffusion of gas through very narrow pores. Such pores can trap gas molecules that are difficult to desorb, leading to the observed isotherm hysteresis. Furthermore, the specific surface area determined with O_2 is strongly correlated with the irreversible capacity of hard carbon in SIBs, i.e., a higher specific surface area leads to a higher irreversible capacity [176, 180]. Despite these arguments, there is a scarcity of data on the use of O_2 and H_2 gases on hard carbon materials.

As mentioned above, HC porosity is characterized mainly in the literature by the probe molecule N_2 and, second, by CO_2. Figure 13 and 14 present a general view of the evolution of specific surface areas of various hard carbons assessed by the gases mentioned above. The materials are derived from different resources (i.e., biomass, biopolymers or synthetic polymers) and pyrolyzed at a wide range of temperatures, i.e., 600 to 2000 °C. In general, the specific surface area decreases with increasing pyrolysis temperature, regardless of the precursor origin. This trend is well known to be related to the reduction in microporosity caused by the reorganization of the hard carbon microstructure, resulting in the closure of the porosity, particularly above 1000 °C [44]. On the other hand, for the same pyrolysis temperature, the SSA values depend on the precursor type, especially at low temperatures (< 1200 °C, see Figure 13).

If we consider the N_2 data reported in the literature shown in Figure 13, a wide range of SSA values has been reported, for example, 550 $m^2\,g^{-1}$ for glucose HC obtained at 600 °C [163] to 0.4 $m^2\,g^{-1}$ for an HC derived from silk waste at 2000 °C [78]. In addition, one can clearly see the above-mentioned trends: decreased areas with an increase in the temperature and the importance of the precursor origin for the same annealing temperature. For example, when increasing the carbonization temperature from 800 °C to 1500 °C, the SSA of mangosteen shell-derived HC decreased from 539 $m^2\,g^{-1}$ to 9 $m^2\,g^{-1}$ [25], while that of lignin-derived HC decreased from 125 $m^2\,g^{-1}$ to 15 $m^2\,g^{-1}$ when the temperature increased from 1000 °C to 1500 °C [181].

Moreover, the structure and chemical composition of the precursors have an important influence on the porosity of the obtained HC. Among the three categories of precursors presented in Figure 13, biomass precursors lead to materials with higher surface areas, followed by biopolymers and synthetic polymers, with the lowest SSA observed for the derived HCs. For example, at 1200 °C, different SSA values were reported for the different groups of precursors: 359 $m^2\,g^{-1}$ for coconut fibre HC [42], ~55 $m^2\,g^{-1}$ for a lignin HC [85] and ~25 $m^2\,g^{-1}$ for a phenolic resin-derived HC [113].

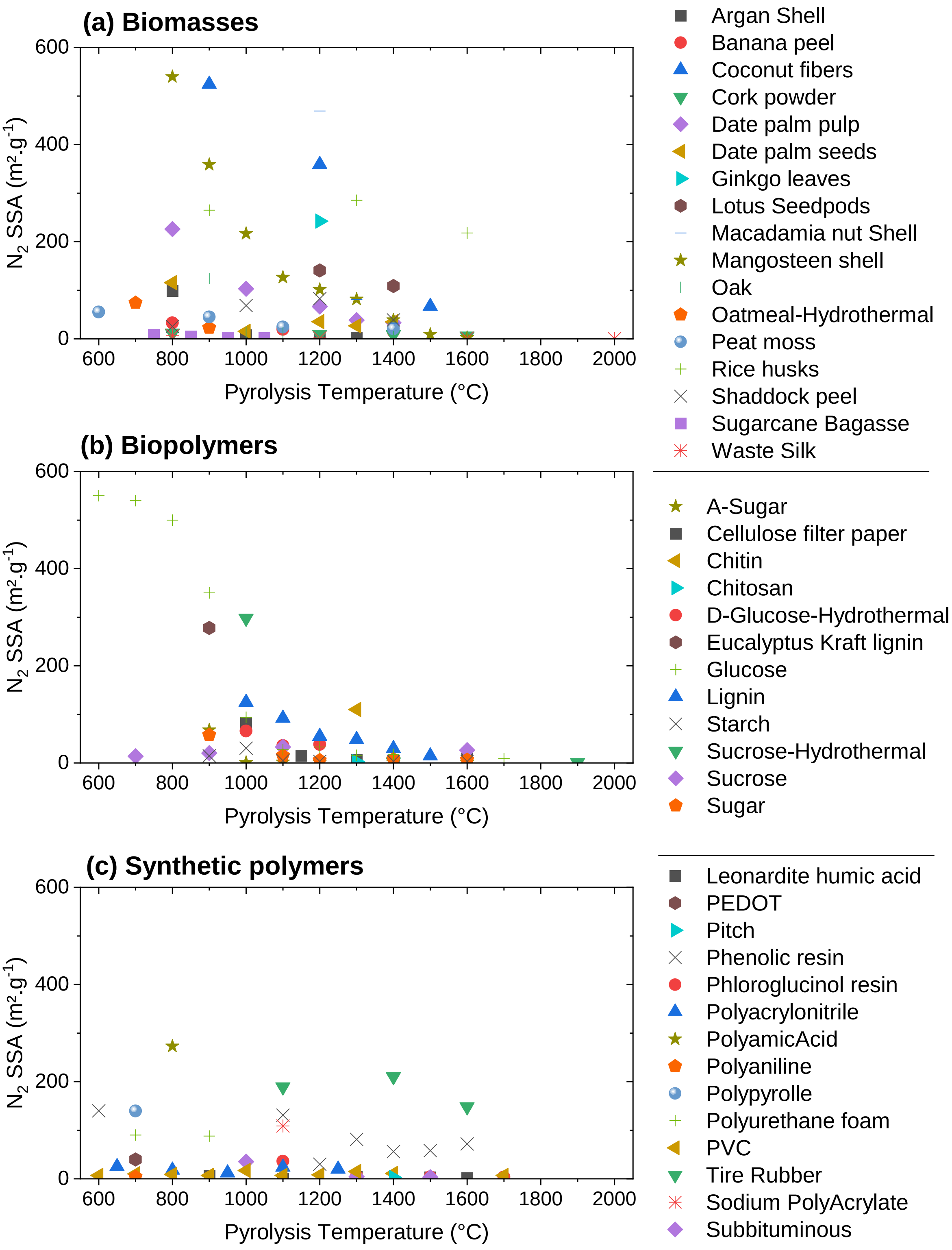

Figure 13: Evolution of the BET specific surface area determined by N_2 adsorption at 77 K, with the pyrolysis temperature for the different classes of precursors: (a) biomasses, (b) biopolymers, and (c) synthetic polymers. The graphs were built based on the references presented in Tables 2 to 4.

In addition, for the same category of precursors and the same pyrolysis temperature, the source of the precursor leads to hard carbon materials with very different N_2 SSA values, e.g., biomass category at 1400 °C, lotus seedpod HC has ~109 $m^2\ g^{-1}$ [182] *vs.* ~21 $m^2\ g^{-1}$ for a peat moss HC [92], biopolymer category at 1000 °C, cellulose HC has 539 $m^2\ g^{-1}$ [183] *vs.* 83 $m^2\ g^{-1}$ for a microcrystalline cellulose HC [40], synthetic polymers at 1400 °C, and tire rubber-derived HC has 210 $m^2\ g^{-1}$ [184] *vs.* ~ 3 $m^2\ g^{-1}$ for a pitch HC [119].

Wu et al. studied in detail the effect of the chemical composition of hard carbon precursors [83]. The authors showed that at 1200 °C, the hard carbon produced from lignin has a much lower N_2 SSA (19.7 $m^2\ g^{-1}$) compared to that of HC derived from cellulose (103.1 $m^2\ g^{-1}$). The difference was related to the structural features of lignin and cellulose precursors, which are composed of aromatic and nonaromatic rings, respectively. It was concluded that the highly condensed aromatic rings of lignin lead to denser HC structures and thus a lower SSA. The structure of the precursor may also play an important role in the final surface area of the materials. It was shown by Irisarri et al. [185] that the pyrolysis of pulp cellulose has a higher N_2 SSA than that of microcrystalline cellulose (87 $m^2\ g^{-1}$ *vs.* 7 $m^2\ g^{-1}$) and can further increase it to 115 $m^2\ g^{-1}$ if pulp cellulose is pelletized. The authors attributed the increase in SSA to the gas evacuation which was low during heat treatment trough the compact samples.

Furthermore, the presence of impurities in the precursor composition plays an important role in dictating the porosity. Beda et al. [137] studied the impact of biomass impurities on hard carbon properties by approaching precursors containing elements, such as Ca, Mg, K, Si, P, and Cl. By performing a post-synthesis washing step, the authors observed that as impurities were removed, the N_2 SSA of HC derived from asparagus peel increased from 7 $m^2\ g^{-1}$ (before washing) to 40 $m^2\ g^{-1}$ (after washing). However, if washing is performed before synthesis, it has been shown that the SSA can be significantly reduced due to the removal of inorganics that impede the activation of carbon during pyrolysis [30].

Additionally, the synthesis process (i.e., pretreatment conditions) is an important parameter that must be taken into account to control the texture of hard carbons. Daher et al. [73] demonstrated that a preoxidation treatment at 300 °C carried out before the pyrolysis of a pitch precursor leads to different N_2 SSAs compared to direct pyrolysis of the same material. Moreover, when oxidation is performed under different atmospheres (i.e., ambient air, oxygen flow, air flow) and durations (i.e., 3, 12, 48, 72 and 200 h), the porosity of the obtained hard carbon changes as well. In particular, the authors observed that preoxidation under air and varying durations (i.e., 3 h to 200 h) increases the N_2 SSA from 1.5 to 49.7 $m^2\ g^{-1}$. The pyrolysis conditions may also affect the porosity of the obtained carbon. Irisarri et al. [186] showed that Ar flow plays a role when sugar is heated at 1100 °C. A low Ar flow rate of 200 $mL\ min^{-1}$ led to a high surface area of 670 $m^2\ g^{-1}$, while by increasing the flow rate to 1000 $mL\ min^{-1}$, the surface area could be significantly decreased to 11 $m^2\ g^{-1}$. Guo et al.[187] showed that the slow heating rate applied to camphor wood residues has a positive effect to decrease the specific surface area from 111.40 to 3.7 $m^2\ g^{-1}$ (for a heating rate of 5 and 0.25 ° C min^{-1}, respectively) and to expand the interlayer space. The same observations regarding the SSA were found elsewhere using sucrose, however, the interlayer space was decreasing with the heating rate [95]. Ultrafast heating rate (300 to 500 °C min^{-1}) in a short time (one minute) by spark plasma sintering (SPS) proved to be an interesting approach to reduce not only the porosity, but also the defects and O-functionalities [188]. In which concern the commercial hard carbons, the specific surface area assessed by N_2 is often available as well. It can be seen in Table 4 that commercially available HC possess a low N_2 SSA, below 10 $m^2\ g^{-1}$.

However, as mentioned before, the porosity of hard carbon is very complex and particular, and the N_2 gas is insufficient to characterize it. Therefore, when CO_2 is approached, as shown in Figure 14, in most cases, the obtained SSAs are higher compared to those obtained by N_2. This is related to the presence of very narrow pores, called ultramicropores (< 0.7 nm), in the hard carbon structure, which is undetectable by N_2. For example, for an HC prepared from bagasse biomass, an SSA of 337 $m^2\ g^{-1}$ was found by CO_2, and only 19 $m^2\ g^{-1}$ was found by N_2 [135]. Similar trends were observed among the biopolymers (i.e., 16.2 $m^2\ g^{-1}$ by CO_2 *vs.* 6.9 $m^2\ g^{-1}$ by N_2 for a catechu extract-derived HC [189]) and the synthetic polymers (i.e., 394 $m^2\ g^{-1}$ SSA by CO_2 *vs.* 131 $m^2\ g^{-1}$ by N_2 for a phenolic resin-derived HC [185]).

As in the previous case (i.e., N_2 gas), CO_2 SSA is influenced by both the source of the precursor and the pyrolysis temperature. In general, regardless of the precursor origin, the CO_2 SSA decreases with increasing temperature, as illustrated in Figure 14. Several reports in the literature are highlighting this trend. For a carbonized cellulose-derived HC between 1000 and 1600 °C, the CO_2 SSA decreases as follows: 406 $m^2\ g^{-1}$ to 380 $m^2\ g^{-1}$ to 255 $m^2\ g^{-1}$ to 40 $m^2\ g^{-1}$ and 3 $m^2\ g^{-1}$ at 1600 °C [40]. The same trend was reported when using an eco-friendly phenolic resin heated between 1100 and 1700 °C to obtain the HC, where the CO_2 SSA decreased from 273 $m^2\ g^{-1}$ to ~21 $m^2\ g^{-1}$ [32].

In addition to the pyrolysis temperature, the precursor source used to prepare the HC material can be detrimental to the CO_2 SSA of the materials. This is very well illustrated in Figure 14 among all three categories of precursors when the pyrolysis temperature is constant.

For example, for biomass precursors at 1000 °C, sugarcane leads to an HC with 525 m^2 g^{-1} CO_2 SSA [124], miscanthus HC to 438 m^2 g^{-1} [190], and wheat straw HC to 257 m^2 g^{-1} [190], while an argan-derived HC leads to a low CO_2 SSA of only 7.7 m^2 g^{-1} [24]. Similar trends can be observed between biopolymers HCs (Figure 14.b) and synthetic polymer-derived HCs (Figure 14.c). Especially for the latter category at low pyrolysis temperatures (e.g., 700 °C), the CO_2 SSAs are quite dispersed and strongly dependent on the precursor type.

Despite the fact that CO_2 gas allows a more detailed characterization of the porosity of hard carbons, the use of this gas is rather limited, as shown from the data in Figure 14 compared to the N_2 data in Figure 13.

(a) Biomasses

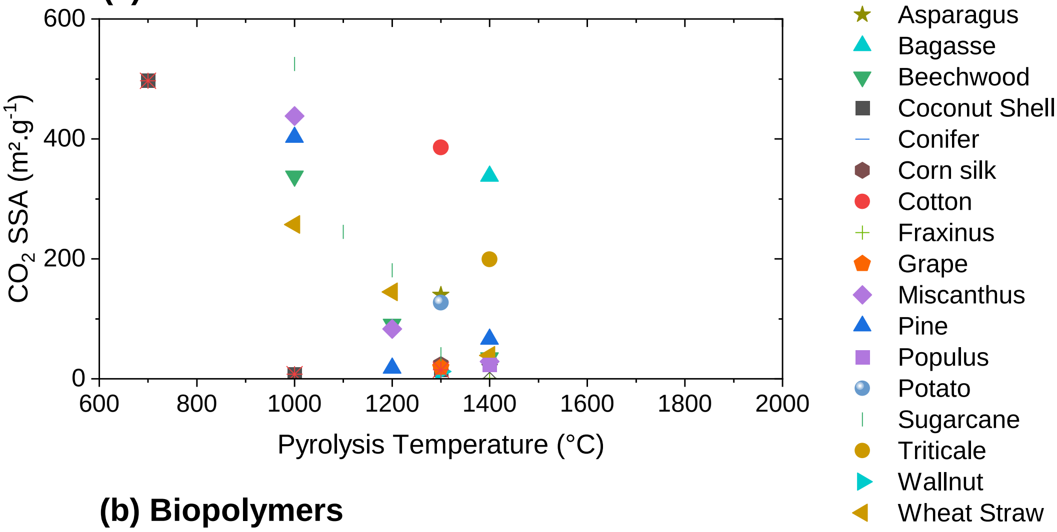

(b) Biopolymers

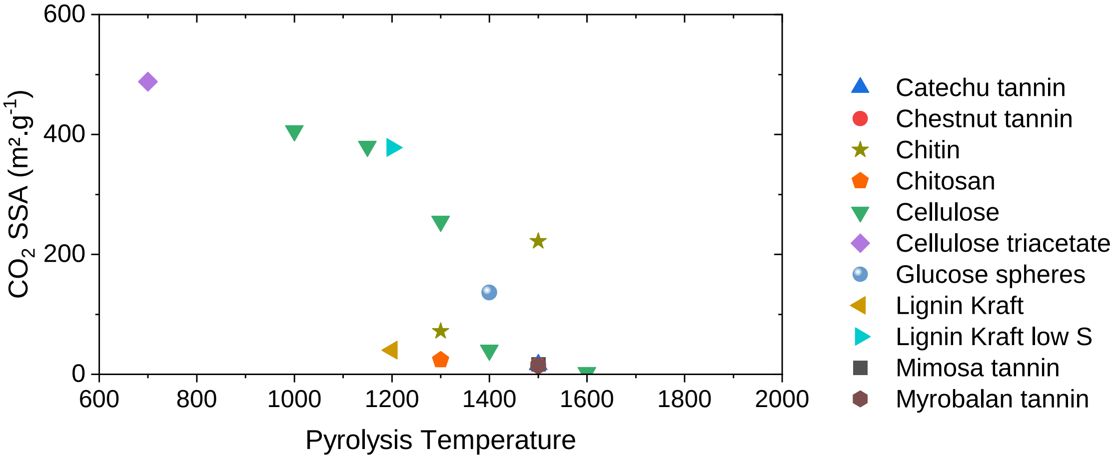

(c) Synthetic polymers

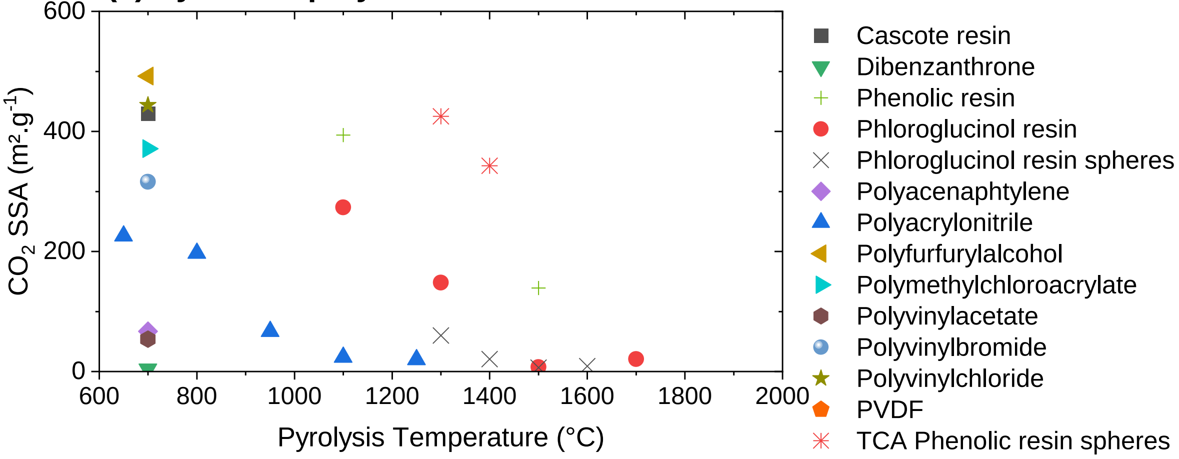

Figure 14: Evolution of the BET specific surface area, determined by CO$_2$ adsorption at 273 K, with the pyrolysis temperature for the different classes of precursors: (a) biomasses, (b) biopolymers, and (c) synthetic polymers. The graphs were built based on the references presented in Tables 2 to 4.

As mentioned above, along with the open porosity, closed porosity is present as well. At high temperatures, the HC framework reorganises and favours the growth of microcrystalline structures. The pseudo-graphitic planes become mobile and align with neighbouring layers, leading to the formation of more stacked layers and micropore coalescence. This induces the closing of certain open pores, thus forming the so-called closed pores [23]. This model explaining the formation of closed hard carbon porosity is known as the 'falling cards' model, as proposed by Stevens and Dahn [23]. The same model first explained the decrease in porosity based on CO_2 adsorption isotherms, as illustrated in Figure 15.a. At low temperature (~900 °C), the micropores are considered type 1, which means that they are fully accessible by CO_2. For temperatures higher than 900 °C, several types of micropores coexist in hard carbon depending on the pyrolysis temperature. For intermediate temperatures (<1400 °C), the pores partially close, leading to micropores with an 'ink bottle' shape (called type 2). Due to narrow pore openings, CO_2 diffusion is more difficult. Finally, at higher temperatures (>1400 °C), the pore openings become narrower and close off (type 3), impeding gas molecules from diffusing inside these restricted closed pores.

As such closed porosity cannot be assessed by gas adsorption, other techniques have been employed in the literature. SAXS (small-angle X-ray scattering) is an interesting tool for investigating the HC texture [63, 177]. In particular, it provides valuable information on the closed porosity, as well as other information. Figure 12.c presents a typical SAXS profile of hard carbon, where the intensity is a function of a scattering vector (q). Such a profile exhibits two major characteristics: a shoulder shape and a continuous increase in intensity by decreasing q. From low- to mid-ranges and then to high q ranges, the morphological (i.e., shape), microstructural (microporosity) and structural characteristics of hard carbon materials can be explored [177]. However, SAXS is restricted only to determining the average pore size, and highly customized equipment is required to establish the distribution of closed porosity in terms of size, volume and/or surface area [191].

With the help of SAXS, Wang et al. [192] revealed the influence of carbonization temperature on closed porosity in anthracite-prepared hard carbons. When increasing the temperature from 700 °C to 1500 °C, an increase in the closed pore volume from $0.05\ cm^3\ g^{-1}$ to $0.12\ cm^3\ g^{-1}$ and a pore size from 1.74 nm to 2.37 nm was observed by SAXS (Figure 15.b). These schematically represent the evolution of porosity with pyrolysis temperature, as illustrated in Figure 15.c. Furthermore, the appearance of closed porosity was accompanied by a decrease in He density from $2.05\ g\ cm^{-3}$ (700 °C) to $1.77\ g\ cm^{-3}$ (1500 °C), as reported by the same authors.

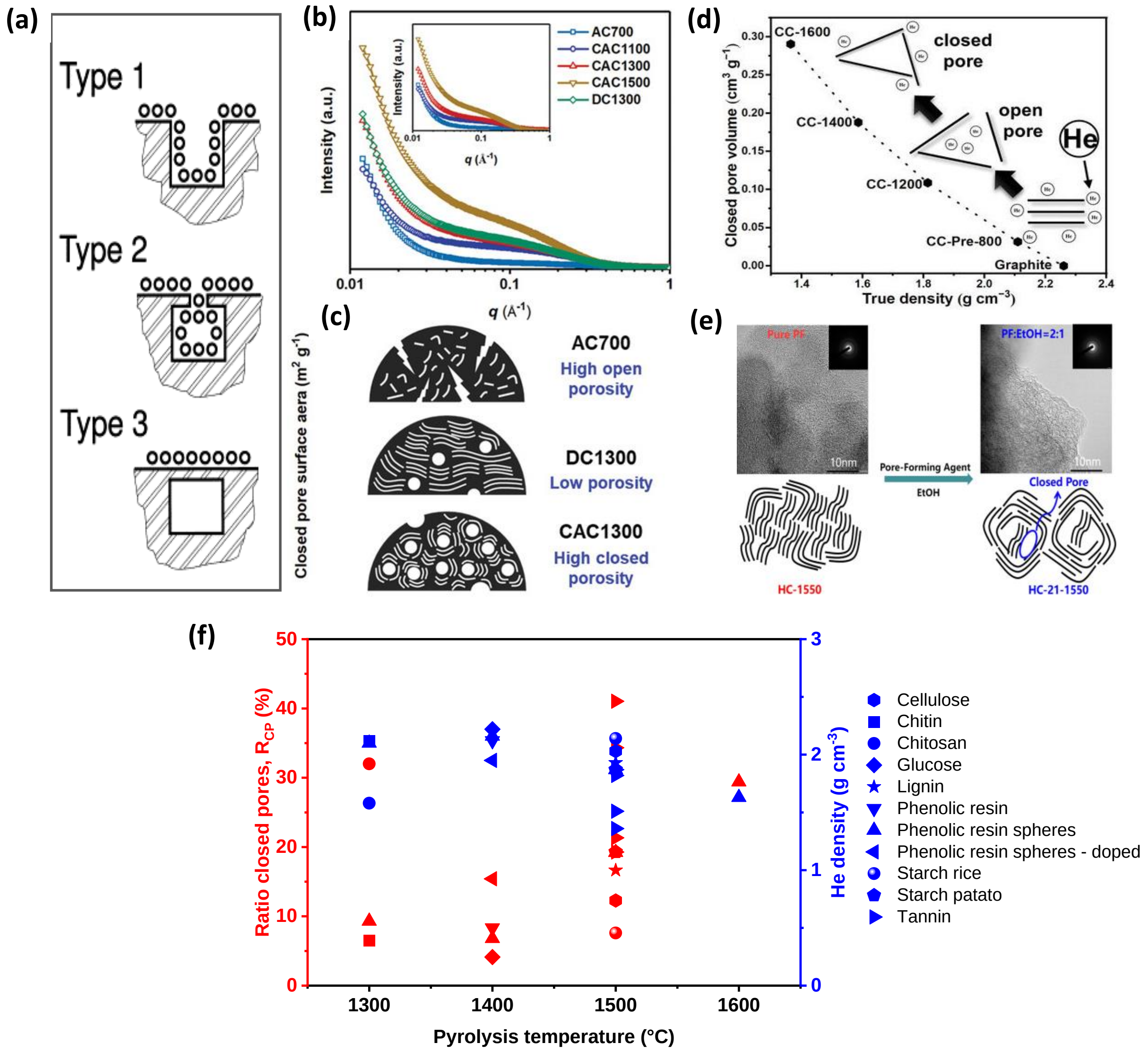

Figure 15: (a) Model of micropore closure in sucrose-derived hard carbon showing open micropores (Type 1), partially closed micropores (Type 2) and fully closed micropores (Type 3) proposed by Buiel et al., Reprinted with the permission from [23], Copyright 1999, , Elsevier. b) SAXS patterns and c) schematic representation of the pore structure evolution during thermal pyrolysis of activated anthracite at different temperatures. Reprinted with permission from [192], Copyright 2022, John Wiley and Sons. (d) Evolution of closed pore volume with the true density of HC derived from cork. Reprinted with permission from [149], Copyright 2019, John Wiley and Sons. (e) Closed pores generated by varying the amount of ethanol in the synthesis. Reprinted with permission from [193], Copyright 2019, American Chemical Society. (f) Evolution of the closed porosity and He density vs. pyrolysis temperature of different precursors [29, 98, 174, 189].

Li et al. [149] observed the same tendency in a cork biomass HC produced at different pyrolysis temperatures. Based on SAXS, TEM and pycnometry analyses, increasing the carbonization temperature from 800 °C to 1600 °C results in i) larger closed pores (from 3.47 to 4.50 nm), ii) a higher volume of closed pores (from 0.03 to 0.29 $cm^3 g^{-1}$) and iii) a lower He density (from 2.11 to 1.36 $g cm^{-3}$). The authors also observed that an increase in the volume of closed pores leads to a decrease in the true density of hard carbon, as shown in Figure 15.d.

Nevertheless, other strategies can be used to tune the closed pores. For example, Zhou et al. [194] prepared HC from rosewood (pre-chemically treated or not) at 1100 °C and found that the chemical treatment led to a larger volume of closed pores compared to the untreated HC (i.e., 0.055 $cm^3 g^{-1}$ *vs.* 0.039 $cm^3 g^{-1}$). The higher volume of closed pores was related to the breakdown of the fibrous structure of the precursor (i.e., the elimination of hemicellulose/lignin and the partial hydrolysis of cellulose in an alkaline medium), which resulted in the development of closed pores with thinner walls. For the same purpose, Meng et al. [193] used phenol-formaldehyde resin and ethanol to generate closed pores in hard carbon and found the optimal ethanol fraction of 33% to obtain the highest number of closed pores (Figure 15.e).

Complementary to SAXS, the closed porosity ratio (R_{CP}) can be estimated considering the HC He density (d_{He}) and the total open pore volume (V_{OP}) determined by nitrogen adsorption, via the following equation: R_{CP} (%) = $(1/d_{He} - 1/2.26) / (V_{OP} + 1/d_{He}) \times 100$ [195].

Figure 15.f shows the evolution of the closed porosity and He density with the pyrolysis temperature for several precursors as studied by Ghimbeu et al. [29, 98, 174, 189]. Indeed, the general tendency of the closed porosity is to increase with the pyrolysis temperature, while the He density shows the opposite behaviour. However, the precursor itself is as important as the temperature. If 1500 °C is taken as an example, the closed porosity varies from 7.6% for starch rice [174] to 19.23% for phenolic resin spheres [98] and to 41.04% for chestnut polyphenol [189]. These differences might be explained by the different chemical compositions, structures, and porosities of these materials.

3.4 Hard carbon chemical composition/surface chemistry

In addition to structural and textural features, a comprehensive understanding of the surface chemistry of hard carbon materials is crucial, given that electrolyte-HC electrode interactions determine the electrochemical performance. In particular, hard carbon materials have several surface functional groups. They are mainly composed of oxygen-based functional groups, such as hydroxyl (−OH), carboxyl (R−COOH) and ether (–R–O–R–), which are inherently formed on all hard carbons due to oxygen present in the parent precursor used or due to air exposure. Likewise, other groups based on N, S, and F may exist within the HC structure. They are derived from precursor composition and/or external sources used to modify the material chemistry.

In this context, techniques such as X-ray photoelectron spectroscopy (XPS) and temperature-programmed desorption coupled with mass spectrometry (TPD-MS), often complemented by elemental analysis (EA), are widely used for HC surface chemistry evaluation.

It is pertinent to note that, because of the structural complexity and heterogeneous aspect of hard carbon, it is highly advised to combine the above approaches for better surface characterization, which can help optimize hard carbon anode synthesis and, therefore, electrochemical performance. XPS is a useful technique to investigate the chemical composition of hard carbon surfaces (~10 nm) and is commonly used to investigate the hybridization state of carbon atoms and oxygen atoms on HC surfaces, the presence of impurities, and chemical bonds.

Figure 16 presents the amount of O and C in different classes of hard carbon precursors with increasing temperatures of thermal carbonization. Clearly, as the pyrolysis temperature increases, the oxygen content decreases, while the carbon content increases for all materials. This behaviour is assigned to the removal of oxygenated species that leads to a reduction in the amount of C sp^3 and defect sites [196] and therefore an increase in C sp^2 carbon. Of note, elemental analysis and XPS can show different concentrations of elements due to the higher penetration depth of EA compared to XPS (i.e., few µm *vs.* few nm). However, as mentioned by Zhang et al. [75], the difference in O content on the surface and in the bulk may reveal the presence of oxygen gradient through the material.

As shown in Figure 16, biomass-derived HCs generally show a lower C content compared to biopolymers and carbons derived from synthetic polymers, which could be related to their higher inorganic impurities content and/or the lower initial carbon content present in the precursor structures. This can be detrimental to the electrochemical performance delivered by the HC anode material. For example, Rios et al. [135, 190] studied a wide palette of 25 biomass precursors that were grouped into three categories according to their main inorganic impurities: Ca for woody type, Si for grass-based ones, and K for agricultural precursors. For HC derived from wood (e.g., orchard apple, beechwood, and scot pine bark) and agricultural waste (e.g., corncob, papaya seed, and tamarind seed), the authors noted a high purity of C (>92 weight-moisture-free (wmf) %) and an ash content between 0.3 and 7.5 wmf %. However, most of the grass-based HCs studied (e.g., triticale, reed canary grass, and wheat straw) have a higher ash content (up to 24.8 wmf %), resulting in a lower purity of C (73.5–95.3 wmf %). This high ash content combined with low C amount proved to be detrimental to the electrochemical performance delivered by the HC anode material [135, 190].

However, Zhang et al. [91] noted that a washing step could be advantageous for improving the carbon content of HC derived from pinecones. Important removal of impurities (e.g., Mg, P, S, K, Ca and Si) was observed after washing the carbon with a solution of KOH for 3 h and HCl for 5 h. This resulted in a carbon content increase from 90.88 wt% to 94.43 wt%, and the oxygen level decreased as well from 7.82 wt% to 5.57 wt%. However, washing is only a partial solution as the main role of the inorganic impurities is played during the synthesis as it influences the structure of the HC itself (catalytic effect…), as explain above. In this direction [30], washing with hot water was proposed on pre-carbonized lignin materials at low temperature, and an increase in the C content with a simultaneous decrease in the amount of impurities were observed compared to unwashed HCs. This allowed the authors to enhance both the iCE and the capacity delivered and to improve the long-term cycling.

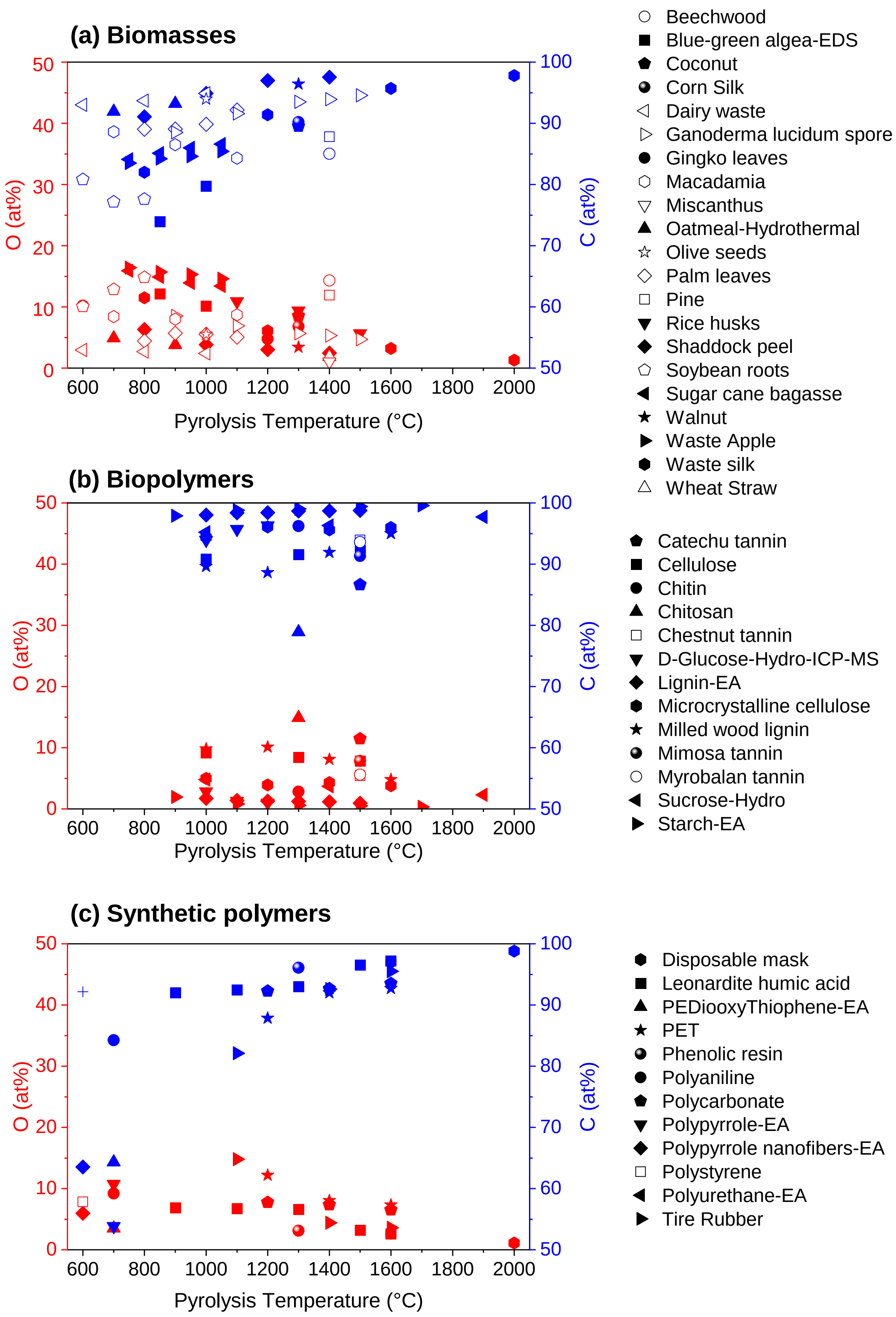

Figure 16: Hard carbon chemical composition: modification of the amount of oxygen and carbon with the pyrolysis temperature for the different classes of precursors: (a) biomasses, (b) biopolymers, and (c) synthetic polymers. Most values were obtained by XPS or EA, where indicated. The graphs were built based on the references presented in Tables 2 to 4.

In addition, Figure 16 shows that regardless of the source category, C and O concentrations vary in opposite ways and are dependent on precursors when the pyrolysis temperature is identical. For example, at 1400 °C, beechwood biomass [135] has ~85 at.% C *vs.* ~97 at.% for shaddock peel biomass [197], while for O, lower values are observed (~15 at.% *vs.* ~3 at.%). The same behaviour is observed among the biopolymers. For example, at 1500 °C, catechu tannin [189] contains 86 at. % C (and ~11 at.% of O) compared to ~98 at.% for starch [198] (and ~1 at.% O). Regarding the synthetic precursors, although less data are available in the literature, the same tendency was observed. For example, at 1600 °C, the percentage of C ranges from ca. 93 at.% (PET [169]) to approximately 98 at.% (leonardite humic acid [199]). As expected, the O content is very low as well between ~7 at. % (PET) and ~2 at.% (leonardite humic acid).

Functional groups other than oxygen-based groups have been investigated in the literature to boost the delivered capacity. For example, HC containing P-based functional groups was synthesized by Hong et al. [200] by using pomelo peels treated with phosphoric acid. However, the authors conclude that P-containing functional groups negatively affect sodium ion storage because of the dissolution of such groups in the electrolyte. Consequently, the obtained iCE was very low (27%), as was the capacity (181 mA h g^{-1} at 200 mA g^{-1} after 220 cycles). In another work [201], it was shown that electrochemical performance depends on the type of P-functional group, which could be modified with an increase in the pyrolysis temperature (500 to 1000 °C) from P - O to P - C and P - P bonds. The P-C groups proved to be the most efficient groups because they preserve a large interlayer space. Although the reversible capacity was high (379.3 mA h g^{-1} at 100 mA g^{-1}), the iCE was very low (~ 30%). Improvement in the iCE of P-doped carbons was achieved by Alvin et al. [202] by heating the materials at a higher temperature (1300 °C), allowing the suppression of micropores and defects, eventually reaching 72% iCE (*vs.* 69% for the undoped HC). An increase in the plateau capacity was also observed and was attributed to the enlargement of d_{002} due to P doping: 183 mAh g^{-1} for the undoped HC to up to 223 mAh g^{-1} P-doped HC).

A different approach involved N-doping by employing various nitrogen precursor sources to prepare HC. Therefore, Romero-Cano et al. [203] used precursors of grapefruit peels and impregnation with urea and melamine, followed by pyrolysis at 600 °C to achieve N functionalization. On the basis of the XPS results, the presence of common nitrogen functional groups (i.e., NH_2, pyridine-N and quaternary-N) was observed in different proportions. The impregnation of urea leads to the formation of a complementary N-group, i.e., pyridine-N-oxide.Wang *et al.* [204] prepared N-doped HC from polyimide separators recovered from spent

LIBs. The films were first washed with acetone to remove any impurities, and then annealed at temperatures between 800 °C and 1300 °C. The obtained materials possessed between 2 and 3.5 at. % N. However, the reversible capacity delivered in SIBs is rather low (190 mAh g^{-1} at a current density of 20 mA g^{-1}) and the iCE is less than 50%.

Doping hard carbons with different dopants can also be achieved by introducing different acids (e.g., H_3PO_4, H_2SO_4 or H_3BO_3) in the synthesis process, followed by pyrolysis at 1100 °C. Li et al. [205] prepared P, S, B-doped HCs through such an approach, to study the storage mechanism of Na-ions. They observed that the doping process brings modification to both the interlayer distance and the defect concentration of HCs. Another strategy to obtain doped materials is to mix the hard carbon with the dopant powder or with a compound containing the dopant. Muruganantham and co-workers [206] prepared N- and S-doped HC by using a two-step synthesis procedure. First, mango peel was pyrolysed at 1000 ° C and washed with an acidic solution. Second, the obtained HC was ground with sulphur powder and hexamethylenetetramine ($C_6H_{12}N_4$), then treated at 800 ° C for 2 h under Ar. As a result, the d-spacing of the N, S- doped HC increased to 0.48 nm compared to the pristine HC (0.38 nm).

Therefore, XPS provides useful information about chemical surface species and their states. However, XPS spectra deconvolution and interpretation are highly challenging and require advanced knowledge to correctly identify the chemical species present on the HC surface.

To strengthen carbon surface analysis investigations, TPD-MS is a complementary advanced tool to probe the nature and quantify oxygen function groups and active surface area (ASA, more details in Section 3.5.2) in hard carbon materials. Briefly, the fundamental principle of the analysis is to heat the carbon under a secondary vacuum and record the spectra of desorbed gases (i.e., CO, CO_2, H_2O, and H_2) as by-products of the decomposition of functional groups using quadrupole mass spectrometry [207]. Although this technique has been widely used by several groups for activated carbon characterization [208-210], only one group [40, 98] reported results on various hard carbons.

The evaluation of CO and CO_2 gases is of high importance because they offer valuable information on the different functional groups present, according to the release temperature, as presented in Figure 17 (top). CO_2 desorbs at rather low temperatures (<500 °C) from various oxygen-containing functional groups, such as carboxylic, anhydride, and lactone groups. Instead, CO is desorbed at higher temperatures (>500 °C) from oxygen-containing functional groups, such as carbonyl, phenol, ether, and quinone groups [154, 211, 212]. When the two types of groups are summed (i.e., $CO+CO_2$), the CO_x groups can be obtained to provide a global view of the O-based functionalities of hard carbon.

Figure 17 (bottom) shows that the amount of COx varies greatly with the precursor type and the annealing temperature. One can observe a higher amount of CO_x for some biomass-derived HCs (e.g., potato (~2.5 mmol g^{-1}) and asparagus (~1.5 mmol g^{-1})), which is highly related to the presence of metallic carbonates [137], as revealed by the presence of unusual CO_2 and CO peaks at both low (ca. 300 °C) and high (500-800 °C) desorption temperatures. In fact, the amount of CO_x was shown to be decreased by 13% and 50% for asparagus and potato HCs, respectively, by washing the hard carbon [137]. The same behaviour was reported by Conder et al. [29], where HCl treatment of chitosan-derived HC led to a reduction in CO_x desorbed molecules compared to the untreated sample (from 0.07 mmol g^{-1} to 0.03 mmol g^{-1}). Apart from these 2 HCs, the materials presented in Figure 17 possess CO_x amounts that are lower than 1 mmol g^{-1}, and biopolymers stand out for the lowest values. Some synthetic polymers (PAN) present a very low amount of CO_x-based groups because of their chemical composition, which does not contain oxygen. Similar was reported for a commercial HC, named PAC-2 (Aekyung Petrochemical), which released a low amount of CO_x, i.e., 0.07 mmol g^{-1}, however, neither the precursor used nor the synthesis conditions are available [98].

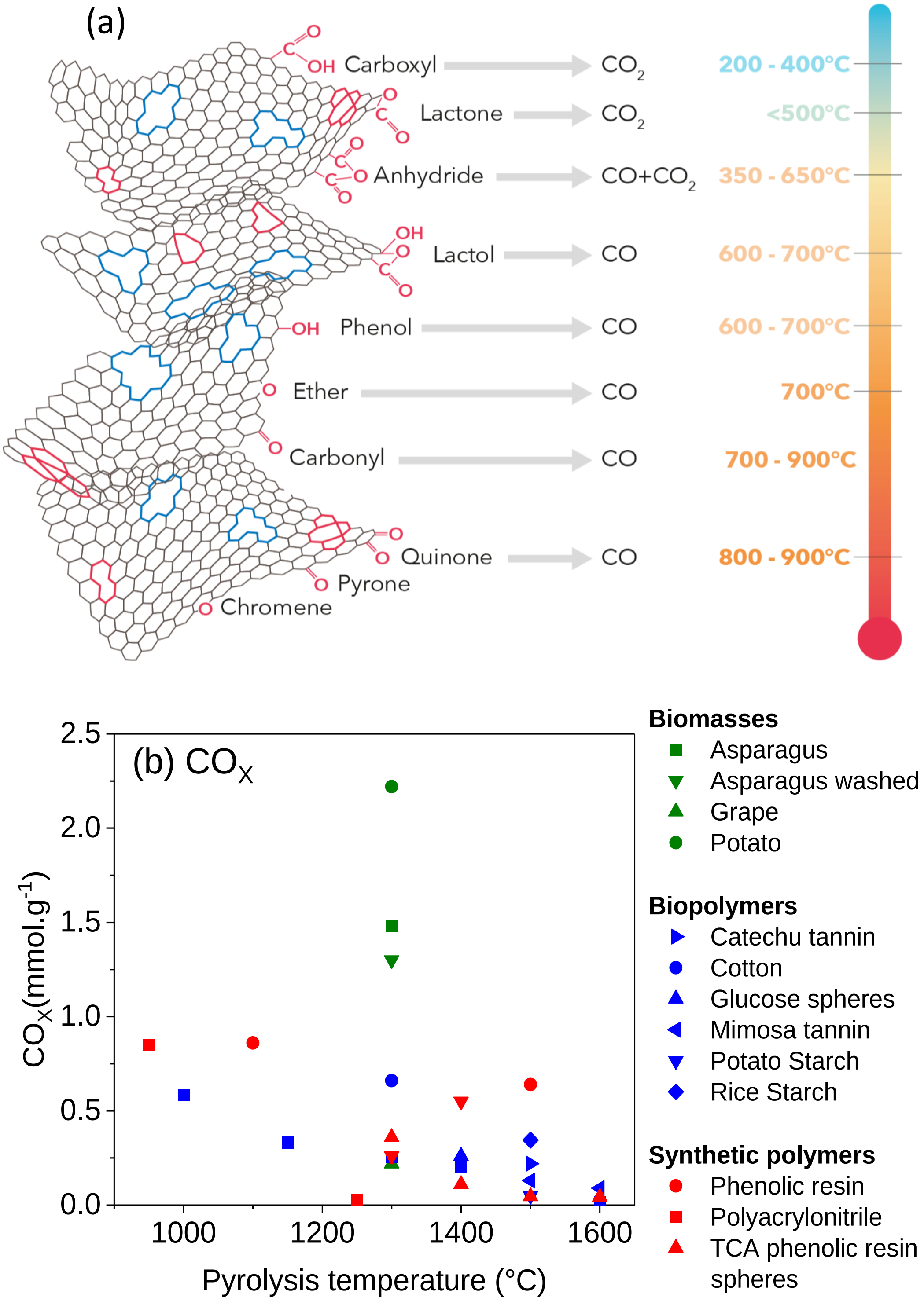

Figure 17: (top) Oxygen-based functional groups evolved from the carbon surface and their decomposition at different temperatures: CO and CO_2 groups, as proposed by the authors of this work, (bottom) Desorbed amount of CO_x derived from the thermal decomposition of oxygen-functional groups during the TPD-MS experiment from hard carbon materials obtained by different precursors pyrolyzed at various temperatures. The graphs were built based on the references presented in Tables 2 to 4.

In addition to precursor type, the pyrolysis temperature has an important impact on the control of HC functionality. For the same precursor origin (cellulose, phenolic resin, etc.), the increase in temperature leads to a reduction in the amount of CO_x, which was proven to be favourable for electrochemical performance, improved iCE, and reversible capacity [40, 98]. Another efficient strategy approached in the literature to reduce the amount of CO_x is a washing step involving either acid or water, which can be performed prior to or after annealing treatment [29, 30, 137].

3.5 Hard carbon structural defects

As mentioned in the Introduction, hard carbons have a disordered and non-graphitizing structure, including curved and randomly aligned graphene sheets with a microporous texture. In particular, distinct Na-ion storage properties (e.g., specific reversible capacity and stability [40, 43, 213]) can be obtained despite the identical structure of the hard carbon precursors as a result of tuning the defect concentration [214]. Consequently, an in-depth investigation of these defects is crucial for electrochemical applications.

Various defects could be present in the HC structure, including Stone–Wales (SW) defects, mono-, di-, and/or multiple vacancies, and line defects. These defects are also known as intrinsic defects or self-doping defects. Stone–Wales (SW) defects are caused by the rearrangement of the carbon lattice, in which the rotation (90°) of two π-bonded carbon atoms in the same plane leads to the formation of carbon polygons other than hexagonal rings, such as heptagons or pentagons [215, 216], as shown in Figure 18.a.

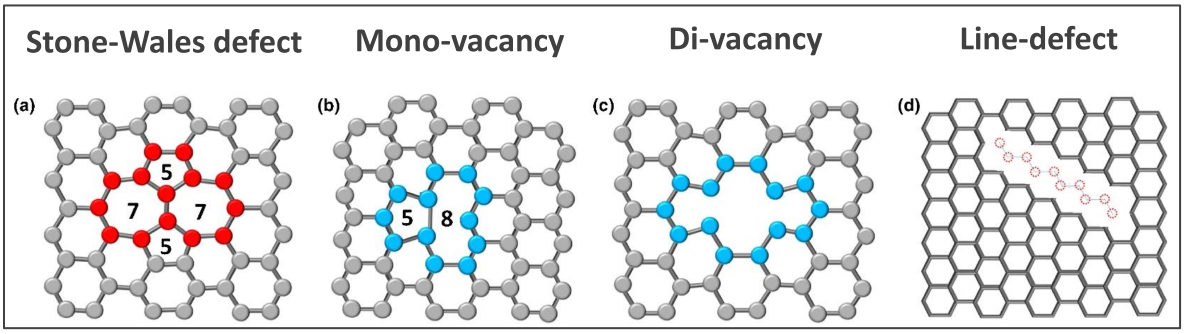

Figure 18: Different types of defects present in the hard carbon structure: Stone–Wales defect (a) mono-vacancy (b) di-vacancy (c) line defect (d). Reprinted from [215] under the terms of CC BY-NC-ND 4.0 DEED licence.

Vacancy defects are another type of natural crystal imperfection that belongs to the point defect group and originates from the absence of carbon atoms from the ideal graphene lattice. When one carbon atom is missing, a pentagon and an octagonal ring appear, the latter presenting a dangling carbon bond (unsaturated atomic valence of C); see Figure 18.b.

However, the di-carbon vacancy may or may not have a dangling carbon bond; see Figure 18.c. It should be noted that dangling carbon bonds are very reactive and may serve as sites for the functionalization of hard carbon structures. Line defects are hard carbon imperfections caused by vacancy defects [215]. As the name suggests, they occur in the carbon atom plane as aligned point defects with or without dangling bonds [217]; see Figure 18.d. Edge defects can also be present in hard carbon, considering that the graphene layer is terminated by edge atoms that are free or passivated with hydrogen atoms. Edges in the zigzag or armchair direction are commonly observed and are very reactive [218].

Regarding the effect of defects on electrochemical behaviour, Olsson et al. [214] demonstrated, through DFT simulations, that sodium ion storage may be considerably affected positively and negatively by structural defects. The authors showed that the presence of defective sites may increase the adsorption of Na^+ and improve the sodiation process. The same observations were confirmed by Wang et al. [219] for lithium-ion batteries. Furthermore, Yoon et al. [220] suggested that a high concentration of defects may result in a high capacity for sodium batteries. Interestingly, for the anode–electrolyte contact and the sodiation phenomena, the location of defect sites is crucial and should be fully considered. On the negative side, highly energetic defective sites might result in a metal trapping effect, resulting in poor electrochemical performance [214]. These results show that controlling the nature and location of defects is critical to achieving improved electrochemical performance.

The most common characterization techniques for studying the structural defects in hard carbons are Raman spectroscopy and TPD-MS. Both of these techniques give different but complementary information. Raman spectroscopy provides qualitative information on the internal organization of the carbon and the degree of disorder (thorough I_D/I_G ratio), while TPD-MS provides quantitative information on the total number of active sites (comprising defects) present in the hard carbon structure by determining the active surface area (ASA).

3.5.1 Probing local carbon structure with Raman spectroscopy

Raman spectroscopy is a local and non-destructive chemical examination technique that offers comprehensive information regarding the structure of HC and is commonly used as a structural analysis auxiliary to XRD and TEM. Raman spectroscopy has proven to be the most sensitive method for investigating the disorder in sp^2 of diverse carbon structures, making it an essential technique for characterizing hard carbon materials. In a typical hard carbon Raman spectrum, two important peaks are identified, D and G, in the visible wavelength range. The G band (referring to graphite) is located at approximately 1600 cm^{-1} and relative to the in-plane optical phonon modes of carbon with a sp^2 hybridized atomic orbital (C–C) [221, 222]. The D-band, located at approximately 1350 cm^{-1}, is the result of the breathing modes of carbon rings [221, 222]. This band, known as the disorder band, appears exclusively when the carbon ring is adjacent to a defective zone (sp^3 carbon) [223]. The area/intensity ratio of D and G bands (I_D/I_G) can be used as an indicator of the level of disorder/defects in HCs. In other words, this parameter is related to the ratio of sp^3 and sp^2 carbon. Importantly, the I_D/I_G ratio is dependent on the laser excitation frequency, especially the sp^2 carbon, which might affect the observed results [224, 225]. Moreover, different ways of calculating the ratio are reported in the literature, making a fair comparison of the available data difficult: i) by implying the area under the peaks, ii) by implying the intensity of the peaks, iii) using the I_D/I_G ratio, and iv) using the I_D/I_D+I_G ratio or even $FWHM_D/FWHM_G$. The area under the peaks is more accurate and recommended since it considers peak width [222, 226].

Figure 19 shows the variation in the I_D/I_G ratio with temperature for hard carbon derived from various precursors. The I_D/I_G ratio decreases as the pyrolysis temperature increases, regardless of the precursor source. However, for a few materials heat-treated below 1000 °C, the trend is the opposite, i.e., macadamia [65], soybean roots [227], cellulose [31], and phloroglucinol spheres [98]. This is caused by the structural changes during the thermal treatment that occur in two distinct regimes: i) the initial pyrolysis phase (600–1000 °C) in which the I_D/I_G ratio increases often due to the release of precursor heteroatoms and ii) the "pseudo-graphitization" phase (> 1000 °C) in which the I_D/I_G ratio usually decreases as the temperature rises, which is related to carbon ordering (sp^2) enhancement.

Qiu et al. [46] reported that increasing the pyrolysis temperature of cellulose from 900 °C to 1500 °C yields HC with a decrease in the (I_D/I_D+I_G) ratio from 0.65 to 0.58, further confirming the reduction in defect content. Yang et al. confirmed [198] the same behaviour. When increasing the pyrolysis treatment from 900 °C to 1700 °C, a clear decrease in I_D/I_G from 1.35 to 1.04 was observed for spherical hard carbon derived from starch. Furthermore, Xiao et al. [228] showed that the pyrolysis rate may have a significant effect on the growth of carbon planes. The authors indicated that the (I_D/I_D+I_G) ratio of hard carbon prepared from sucrose at 1300 °C was reduced from 0.76 to 0.65 as the pyrolysis ramp decreased from 5 °C min^{-1} to 0.5 °C min^{-1}. This result was attributed to the formation of integrated hexagonal carbon rings with lower defective basal planes at a low pyrolysis rate. In addition, Wang et al. [229] demonstrated that acidic treatment (e.g., H_2SO_4) can reduce the I_D/I_G ratio from 2.7 to 2.1 for hard carbon produced from Platanus biomass. Marino et al. [82] investigated the impact of several atmospheres (Ar, N_2, and Ar/H_2) on the properties of hard carbon derived from lignin-based bio-waste. The authors deconvoluted the Raman spectra according to the procedure of Sadezky et al. [226] and found that the A_{D3}/A_G ratio was smaller when hard carbon was treated under a reducing atmosphere (Ar/H_2), suggesting fewer adsorbed molecules on the surface.

In addition to the temperature and synthesis conditions, the precursor source used has an impact on the I_D/I_G ratio. In Figure 19, slightly higher I_D/I_G ratios can be seen when biomass precursors are used to prepare HC compared to those of biopolymers and synthetic polymers. This is mainly a result of the high impurity content and the presence of heteroatoms in biomass precursors. The latter has an impact on the degree of graphitization and sometimes leads to heterogeneous structures (disordered and highly graphitized) [102, 137]. In such cases, the acquisition of Raman spectra in different zones is needed, as is the analysis of second-order Raman peaks, such as the 2D (also called G') peak (~ 2700 cm^{-1}), which provides information on the graphite regions.

Heteroatom doping (P [205], B [230], S [231], N [232], F [93], etc.) can be used to intentionally alter the local structure of hard carbons, with the aim of enhancing the electrochemical storage capability in SIBs. Recently, Li et al. [205] examined the effects of P, B, and S heteroatoms on the turbostratic nanodomains of a hard carbon derived from sucrose. Compared to undoped HC (1.30 ratio), phosphorus doping increased the I_D/I_G ratio to 1.39, boron presence led to a decrease in the I_D/I_G ratio to 1.15, and S doping led to a similar result as boron (1.18 ratio). These findings were consistent with the structural TEM observations. When P heteroatoms are introduced, smaller or more curved graphene sheets appear, while B drives the appearance of large areas of graphitic layers.

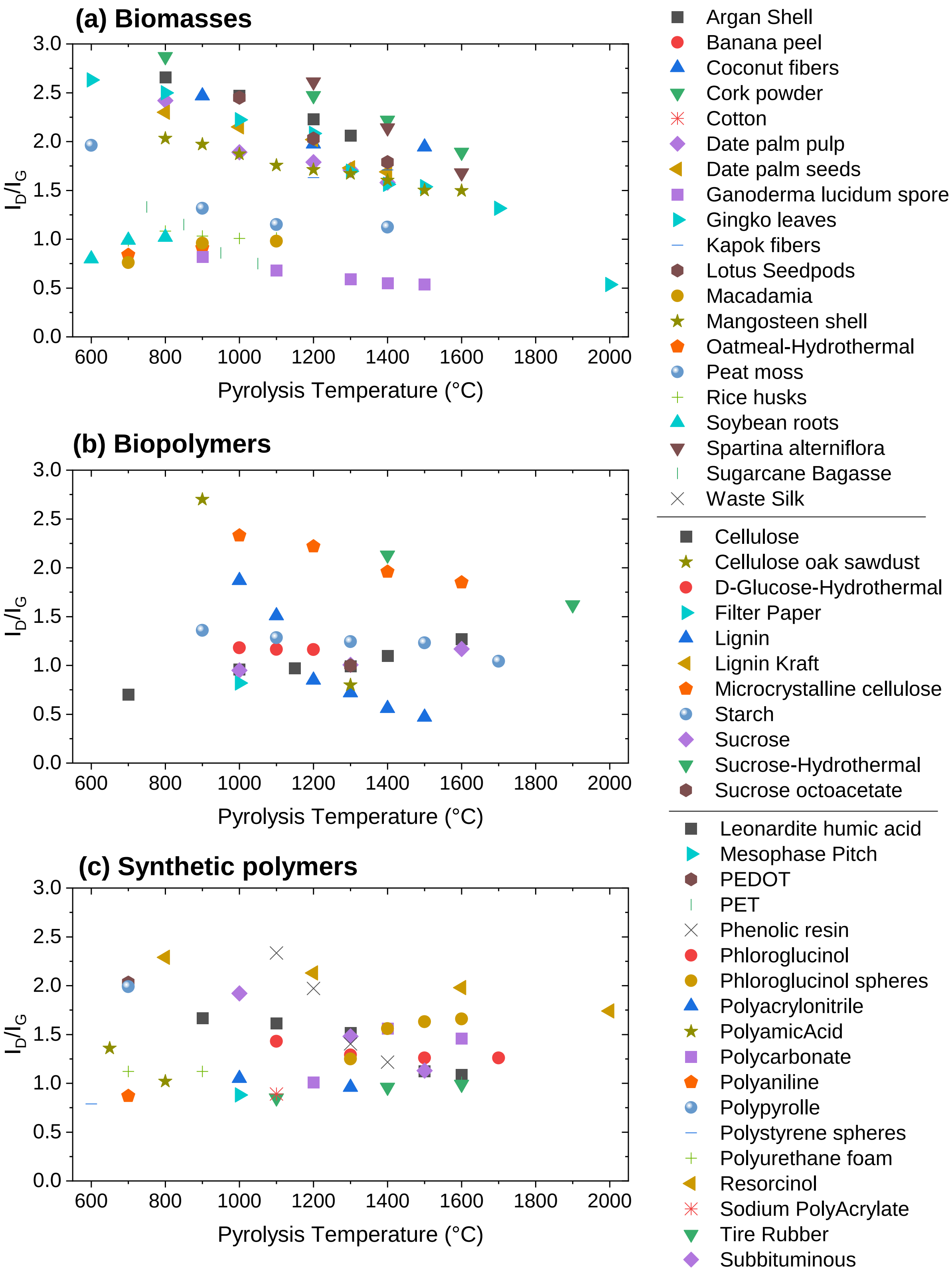

Figure 19: Evolution of the I_D/I_G ratio with pyrolysis temperature for the different classes of precursors: (a) biomasses, (b) biopolymers, and (c) synthetic polymers. The graphs were built based on the references presented in Tables 2 to 4.

]]>

Regarding the effect on the electrochemical performance, P and S doping led to an increase of the reversible capacity delivered: 359 mAh g^{-1} for P-HC and 328 mAh g^{-1} for S-HC compared to 283 mAh g^{-1} for the pristine HC. In the case of B doped HC, the capacity observed was very low, 147 mAh g^{-1}, along with a low iCE of 36% only. The authors linked the high-energy in-plane “defect” sites inside turbostratic nanodomains to the poor performance. Agrawal et al. [232] also observed an increase in disordering of the HC structure after nitrogen doping. Moreover, the authors stated that such an increase may facilitate the reaction sites for the Na ion. Indeed, the electrochemical performance delivered by the doped materials confirmed this assumption. The reversible capacity improved from 205 to 266 mAh g^{-1} for N doped micron-sized HC and from 230 to 286 mAh g^{-1} for N doped nano-sized HC. An improvement was observed for the iCE, as well. Similarly, Wu et al. [230] observed that doping HC with boron heteroatoms (based on glucose precursor) increases the degree of disorder from 2.66 (undoped HC) to 3.05 I_D/I_G ratio. Contrary to the previous study, Wu and co-authors found that B doping increases the reversible capacity delivered by the HC in the first cycle, from ~175 mAh g^{-1} (pristine HC) to 230 mAh g^{-1} (B doped HC).

Fluorine, a highly electronegative element, also proved to be an efficient dopant to tune the HC structure and to lower the energy barrier for Na^+ insertion [233]. Kong et al. [166] reported a pretreatment method (4 h in a reacting stove under F_2/N_2 gas) for F doping to induce more defects in the HC structure. By varying the reaction temperature from 50 °C to 150 °C, the I_D/I_G ratio increased from 1.01 (undoped HC) to 1.07 for the HC doped at 150 °C. Other similar strategies imply the use of multiple dopants (typically two, (N/S [234], S/P [235], and B/P [236]) to obtain a synergistic effect, but this route is rather rarely approached. For instance, Qin et al. [237] developed HC from corn stalks and doped it with both nitrogen and phosphorus. As revealed by the I_D/I_G ratio, this strategy led to a higher number of structural defects with 1.69 for N/P-doped HC *vs.* 1.56 for undoped HC.

As shown from these examples, it is complicated to compare the I_D/I_G absolute values from different articles. Due to the different ways of calculating them, only their tendency can be compared. According to the findings presented above, the final I_D/I_G value is strongly influenced by the pyrolysis conditions (i.e., temperature, heating rate, atmosphere, dopants, etc.) as well as the hard carbon resources used.

3.5.2 Active surface area (ASA) determined by TPD-MS

Raman analysis is an essential technique for the structural investigation of hard carbons, but the evaluation of defects based on the I_D/I_G ratio is qualitative only, and in addition, it does not take into account microporosity-induced defects. Moreover, the multiple ways of calculating the I_D/I_G ratio make the comparison of the results difficult. A powerful approach to derive the quantitative evaluation of hard carbon defects/active sites is the determination of the active surface area (ASA) by TPD-MS, which is associated with chemically accessible and reactive sites that allow covalent bonds [238]. More precisely, ASA includes the areas of different carbon edge planes and the defects (i.e., dislocations, vacancies, point defects and Stone–Wales defects) [239, 240]. To distinguish it from the total specific surface area (TSA, called also SSA), one should consider that SSA determined by gas adsorption comprises both the basal planes and the edge planes/defects (ASA), as illustrated in Figure 20.a. To assess the ASA, the surface of HC that was previously "cleaned" (oxygen-based functional groups removed under a secondary vacuum) was exposed to oxygen chemisorption (300 °C). The newly formed surface oxygenated groups were quantified by TPD-MS, and the active surface area was determined. More precisely, ASA formula considers the amount of CO and CO_2 desorbed during TPD-MS (up to 950 °C) and the area of an edge carbon site, assuming that : i) the effective area of a carbon atom edge is 0.083 nm^2 , ii) the edge carbons lie in the (100) plane, and that iii) only one bond is formed between oxygen and the edge carbon [40, 180].

Figure 20.b presents an overview of the data available in the literature on ASA for HC materials. This technique is very particular, and few laboratories have it available. One may observe that ASA is highly influenced by both pyrolysis temperature and precursor origin, with the reported ASA values between ~53 m^2 g^{-1} (potato peel at 1300 °C [137]) and 0.36 m^2 g^{-1} (polyacrylonitrile at 2800 °C [75]). In general, as the pyrolysis temperature increases, the ASA of hard carbons decreases, as is the case for cellulose precursors [40] (from 44 to 1 m^2 g^{-1} when the temperature varied from 1000 °C to 1600 °C) or phenolic resin spheres [98] (from ~12 to 1.3 m^2 g^{-1} when temperature increased from 1300 °C to 1600 °C). In effect, high-temperature pyrolysis can minimize the number of active sites in the material by minimizing structural imperfections and promoting the formation of pseudo-graphitic nanodomains. These findings were confirmed by Zhang et al. [75] using a polyacrylonitrile polymer as a hard carbon nanofiber precursor. When the pyrolysis temperature was increased from 950 °C to 2800 °C, the ASA value was significantly reduced from 23 m^2 g^{-1} to 0.36 m^2 g^{-1}. The authors attribute this tendency to the

increase in structural organization, which is possible at high pyrolysis temperatures (≥ 2000 °C), as sustained by the TEM micrographs.

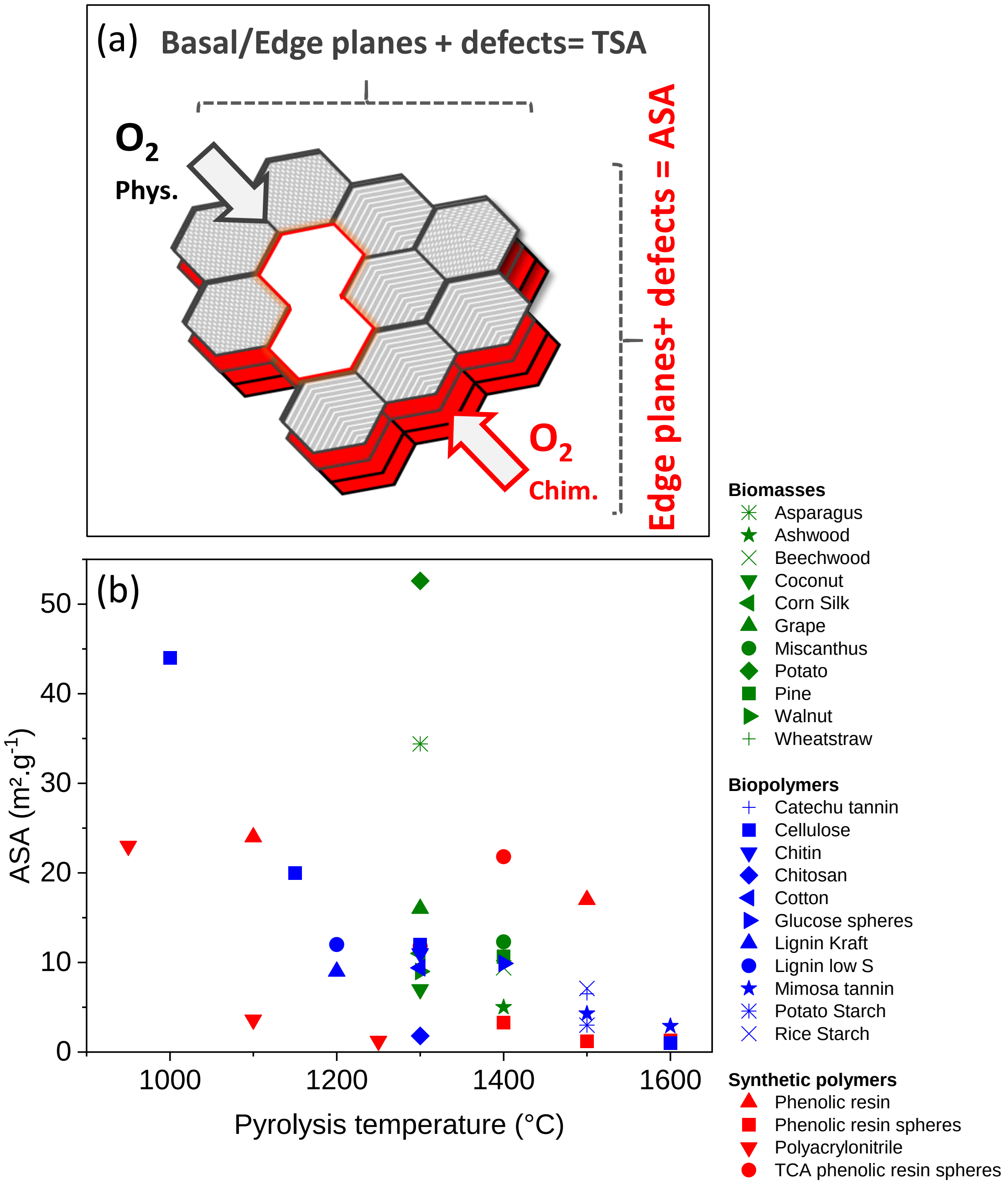

Figure 20: (a) Schematic representation of a hard carbon crystallite showing the total surface area (TSA- related to basal and edge planes) and active surface area (ASA – related to edge planes and defects). Reproduced under the terms of CC BY-NC 3.0 DEED licence [180], Copyright 2022, The Authors, Published by Royal Society of Chemistry. (b) Active surface area obtained by oxygen chemisorption and subsequent TPD-MS analyses on hard carbon materials obtained at different pyrolysis temperatures. The graphs were built based on the references presented in Tables 2 to 4.

Moreover, the values of ASA depend greatly on the precursor type since each material has a unique composition and a particular structure. For example, precursors exempt from oxygen result in lower ASA values, i.e., 0.6 m^2 g^{-1} for polyacrylonitrile [75] versus 17 m^2 g^{-1} for phenolic resin [185] rich in oxygen functionalities, with both treated at 1500 °C. The gap in ASA induced by the precursors can reach ~98% at low temperatures (< 1400 °C) when comparing a biomass (~53 m^2 g^{-1} for potato [137]) with a synthetic polymer (~1.2 m^2 g^{-1} for polyacrylonitrile [75]) heat treated at a similar temperature (~ at 1300 °C)). This difference tends to decrease at high temperatures (>1500 °C). For example, the series of biopolymers treated at 1500 °C present ASAs between 7.1 and 1.3 m^2 g^{-1} [115, 174].

Since each material has unique structural and chemical composition features, this wide range of ASA values demonstrates that this parameter is an intrinsic property of each material. Ghimbeu's team noted that for the same pyrolysis temperature (i.e., 1400 °C), the existence of heteroatoms in the structure of hard carbon precursors (e.g., N, S) leads to higher ASA values (i.e., 21.8 m^2 g^{-1} for TCA phenolic resin), in contrast to precursors that include only oxygen (i.e., 3.3 m^2 g^{-1} phenolic resin spheres) [180]. This observation is in line with the Raman studies presented above showing an increase in the I_D/I_G ratio for doped carbon materials. A significant impact of metal-based impurities present on the structure of the precursors on ASA values was also highlighted [137]. Such metal impurities might induce the formation of metallic oxides during O_2 chemisorption, which further reacts with carbon during the TPD-MS measurement, releasing important amounts of additional CO_X gas. To address this issue, a washing treatment prior to or after pyrolysis was proposed [137], and it proved to be efficient in certain cases. For example, the ASA value of an HC produced from potato peel waste was reduced from 52.6 m^2 g^{-1} to 43.3 m^2 g^{-1} when washing was performed after heat treatment and to 11.5 m^2 g^{-1} when washing was done prior to heat treatment.

The determination of ASA for HC is essential in terms of understanding and optimizing Na storage in HC anodes. Recently, it was shown that there is a strong correlation between the active surface area and the irreversible capacity observed in the first cycle [180]. More precisely, when the ASA is reduced, the initial irreversible capacity decreases considerably, which makes this HC feature of great interest.

Table 2: Literature review of hard carbon materials derived from biomass: precursors used and physico-chemical and electrochemical performance

Hard carbon synthesis		**Hard carbon properties**				**Hard carbon testing conditions**			**Hard carbon performance**			**Refs.**
Precursor	**TT (°C)**	**d_{002} (Å)**	**N_2 SSA (m^2 g^{-1})**	**CO_2 SSA (m^2 g^{-1})**	**O % (at. %)**	**Formulation**	**Electrolyte**	**Current density**	**iCE (%)**	**1st cycle insertion capacity (mAh g^{-1})**	**1st cycle reversible capacity (mAh g^{-1})**	
Alnus	1400	3.88	21.5	26.5	-	90-5-5 HC, PVDF, CB	1M $NaPF_6$ in EC:DMC, 1:1, 1.5 % FEC	37.2 mA g^{-1}	74-85	270-376	200-313	[102]
Almond Shells	1000	4	21-252	-	-	90-10 HC, CMC	1M $NaPF_6$ in EC:DEC, 1:1	30 mA g^{-1}	47-83	270-318	128-260	[82]
Apple waste	1100	3.77	1.54	-	7.8	80-10-10 HC, CMC, CB	1M $NaClO_4$ in EC:PC, 1:1	20 mA g^{-1}	83	390	330	[241]
Argan shell	800-1300	3.91-3.85	99-2.6	-	-	90-10 HC, PVDF	1M $NaPF_6$ in EC:DEC, 1:1	25 mA g^{-1}	63-82	350-372	232-286	[24]
Artemia cyst	1300	3.72-3.8	6.9-285.8	-	7.3-13.5	80-10-10 HC, PVDF, CB	1M $NaClO_4$ in EC:DEC, 1:1	25 mA g^{-1}	70	400-460	280-320	[84]
Asparagus peel	1300	3.82	7	140	16.3	70-10-20 HC, PVDF, CB	1M $NaPF_6$ in EC:DMC, 1:1	37.2 mA g^{-1}	46	390	180	[137]
Bagasse	1400	3.74	19	338	-	80-10-10 HC, PVDF, CB	1M $NaPF_6$ in EC:DMC, 1:1, 1.5% FEC	37.2 mA g^{-1}	76	374	284	[135]
Banana peel	800-1400	3.97-3.84	33-14.5	-	-	80-10-10 HC, PVDF, CB	1M $NaClO_4$ in EC:DEC, 1:1	50 mA g^{-1}	67.8	523	355	[126]
Beechwood	1000-1400	3.99-3.75	16-4.8	338-35	14.31	80-10-10 HC, PVDF, CB	1M $NaPF_6$ in EC:DMC, 1:1, 1.5% FEC	30 mA g^{-1}	65-82	244-393	190-315	[190]
Blue-green algae	850-1000	-	-	-	12.1-10.1	80-10-10 HC, PVDF, CB	1M $NaClO_4$ in EC:DEC, 1:1	20 mA g^{-1}	47-53	300-462	157-234	[242]

Camphor wood	1000	3.90	678	-	-	70-15-15 HC, CMC, CB	1M $NaClO_4$ in PC, 5% FEC	100 mA g^{-1}	33.7	785.9	264.9	243
Coconut fibres	900-1500	3.87-3.86	524-67	-	-	80-10-10 HC, PVDF, CB	1M $NaClO_4$ in EC:DMC, 1:1	C/10	66-86	292-441	270-344	42
Coconut husk	1400	3.78	14	60	-	80-10-10 HC, PVDF, CB	1M $NaPF_6$ in EC:DMC, 1:1, 1.5% FEC	37.2 mA g^{-1}	76	381	291	135
Coconut shell	1300	3.75	7	15	8.5	80-10-10 HC, PVDF, CB	1M $NaPF_6$ in diglyme	25 mA g^{-1}	63	463	294	154
Conifer	1400	3.91	16	21.3	7.4	90-5-5 HC, PVDF, CB	1M $NaPF_6$ in EC:DMC, 1:1, 1.5 % FEC	37.2 mA g^{-1}	82	350	287	102
Cork powder	800-1600	4.03-3.76	11.7-5.5	-	-	90-5-5 HC, Na Alginate, CB	1M $NaPF_6$ in EC:DMC, 1:1	30 mA g^{-1}	71-87	289-450	252-351	149
Corn silk	1300	3.68	10	23	6.8	80-10-10 HC, PVDF, CB	1M $NaPF_6$ in diglyme	25 mA g^{-1}	62	313	273	154
Cotton	1300	4.0	119	386	2.9	100 HC	1M $NaPF_6$ in EC:DEC, 1:1	37.2 mA g^{-1}	63.5	284	260	213
Dairy waste	600-1000	3.7-3.6	-	-	2.4	80-10-10 HC, PVDF, CB	1M $NaClO_4$ in EC:PC, 1:1	50	30.7	485	149	244
Date palm pulp	800-1400	3.82-3.76	225.9-33.3	-	-	97-3 HC, PANa	1M $NaPF_6$ in EC:DEC, n.a.	25 mA g^{-1}	71 - 88	304 - 327	207-300	39
Date palm seeds	800-1400	3.86-3.71	115.6-34.7	-	-	97-3 HC, PANa	1M $NaPF_6$ in EC:DEC, n.a.	25 mA g^{-1}	71 - 88	304 - 327	207-300	39
Fraxinus	1400	3.81	5	6.9	-	90-5-5 HC, PVDF, CB	1M $NaPF_6$ in EC:DMC, 1:1, 1.5 % FEC	37.2 mA g^{-1}	83	362	301	102
Ganoderma lucidum spore	900-1500	3.79 - 3.68	329.6-12.7	-	8.52-4.69	80-10-10 HC, PVDF, CB	1M $NaClO_4$ in EC:PC, 1:1	20 mA g^{-1}	25-72	392-483	104-283	245
Gingko leaves	1200-2500	4.01-3.35	242-16	-	4.77-2.05	90-10 HC, PVDF	1M $NaClO_4$ in EC:DEC, 1:1	30 mA g^{-1}	37-58	300-750	120-400	167
Grape waste	1300	3.79	6	19	23.9	70-10-20 HC, PVDF, CB	1M $NaPF_6$ in EC:DMC, 1:1	37.2 mA g^{-1}	67	227	153	137
Grapefruit peels	600	3.8	3.2-10.9	-	9.8-18.6	80-10-10 HC, PVDF, CB	1M $NaPF_6$ in EC:PC:DMC, 1:1:1	37 mA g^{-1}	21-41	67-427	14-176	203
Kapok fibers	1200-1400	3.9-3.8	-	-	8.3-5.3	95-5 HC, CMC	1M $NaClO_4$ / $NaPF_6$ in EC:DMC, 1:1	30 mA g^{-1}	79-80	289-366	228.7-292.5	246

Longan	1350	-	6-268.1	-	-	90-5-5 HC, PVDF, CB	1M $NaClO_4$ in EC:PC, 1:1	25 mA g^{-1}	53-88	335-394	183-310	247
Lotus leaves	1000	3.72	250 - 365.5	-	-	80-10-10 HC, DMF, CB	1M $NaClO_4$ in PC:DEC, 1:1	50 mA g^{-1}	65-72	387-402	260-289	248
Lotus seedpods	1000-1400	3.91-3.70	751.6-108.8	-	-	80-10-10 HC, PVDF, CB	1M $NaClO_4$ in PC, 2% FEC	50 mA g^{-1}	35-50	430-650	150-329	182
Lumber	1000-1400	-	262.8 - 716.9	-	-	80-10-10 HC, PVDF, CB	1M $NaPF_6$ in EC:DEC, 1:1	100 mA g^{-1}	20-66	165-436	60-146	249
Macadamia nut Shell	1200-1600	-	469-0.8	-	-	95-5 HC, Na-alginate	1M $NaPF_6$ in EC:DMC, 1:1, 2% FEC	C/10	65-91	310-325	200-301	65
Magnolia	1200	3.9	95.7	-		80-10-10 HC, CMC, CB	1M $NaClO_4$ in PC, 5% FEC	30 mA g^{-1}	69.4	453.9	315	250
Mangosteen shell	800-1600	3.84-3.66	539.4-2.4	-	-	80-10-10 HC, waterlock , CB	1M $NaClO_4$ in EC:PC, 1:1	20 mA g^{-1}	22-86	350-390	70-330	25
Miscanthus	1000-1400	-	11-12	438-29	1.04	80-10-10 HC, PVDF, CB	1M $NaPF_6$ in EC:DMC, 1:1, 1.5 FEC	30 mA g^{-1}	65-82	244-393	190-315	190
Oak seeds	900-1100	4-3.79	26.5	-	-	80-10-10 HC, PTFE, CB	1M $NaClO_4$ in EC:PC, 1:1, 5% FEC	50-100 mA g^{-1}	33-52	440-1275	230-431	251
Oatmeal-Hydrothermal	700-900	3.91-3.88	74.4-22.8	-	4.9-3.8	80-10-10 HC, PVDF, CB	1M $NaClO_4$ in EC:DMC, 1:1	50 mA g^{-1}	33-56	225-825	75-320	252
Olive seeds	1000	3.84	-	-	5.49	80-10-10 HC, PVDF, CB	1M $NaClO_4$ in EC:DEC, 1:1	25 mA g^{-1}	28-39	393-490	128-152	253
Palm leaves	800 - 1100	3.88	20.5-6.21	-	4.42-5.05	80-10-10 HC, PVDF, CB	1M $NaClO_4$ in EC:DEC, 1:1	25 mA g^{-1}	45-62	518-652	264-364	253
Papaya seed	1400	3.77	10	8	-	80-10-10 HC, PVDF, CB	1M $NaPF_6$ in EC:DMC, 1:1, 1.5% FEC	37.2 mA g^{-1}	71	359	256	135
Peanut shell	1000 -1600	4.15-3.92	309-24	-	-	80-10-10 HC, CMC:polyacrylic ester, CB	1M $NaPF_6$ EC:DEC:DMC, 1:1 :1	20 mA g^{-1}	50-86.8	335-380	168-312	83
Peat moss	600-1400	3.98-3.82	55.3-20.8	-	-	80-10-10 HC, CMC:polyacrylic ester, CB	1M $NaClO_4$ in EC:DEC, 1:1	25 mA g^{-1}	64-68	441-564	30-372	92

Pine	1200-1400	3.78-3.76	141-5	18-66	11.91	80-10-10 HC, PVDF, CB	1M $NaPF_6$ in EC:DMC 1:1, 1.5% FEC	30 mA g^{-1}	65-82	244-393	190-315	190
Poplar	1400	3.68	11	0.5	-	80-10-10 HC, PVDF, CB	1M $NaPF_6$ in EC:DMC, 1:1, 1.5% FEC	37.2 mA g^{-1}	75	365	274	135
Populus	1400	3.81	5	6.9	-	90-5-5 HC, PVDF, CB	1M $NaPF_6$ in EC:DMC, 1:1, 1.5 % FEC	37.2 mA g^{-1}	83	362	301	102
Potato peel	1300	3.98	11.5	127	11.7	70-10-20 HC, PVDF, CB	1M $NaPF_6$ in EC:DMC, 1:1	37.2 mA g^{-1}	67	317	214	137
Rice husks	1100-1500	4.03-3.84	265-218	-	10.9-5.6	80-10-10 HC, PVDF, CB	1M $NaClO_4$ in EC:DC, 1:1	25 mA g^{-1}	64-68	441-564	300-372	89, 133
Salix	1400	3.83	14.7	23.1	8.32	90-5-5 HC, PVDF, CB	1M $NaPF_6$ in EC:DMC, 1:1, 1.5 % FEC	37.2 mA g^{-1}	83	354	294	102
Shaddock peel	800-1400	3.92-3.76	25.5-39	-	6.32-2.47	80-10-10 HC, PVDF, CB	1M $NaClO_4$ in EC:DEC 1:1	30 mA g^{-1}	63-69	418-636	263-430	197
Soybean roots	600 - 800	3.95	7.5	-	10.08-14.83	70-10-20 HC, PVDF, CB	1M $NaClO_4$ PC, 5% FEC	500 mA g^{-1}	39-44	644-911	255-369	227
Spartina alterniflora	1000-1600	3.72-3.55	415.5 - 7.9	-	-	90-5-5 HC, CMC, CB	1M $NaClO_4$ in EC:PC, 1:1	20 mA g^{-1}	63-70	234-394	212-265	161
Sugarcane Bagasse	750 - 1050	3.74-3.81	8-2	-	15.9-13.4	70-10-20 HC, PVDF, CB	1M $NaClO_4$ in EC:DEC, 1:1	30 mA g^{-1}	56-71	382-469	256-290	254
Triticale	1400	3.73	50	199	-	80-10-10 HC, PVDF, CB	1M $NaPF_6$ in EC:DMC, 1:1, 1.5% FEC	37.2 mA g^{-1}	64	379	242	135
Various biomasses	1400	3.6-3.92	2-97	0.5-338	-	80-10-10 HC, PVDF, CB	1M NaPF6 EC:DMC 1:1, 1.5 % FEC	37 mA g^{-1}	48-88	297-381	170-315	135
Walnut shell	1300	3.7	6	12	3.4	80-10-10 HC, PVDF, CB	1M $NaPF_6$ in diglyme	25 mA g^{-1}	66	479	315	154
Waste apple	750 - 1050	3.91-3.82	-	-	16.4-14.6	70-10-20 HC, PVDF, CB	1M $NaClO_4$ in EC:DEC, 1:1	30 mA g^{-1}	56-71	382-469	256-290	254
Waste Silk	800 - 2800	-	6.3-0.4	-	11.5-0.7	100 HC	1M $NaPF_6$ in DEGDME	30 mA g^{-1}	63-93	118-334	103-309	78
Wheat Straw	1000 -1400	-	-	257-39	1.86	80-10-10 HC, PVDF, CB	1M $NaPF_6$ in EC:DMC, 1:1, 1.5% FEC	30 mA g^{-1}	65-82	244-393	190-315	190

Table 3: Literature review of hard carbon materials derived from biopolymers: precursors used and physico-chemical and electrochemical performances

Hard carbon synthesis		**Hard carbon properties**				**Hard carbon testing conditions**			**Hard carbon performance**			**Refs.**
Precursor	**TT (°C)**	**d_{002} (Å)**	**N_2 SSA ($m^2\ g^{-1}$)**	**CO_2 SSA ($m^2\ g^{-1}$)**	**O % (at. %)**	**Formulation**	**Electrolyte**	**Current density**	**iCE (%)**	**1st cycle insertion capacity ($mAh\ g^{-1}$)**	**1st cycle reversible capacity ($mAh\ g^{-1}$)**	
A-sugar	900-1600	-	67.6-0.7	-	-	-	-	-	-	-	-	171
Catechu tannin	1500	3.55	6.9	16.2	14.1 (wt%)	90-5-5 HC, PVDF, CB	1M $NaPF_6$ in EC:DMC, 1:1, 2%FEC	37.2 $mA\ g^{-1}$	84	351	300	189
Cellulose	900	3.88	819	-	-	80-10-10 HC, PAA, CB	1M $NaClO_4$ in EC:DEC, 1:1, 5% FEC	20 $mA\ g^{-1}$	41	839	343	46
Cellulose	1000-1600	3.89-3.72	83.0-8.0	406-3	9.2-7.8	80-10-10 HC, PVDF, CB	1M $NaPF_6$ in EC:DMC, 1:1	37.2 $mA\ g^{-1}$	48-84	342-379	254-310	40
Cellulose oak sawdust	900-1300	4.15-3.97	604.6-3.8	-	37.6-2.15	70-10-20 HC, PVDF, CB	1M $NaClO_4$ in EC:PC:DMC, 9:9:2	50 $mA\ g^{-1}$	46-68	275-450	140-305	255
Chestnut tannin	1500	3.57	2.2	15	7 (wt%)	90-5-5 HC, PVDF, CB	1M $NaPF_6$ in EC:DMC, 1:1, 2%FEC	37.2 $mA\ g^{-1}$	85	332	279	189
Chitin	1300-1500	3.61-3.57	110	72-222	2.8	80-10-10 HC, PVDF, CB	1M $NaPF_6$ in EC:DEC, 1:1	C/10	63	444	280	29
Chitosan	1300	3.65	2.6	24	14.9	80-10-10 HC, PVDF, CB	1M $NaPF_6$ in EC:DEC, 1:1	C/10	82	341	280	29
D-Glucose HTC	1000-1200	4.06-3.94	65.7-38.3	-	1.29-2.84	75-15-10 HC, PVDF, CB	1M $NaClO_4$ in EC:DMC, 1:1	100 $mA\ g^{-1}$	71-81	209-350	229-285	99
Filter paper	1000	3.86	539	-	-	95-5 HC, Na-alginate	1M $NaClO_4$ in EC:DMC, 1:1	30 $mA\ g^{-1}$	37	405	150	183
Glucose	600-1700	3.6-3.5	550-9	-	-	89-6-5 HC, PVDF, CB	1M $NaPF_6$ in EC:DEC, 1:2	10 $mA\ g^{-1}$	56-89	333-402	187-355	163
Glucose spheres (HTC)	1400	4.0	25	136.5	-	94-3-3 HC, PVDF, CB	1M $NaPF_6$ in EC:DMC, 1:1	7.44 $mA\ g^{-1}$	85	325	281	98

Lignin	1000-1500	3.83-3.65	124.9-14.7	-	1.71-0.94	70-20-10 HC, PVDF, CB	1M $NaClO_4$ EC:PC:DMC, 9:9 :2	50 mA g^{-1}	61-72	302-392	203-261	[85]
Lignin Kraft	1200	3.84	1.6	40	-	80-10-10 HC, CMC, CB	1M $NaClO_4$ in EC:DMC, 1:1	25 mA g^{-1}	66	273	181	[30]
Lignin Kraft low S	1200	3.82	180	378	-	80-10-10 HC, CMC, CB	1M NaClO4 in EC:DMC, 1:1	25 mA g^{-1}	64	319	205	[30]
Microcrystalline cellulose	1300	3.62-3.67	58.5-281.8	-	-	90-10 HC, PVDF	1M $NaClO_4$ EC:DMC :PC 9:2:9	50 mA g^{-1}	58-66	350-550	231-322	[256]
Milled-wood lignin	1000-1600	4.1-3.46	19.7-10.3	-	10.1-4.8	80-10-10 HC, PAE, CB	1M $NaPF_6$ in EC:DEC:DMC	20 mA g^{-1}	72.3-80.1	299-387	216-292	[83]
Mimosa tannin	1500	3.61	1.5	16.5	10 (wt%)	90-5-5 HC, PVDF, CB	1M $NaPF_6$ in EC:DMC, 1:1, 2%FEC	37.2 mA g^{-1}	86	345	295	[256]
Mimosa tannin extract	900-1600	3.9-3.4	287-7	-	4.46-0.58 (wt%)	92-2.9+2.5-2.6 HC, CMC, CB	1M $NaPF_6$ in EC:DMC, 1:1	18.6 mA g^{-1}	42-87	-	150-306	[172]
Myrobalan tannin	1500	3.64	2.2	14.2	7.2	90-5-5 HC, PVDF, CB	1M $NaPF_6$ in EC:DMC, 1:1, 2%FEC	37.2 mA g^{-1}	85	359	304	[256]
Sucrose	700-1600	3.46-3.62	13.6-26.5	-	-	80-10-10 HC, PVDF, CB	1M $NaPF_6$ in EC:DEC, 1:1	20 mA g^{-1}	49-67	184-370	91-231	[162]
Starch	900-1700	3.75-3.51	6.3-1.5	-	2.47-0.43	92-2.5-2.5-3 HC, CMC, SBR, CB	0.6M $NaPF_6$ in EC:EMC, 1:1	30 mA g^{-1}	80-93.9	250-376	235-320	[198]
Starch potato	1500	3.77	2.4	2.3	10	90-5-5 HC, PVDF, CB	1M $NaPF_6$ in EC:DMC, 1:1, 2% FEC	37.2 mA g^{-1}	88.6	329	291	[174]
Starch rice	1500	3.79	14.7	35.8	2.2	90-5-5 HC, PVDF, CB	1M $NaPF_6$ in EC:DMC, 1:1, 2% FEC	37.2 mA g^{-1}	85.8	359	308	[174]
Sucrose octaacetate	1300	3.95	98.9	-	2.21	70-10-20 HC, PVDF, CB	1M NaClO4 in EC:PC:DMC, 9:9:2	50 mA g^{-1}	56	426	242	[255]
Sucrose-HTC	1000-1900	3.88-3.54	297.7-0.8	-	4.8-2.3	90-10 HC, CMC	1M $NaPF_6$ in EC:DEC, 1:1	20 mA g^{-1}	n.a-95.2	180-348	n.a.-331	[41]

Table 4: Literature review of hard carbon materials derived from synthetic polymers: precursors used and physico-chemical and electrochemical performances

Hard carbon synthesis		**Hard carbon properties**				**Hard carbon testing conditions**			**Hard carbon performance**			**Refs.**
Precursor	**TT (°C)**	**d_{002} (Å)**	**N_2 SSA ($m^2\ g^{-1}$)**	**CO_2 SSA ($m^2\ g^{-1}$)**	**O % (at. %)**	**Formulation**	**Electrolyte**	**Current density**	**iCE (%)**	**1st cycle insertion capacity (mAh g^{-1})**	**1st cycle reversible capacity (mAh g^{-1})**	
Bituminous	1300	-	13.93	-	-	80-10-10 HC, PAA, CB	1M $NaClO_4$ in EC:DEC, 1:1	20 mA g^{-1}	68	329	224	[77]
Disposable masks	1600- 2400	3.6-3.42	27.4 – 13.4	-	2.7 -1.0	90-10 HC, PVDF	1M $NaPF_6$ in DEGDME	25 mA g^{-1}	68-86	282-443	209-328	[257]
Leonardite humic acid	900-1600	3.99-3.62	6.4-1.1	-	6.9-2.6	80-10-10 HC, PVDF, CB	1M $NaClO_4$ in EC:DMC, 1:1	25 mA g^{-1}	58-75	418-500	286-345	[199]
Mesophase Pitch	1000	3.49	2	-	-	95-5 HC, Na-alginate	1M $NaClO_4$ in EC:DMC, 1:1	30 mA g^{-1}	80	221	177	[183]
PEDOT	700	3.86	39.8	-	3.5	85-10-5 HC, PVDF, CB	1M $NaClO_4$ in EC:PC, 3:1	100 mA g^{-1}	54-74	579-657	315-486	[258]
PET	1200-1600	3.81-3.63	~ 1 – 2.6		16.16 - 7.3	80-10-10 HC, Na-alginate, CB	1M $NaPF_6$ in EC:DMC, 1:1	20 mA g^{-1}	80-86	380-398	308-342	[169]
Phenolic resin	1100	3.85- 3.89	35-338	-	-	85-2+3-10 HC, CMC/sbr, CB	1M $NaClO_4$ in EC:DEC, 1:1	20 mA g^{-1}	62-85	389-401	243-334	[114]
Phenolic resin	600-1600	3.88-3.72	140-72	394-139	-	85-8-7 HC, PVDF, CB	1M $NaClO_4$ EC:PC:DMC, 0.45 :0.45:0.1	C/10	33-57	245-453	122-254	[185]
Phenolic resin + dopant	700	4.02- 4.23	356-982	-	3.99 -9.01	80-10-10 HC, CMC, CB	1M $NaPF_6$ in DME	200 mA g^{-1}	89	571	506	[112]
Phenolic resin + GO	1400	3.7-3.9	1.8-5.6	-	-	95-5 HC, Na-alginate	1M $NaPF_6$ in EC:DMC, 1:1	30 mA g^{-1}	80-90	362-383	290-343	[259]
Phenolic resin spheres	1300 - 1600	3.9- 3.77	2.7-6	60 - 9	3.1	94-3-3 HC, PVDF, CB	1M $NaPF_6$ in EC:DMC, 1:1	7.44 mA g^{-1}	89-92	318-345	293-309	[98]
Phenolic resin spheres (TCA)	1300-1400	4-3.8	104 -23	425-343	-	94-3-3 HC, PVDF, CB	1M $NaPF_6$ in EC:DMC, 1:1	7.44 mA g^{-1}	68-70	349-423	239-296	[98]
Phloroglucinol	1100-1700	3.96-3.70	36-3.7	273.3-20.8	-	70-10-20 HC, PVDF, CB	1M $NaPF_6$ in EC:DMC, 1:1	37.2 mA g^{-1}	76	350	270	[32]

Pitch	1400	3.45	2.85	-	-	95-5 HC, Na-alginate	1M NaPF$_6$ in EC:DMC, 1:1	30 mA g^{-1}	58-82	157-332	85-254	119
Polyacrylonitrile	950-2800	3.49-3.43	24-20	67-20	-	100 HC	1M NaClO$_4$ in EC:DMC, 1:1	50 mA g^{-1}	46-73	125-370	77.5-237	75
Polyacrylonitrile + S	800-1200	3.53-3.66	-	-	-	80-10-10 HC, PVDF, CB	1M NaClO$_4$ in EC:DEC, 1:1, 2% FEC	500 mA g^{-1}	31-63	300-613	92-284	165
Polyamic acid nanofibers	800	3.71	273	-	-	80-10-10 HC, CMC, CB	1M NaCF$_3$SO$_3$ in Diglyme	50 mA g^{-1}	70	447	313	260
Polyaniline	700	3.76	4.18	-	9.2	80-10-10 HC, PVDF, CB	1M NaClO$_4$ in EC:DEC, 1:2	30 mA g^{-1}	50	432	215	117
Polyaniline nanowire	1150	3.7	34.1	-	-	80-10-10 HC, PVDF, CB	1M NaClO$_4$ in EC:EMC, 1:1	50 mA g^{-1}	45	500	224	116
Polycarbonate	1200 - 1600	3.77- 3.72	~ 2	-	7.75- 6.52	80-10-10 HC, Na-alginate, CB	1M NaPF$_6$ in EC:DMC, 1:1	20 mA g^{-1}	80-85	333-380	282-327	169
Polypyrrole	700	3.53	139.7	-	17.64	85-10-5 HC, PVDF, CB	1M NaClO$_4$ in EC:PC, 3:1	100 mA g^{-1}	54	579	315	258
Polyurethane foam	500-900	3.68-3.55	183.4-87.5	-	-	80-10-10 HC, PVDF, CB	1M NaClO$_4$ in EC:DMC, 1:1	20 mA g^{-1}	38.3	600	230	261
PVC	1000-1700	3.42-3.43	7	-	-	89-6-5 HC, PVDF, CB	1M NaPF$_6$ in EC:DEC, 1:2	10 mA g^{-1}	48-68	137-361	73-226	163
PVC nanofibers	600-800	3.52-3.50	-	-	-	80-10-10 HC, PVDF, CB	1M NaPF$_6$ in EC:DEC, 1:1	12 mA g^{-1}	65-70	331-389	214-272	74
PVDF	400-800	-	1024-878	-	-	70-10-20 HC, PVDF, CB	1M NaClO$_4$ in PC	50 mA g^{-1}	34-39	410-690	140-270	262
Resorcinol	800-3000	4.17-3.42	4.2 - 650	-	-	100 HC	0.8M NaClO$_4$ in EC:DEC, 1:1	20 mA g^{-1}	31-92	260-390	110-350	38
Sodium Polyacrylate	1100	3.79	108.9		-	80-10-10 HC, PVDF, CB	1M NaClO$_4$ in PC	50 mA g^{-1}	80	426	341	263
Subbituminous	1000-1500	-	35.3-3.1	-	-	80-10-10 HC, PAA, CB	1M NaClO$_4$ in EC:DEC, 1:1	20 mA g^{-1}	68-79	329-380	224-289	77
Tire rubber	1100-1600	2.67-1.58	189-148	-	14.8-3.6	80-10-10 HC, PVDF, CB	1M NaClO$_4$ in EC:DEC, 1:1	20 mA g^{-1}	48-66	308-520	185-250	184
Commercial Hard carbon materials												
BSHC-300, BTR	-	-	≤ 5.0	-	-	-	-	-	≥88	-	295 ± 5.0	264

C1600 Sumitomo Chemical Co.	1600	-	10	-	-	95-5 HC, PVDF	1M $NaClO_4$ in EC:DMC, 1:1	20 mA g^{-1}	78	413	321	265
Carbotron P, Kureha Co.	-	3.67	4-8	-	-	96-4 HC, polyamide-imid	Na[FSA] : [C3C1pyrr]FSA, 20 :80	50 mA g^{-1}	82.7	259	214	266,267
Carbotron P, Sumitomo Bakelite Co.	-	3.64	-	-	-	96-4 HC, polyamide-imid	Na[FSA] : [C3C1pyrr]FSA, 20 :80	50 mA g^{-1}	86.7	295	255.7	266
JFE, JFE Chemical corporation	-	-	0.7-5	-	-	-	-	-	-	350-410	-	268
Kuranode, Kuraray	-	> 3.8	5.2	-	-	97-1.5-1.5 HC, CMC, SBR	1M $NaPF_6$ in EC:DMC, 1:1	C/10	92	300	276	269,270
PAC2 Aekyung Petrochemical	-	3.75	3.8	3.6	-	94-3-3 HC, PVDF, CB	1M $NaPF_6$ in EC:DMC, 1:1	C/50	86	322	277	98
YHC-1, BSG –Best Graphite	-	-	5.27	-	-	-	-	-	89.2	-	294.6	271

4 Relationship Between Hard Carbon Properties and Electrochemical Performance

The electrochemical performance of hard carbon-based electrodes is closely dependent on the structural, chemical, textural, and morphological features of the active material. Thus, by altering the properties of the HC, it is possible to significantly enhance reaction kinetics, ion transport, Coulombic efficiency, and the battery's cycle life. However, in addition to HC features, testing conditions (e.g., electrode formulation, presence of additives, electrolyte formulation, current rate, etc.) can also significantly influence the performance of the material. To our knowledge, for the evaluation of the electrochemical performance of battery materials at the laboratory scale, no international standardisation exists, contrary to other characterisation techniques. Therefore, it is very difficult to compare the results of one study with another. Nevertheless, some rough tendencies between the properties of a wide range of HCs available in the literature and the electrochemical performance delivered by those materials were observed and are discussed in the following sections. The presented correlations are based on existing knowledge on the electrochemical performance (e.g. iCE and reversible capacity) and the physical-chemical characteristics that have a major influence on these electrochemical parameters.

4.1. N_2 SSA influence on iCE

Figure 21 presents the influence of N_2 SSA on the initial Coulombic Efficiency (iCE), for a wide range of hard carbon materials reported in the literature. The HCs were grouped on the basis of the precursor origin, namely, biomasses, biopolymers, and synthetic polymers, as in the previous sections. In general, it can be observed that regardless of the precursor, lower N_2 SSA values are more favorable to obtain a higher iCE %. However, this tendency is less visible in the case of biomass-derived HCs. Figure 21.a presents the results for biomass-derived HC materials. To some extent, the tendency of iCE to increase with the decrease in N_2 SSA is observed, especially within the same series of precursors, for example, date palm pulp, mangosteen shell, sugarcane bagasse, etc. However, for low N_2 SSA values (< 20 m^2 g^{-1}), very different iCE values are observed for HC materials prepared with different precursors. i.e., ~ 40% (for grapefruit peels and ginko leaves) *vs.* ~ 80% (for beechwood HC and ~ 85% for mangosteen shells). This might be due to the fact that for some materials the available surface area cannot be fully assessed by N_2 gas, therefore, the material surface is underestimated [176].

Another reason can be that other parameters may affect iCE. In this direction, biomass-derived HCs are known to have very rich surface chemistry (heteroelements) and chemical composition (inorganic minerals), a feature that has been shown to have a significant influence on the iCE, along with porosity [98, 135]. Moreover, the active surface area of the materials also has a major impact on the iCE delivered by the materials, as shown elsewhere [180].

In the case of biopolymers and synthetic polymers, Figure 21.b and Figure 21.c, the relationship between iCE and N_2 SSA is more obvious. A significant decrease in the iCE is observed for the HCs having high N_2 SSA. For example, Zhong et al.[272] reported an iCE value of only 23% for a glucose-derived HC having an N_2 SSA of 475.9 $m^2\ g^{-1}$. On the contrary, a high iCE of approximately 85% was reported for materials with low N_2 SSA (below 10 $m^2\ g^{-1}$), i.e., mimosa and myrobalan tannin HCs [189], cellulose-derived HC [83], glucose-based HC [228]. The high iCE of some biopolymer HCs can be explained by the chemical composition of precursors which contain fewer impurities than biomass ones, and therefore the surface chemistry of HCs affects less the iCE. Furthermore, for synthetic polymers that are rather pure precursors (no inorganics) and have low oxygen content, the correlation between iCE and N_2 SSA is less impacted by other physicochemical parameters. This might also explain why the best correlation between iCE and N_2 SSA was obtained for this category of precursors (Figure 21.c).

However, if one considers a particular precursor, it is rather difficult to find a linear correlation between iCE and SSA, since there are so many other parameters that impact the iCE, e.g., d-spacing, ultramicroporosity (which is not accessible by N_2), surface chemistry, testing conditions, etc. For example, Li. *et al*. developed hard carbons with different N_2 SSAs, from pitch and lignin [119]. The authors reported an iCE of 82% for an HC with an N_2 SSA of 4.3 $m^2\ g^{-1}$ and only 75% iCE for an HC with a very similar N_2 SSA (4.5 $m^2\ g^{-1}$). Furthermore, a similar iCE value (74%) was found for an HC with a significantly higher N_2 SSA than the previous HCs, 34.7 $m^2\ g^{-1}$. Therefore, the linear trend between iCE and N_2 SSA is not present in several cases due to other factors. For example, the authors mentioned the high degree of crystallinity, which might lead to Na^+ trapping between the graphene layers with narrow interlayer distances. Another reason may be the fact that the overall porosity cannot be accessed by N_2 adsorption, as explained in Section 3.3. No correlation was observed between iCE and N_2 SSA, however, when using O_2 gas, an increase in iCE was noticed with the decrease in O_2 SSA [176]. In fact, later on, the same authors showed a linear relationship between iCE and O_2 SSA by using several types of carbons [180]. They pointed out as well, that narrow pores (ultra-micropores) are the most responsible for the decrease in iCE. For the commercial HCs reported in the literature which present low SSAs, a high iCE is reported in general, superior to 80%. Nevertheless, an iCE as high as 92% was reported for a Kuranode HC [269,270].

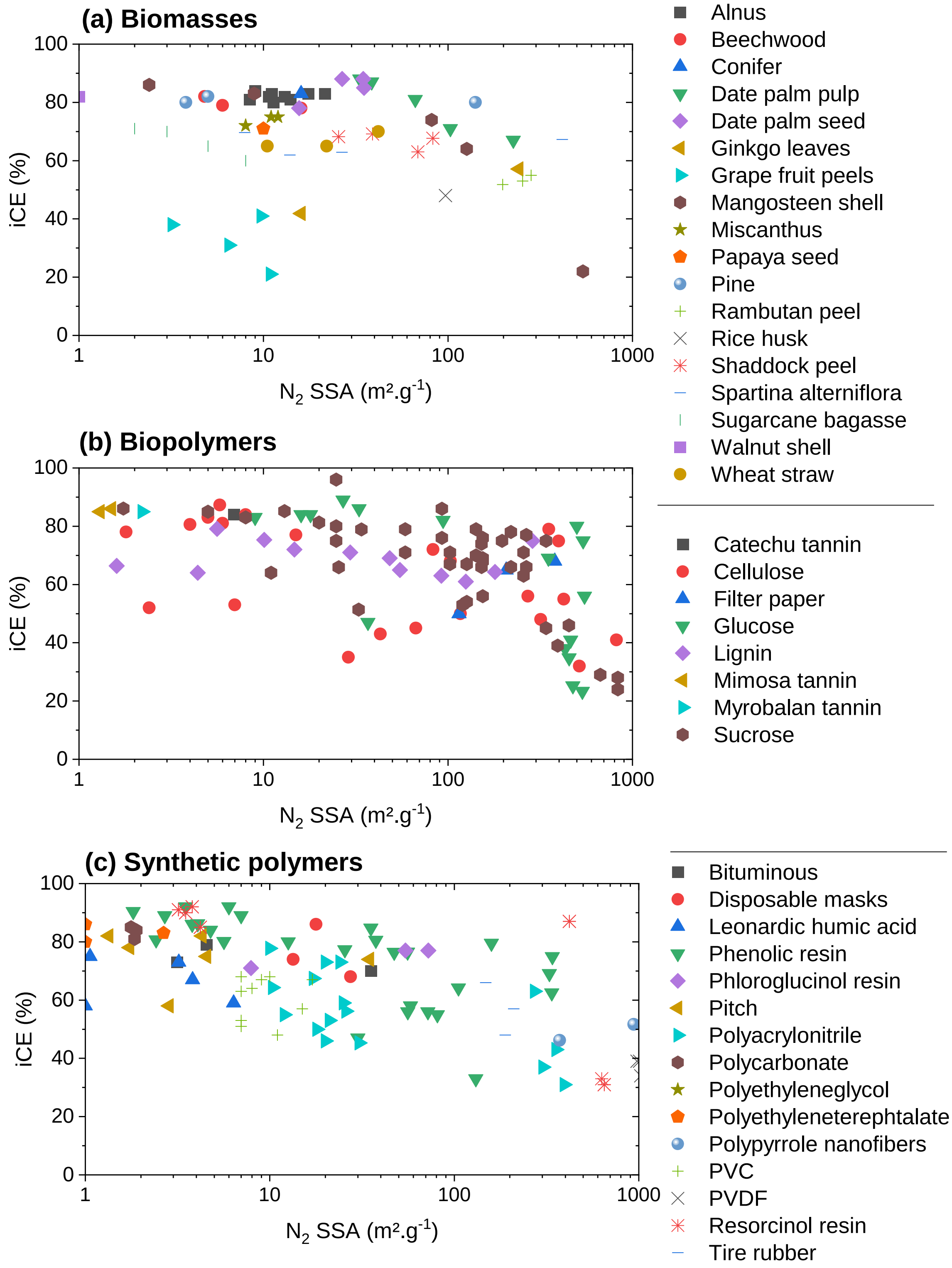

Figure 21: Initial Coulombic Efficiency as a function of the N_2 SSA for the 3 types of precursors: a) Biomass, b) Biopolymers and c) Synthetic polymers. The graphs were built based on the references presented in Tables 2 to 4.

4.2. Active surface area influence on iCE

The active surface area has been reported to be involved in irreversible electrochemical reactions and therefore has a significant impact on the iCE. Figure 22.a resumes the correlation between iCE and ASA obtained based on all articles in the literature reporting both these parameters, no matter the category of precursor. Generally, it can be seen in Figure 22.a that higher ASA values are unfavourable for iCE, in a similar way as for N_2 SSA. Furthermore, the same tendency is observed for each individual category of precursors (biomass, biopolymers, or synthetic polymers).

Only PAN-derived HC deviates from this trend, and this is only when the ASA values are very low, namely below 1 m^2 g^{-1}, and correspond to very high annealing temperatures, 2200-2800 °C. This can be explained by the structural characteristics of these materials, which exhibit very small interlayer distances, for example, 0.343 nm at 2800 °C, values very close to those of graphite (0.335 nm) [75]. The authors reported that such low values of d_{002} significantly reduce the plateau capacity gain and favor Na^+ trapping between the graphene layers, thus inducing a low iCE.

When the materials are heat-treated at lower temperatures, i.e., 1200 – 1500 °C, and the physicochemical parameters are not drastically impacted, the correlation between iCE and ASA is maintained. Ghimbeu's group, which is among the few to analyze the ASA parameter on HCs, recently highlighted its importance on iCE (Figure 22.b). The authors could evidence by employing different precursors (i.e., biopolymers or synthetic polymers) or annealing temperatures (1300 – 1600 °C), that the irreversible capacity is reduced, therefore, the iCE is improved, when ASA values are diminished [180].

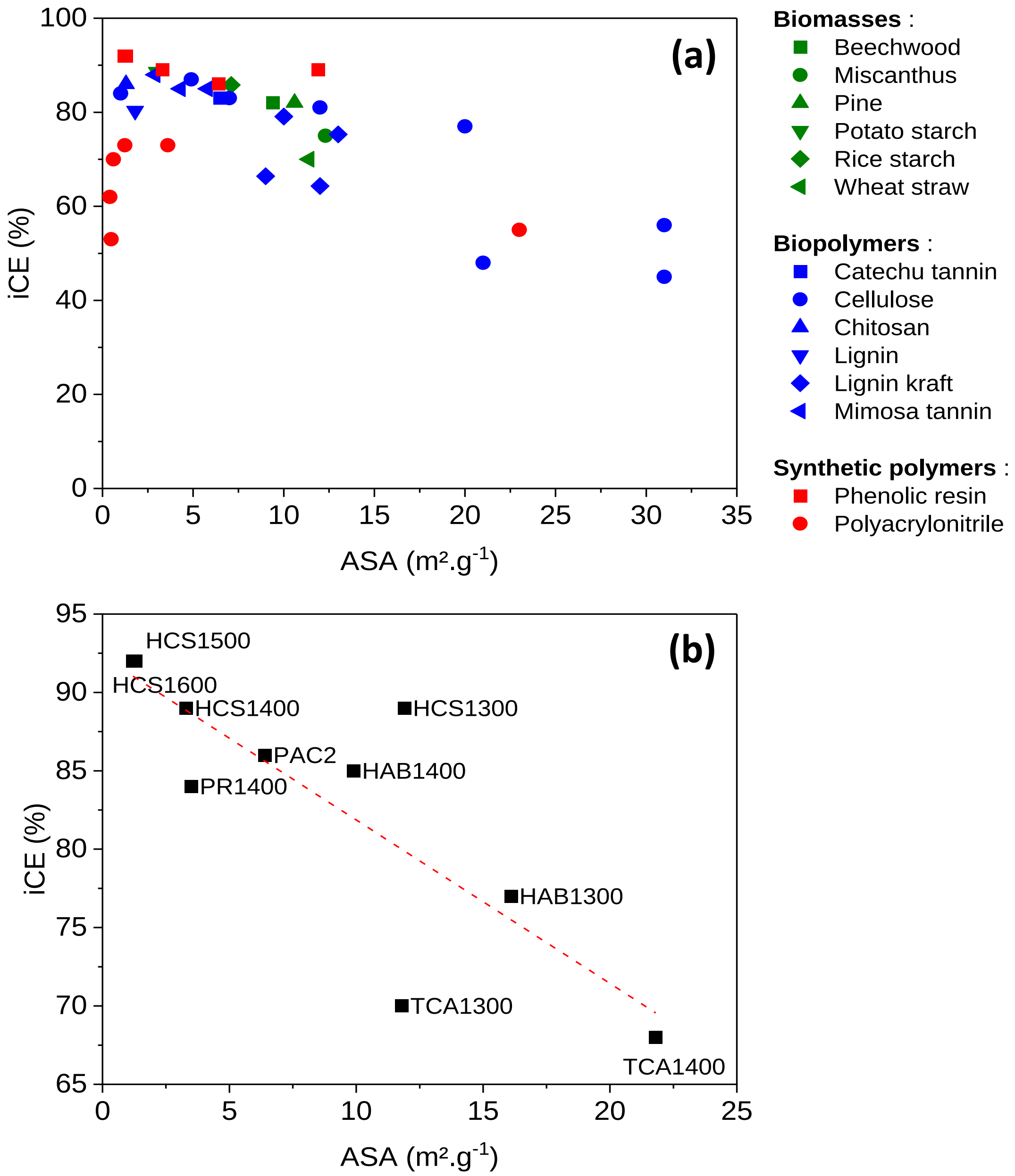

Figure 22: (a) iCE as a function of ASA for the three classes of precursors. The graphs were built based on the references presented in Tables 2 to 4. (b) Relationship between iCE and ASA. Adapted under the terms of CC BY-NC 3.0 DEED licence [180]*, Copyright 2022, The Authors, Published by Royal Society of Chemistry.*

4.3. Ash content influence on electrochemical performance

Another parameter that was observed to have an impact on the iCE is the ash content of the materials. This parameter is particularly evaluated for biomass-derived HCs, with Figure 23 summarizing the articles that report this feature. Although the number of papers reporting it is limited, a nice linear trend with iCE can be observed (Figure 23.a). Regardless of the precursor, higher wmf % negatively impacts iCE. This can be explained by the involvement of 'ash' in different undesirable reactions. On the one hand, inorganics can affect the properties of materials during synthesis, e.g., an increase of SSA (for Na, K, Ca-based), local graphitization (for K, Ca, Fe and Si-based), growth of nanostructures (Si-based), a decrease of electronic conductivity (all impurities) [30, 135, 137] which favor the electrolyte decomposition, Na-ion trapping, etc. On the other hand, the inorganic impurities can also interact with the electrolyte leading to its decomposition and, in some cases, to their dissolution. It is worth mentioning that the better trend observed in this case might be related, to a certain extent, to the similar electrochemical conditions used for all the materials (e.g., electrode and electrolyte formulation, current density, and cycling regime), since all materials are reported by the same research group[135].

Not only is iCE impacted by the ash content, but so is the reversible capacity delivered by the materials. Figure 23.b shows that when the percentage of "ash" increases, the obtained reversible capacity decreases significantly. Rios et al.[135] illustrated very well this trend by using a wide number and types of precursors. The authors reported a reversible capacity of ~ 300 mAh g^{-1} for a sunflower seed HC with an ash content of 3.2 wmf %, 256 mAh g^{-1} for a papaya seed HC with an ash content of 6.7 wmf % and only ~ 170 mAh g^{-1} for a rice husk HC with an ash content as high as 14.7 wmf %. The latter behavior is explained by a reduced carbon content in the materials when the ash wmf % is high, and by the nature of impurities (Si and Ca-based) which graphitized the carbon and lead to the growth of SiC whiskers and the decrease in the graphitic interlayer space. This induce a limited capacity delivered by the material.

From a more general point of view, the authors concluded that the HC derived from woody and agriculture biomass precursors presents a low content of inorganic ash in their precursor (0.8 wmf % for Beechwood to 6.7 wmf % for Papaya seeds) and very good performance (iCE ~ 85% and capacity of ~ 300 mAh g^{-1} for Beechwood). On the contrary, the HC obtained with grassy biomass presents a higher amount of ash (2.8 wmf % for Miscanthus to 14.6 wmf % for rice husk) and lower performance. Although among the three classes of biomass, the ash composition is similar (i.e., Na, K, Ca, Mg, Si, and Fe), but their total amounts and proportions are significantly different. HCs with lower impurity concentrations, and therefore higher carbon contents, limit irreversible reactions with the electrolyte and promote electrode conductivity, improving electrochemical performance (i.e., reversible capacity ~ 300 mAh g^{-1} and iCE ~ 85%). The HCs rich in Si and Ca lead to worse performance.

Because the ash content proves to have an important influence on the electrochemical performance of HC materials, its determination should be considered mandatory for all hard carbon materials. Currently, this is determined on limited HC materials, mainly biomass-based ones, although biopolymers and synthetic polymers might contain also [30]. Commercial HC technical sheets do not provide such information either, despite its high interest [267, 268, 270].

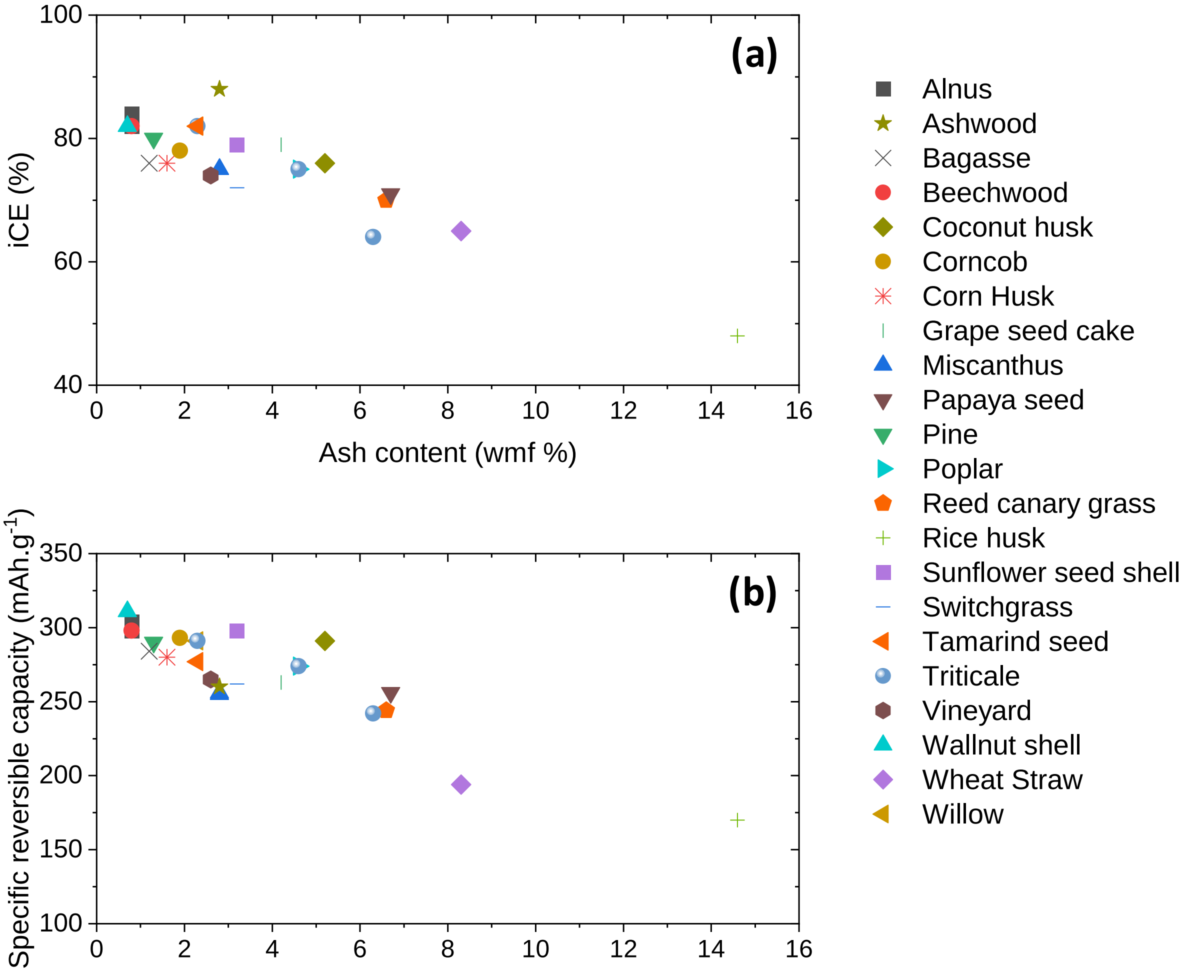

Figure 23: (a) iCE and (b) specific reversible capacity as a function of the ash content for the biomass precursors. The graphs were built based on the reference [135].

4.4. Interlayer space influence on the specific reversible capacity

The distance between layers (d_{002}) is an important characteristic of HC, directly involved in the storage mechanism of Na^+ and is often linked to the capacity delivered by the materials. Figure 24 summarizes the influence of the value of d_{002} on the reversible capacity, among the three categories of precursors: biomass, biopolymers, and synthetic polymers. First, it can be noticed that there is a wide range of d_{002} values reported in the literature, i.e., 3.4 Å - 4.2 Å, corresponding to reversible capacities comprised between a few mAh g^{-1} (14 mAh g^{-1} for a grapefruit peel HC) [203] and 430 mAh g^{-1} (shaddock peel HC) [197]. Second, no general trend can be observed, but some particularities are present for each category of precursors.

In the case of biomass-derived HC (Figure 24.a), most of the interlayer distance values are between 3.7 Å and 3.9 Å while the reversible capacity delivered is mainly between 250 and 300 mAh g^{-1}. For HCs derived from biopolymers presented in Figure 24.b, the points are very randomly located, especially for materials with a d_{002} value superior to 3.9 Å, for which the reversible capacity varies between 75 and 361 mAh g^{-1}.

For HC derived from synthetic polymers, although the points presented in Figure 24.c are highly dispersed, a bell curve trend can be depicted. The highest reversible capacities are obtained for materials with a d-spacing between 3.7 Å and 3.9 Å, while outside these limits, materials tend to deliver lower reversible capacities. This can be due to either the steric effects ($d_{002} < 3.7$ Å) or the low conductivity ($d_{002} > 3.9$ Å).

This difficulty in establishing correlations between d_{002} and the reversible capacity can be related to a certain extent to the fact that the Na^+ storage mechanism relies on several phenomena including adsorption into the porosity, interactions with the surface chemistry (e.g., functional groups, active surface area) and intercalation between the graphene sheets. Each particular phenomenon can be attributed to a certain region of the galvanostatic curve, as will be detailed in the next chapter.

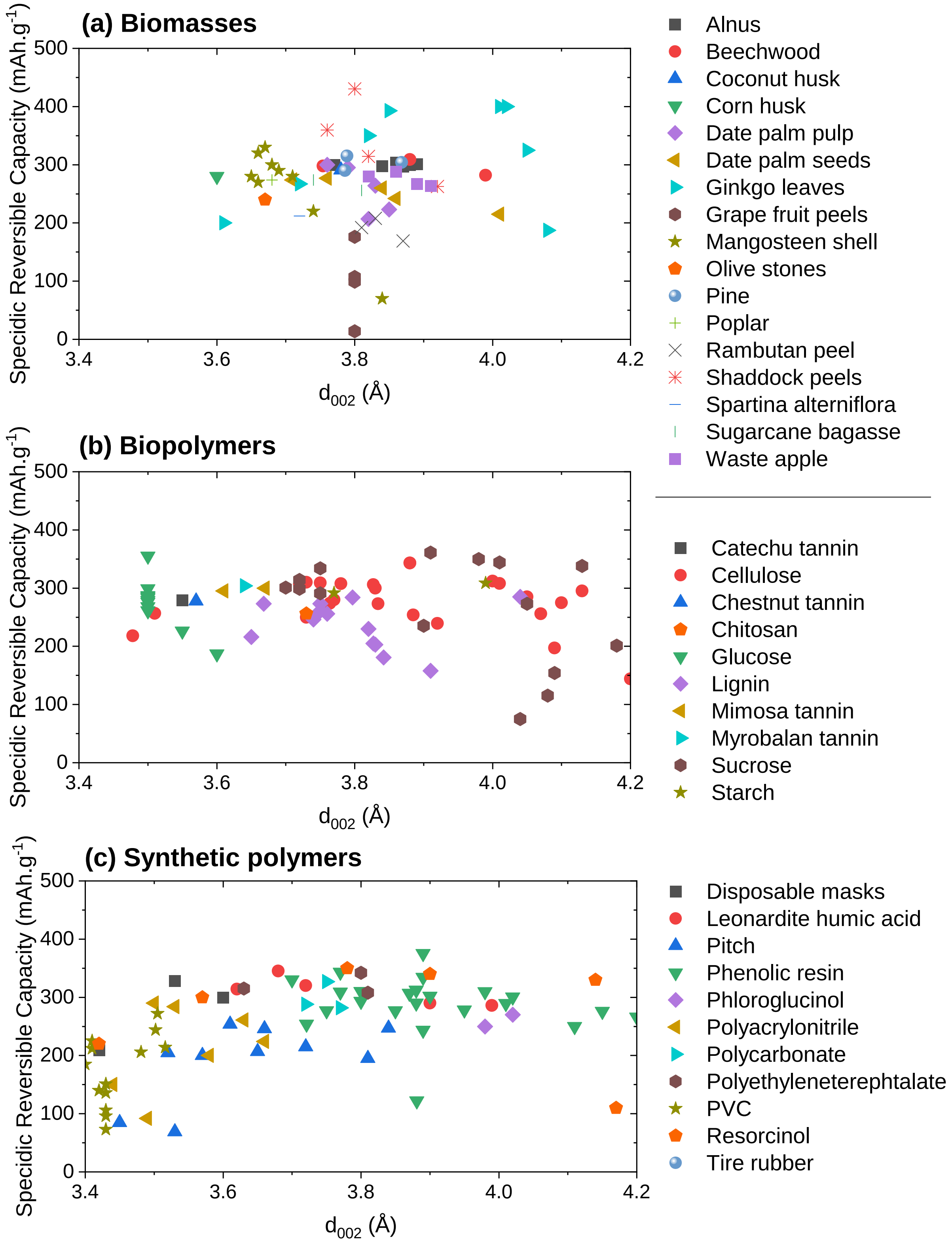

Figure 24: Specific reversible capacities as a function of the d_{002} interlayer spacing for the 3 types of precursors: a) Biomasses, b) Biopolymers, c) Synthetic polymers. The graphs were built based on the references presented in Tables 2 to 4.

4.5. N_2 specific surface area influence on the specific reversible capacity

In addition to the distance between graphene layers, HC porosity is involved in Na^+ storage mechanisms and several authors reported that it correlates with the specific capacity delivered by certain HC anodes. For example, Bommier et al. [28] used sucrose to prepare hard carbons with a wide range of N_2 SSAs, implying two strategies: different pyrolysis temperatures and CO_2 activation at various temperatures and time durations. N_2 adsorption revealed SSA values between 25 and 1410 $m^2\ g^{-1}$. When the reversible capacity was correlated with the surface area (Figure 25.a), a linear trend ($R^2 = 0.84$) showing that a lower SSA leads to an important increase in the reversible capacity delivered by the materials was found. In the same study, the authors revealed an interesting correlation between the reversible capacity and the so called unexposed carbon atoms (not involved in the surface area) [28]. It was shown that the HC materials exhibit the best performance when the highest percentages of unexposed carbon atoms are present, for example, 335 mAh g^{-1} for 98.4% unexposed carbon atoms (Figure 25.b). The authors attributed these observations to the fact that exposed carbons may act as nucleation sites favoring SEI, a passivation layer that limits the access of Na^+ to the carbon structure.

Despite these findings, when we tried to represent the reversible capacity as a function of N_2 SSA, for the three categories of precursors, biomass, biopolymers and synthetic polymers, a trend could hardly be observed, the points being very scattered. Rather a random trend was noticed among the commercial HCs, as well (Table 4). Despite their low N_2 SSA (< 10 $m^2\ g^{-1}$), the reversible capacity reported vary between 214 and 295 mAh g^{-1}.

Only in the case of biopolymer-derived HC some tendency could be observed, as presented in Figure 25.c. To some extent, it can be seen that the reversible capacity increases when the N_2 SSA is lower, as previously reported by Bommier et al. [28]. The trend is particularly observed when the sucrose precursor is used to prepare the HCs, while for the other precursors the distribution is rather random. This might be due to the fact that for certain precursors that undergo specific heat treatments, other HC parameters play an important role on the capacity delivered by the materials. For example, Beda et al. [98] reported that N_2 SSA provides a very poor correlation ($R^2 = 0.3$) with the capacity delivered by several HCs prepared from phenolic resins, heat-treated at different temperatures. Other parameters such as electrode porosity, d_{002} distance, or CO_2 SSA were found to affect the material's capacity more.

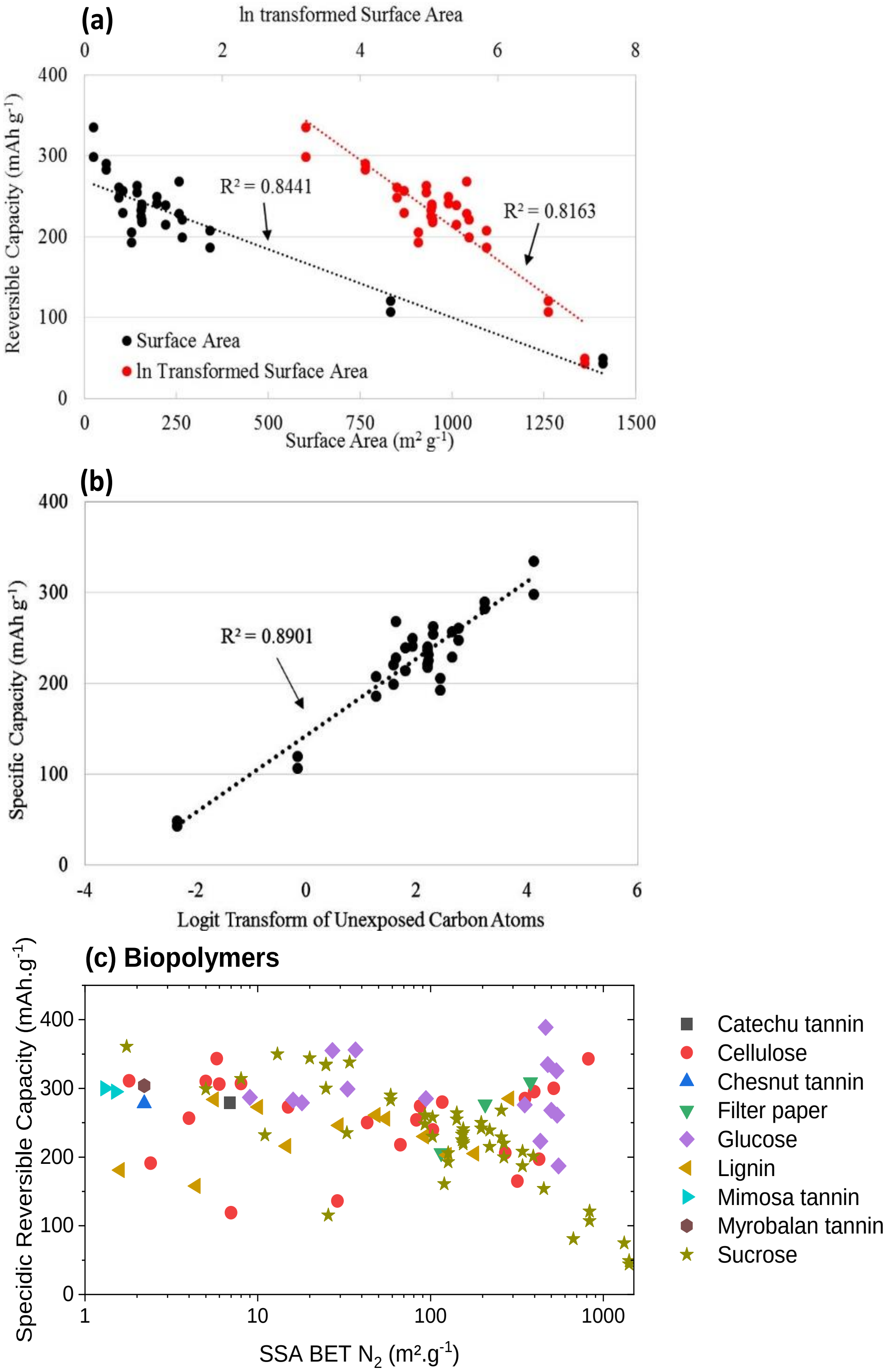

Figure 25: (a) Linear and natural logarithm transformed models plotting the reversible capacity as a function of N_2 SSA, (b) Reversible capacity vs. logit transform of the percentage of the unexposed carbon atoms. Reprinted with the permission from [28], Copyright 2014, Elsevier (c) Reversible capacity vs. N_2 SSA for biopolymers-based HCs using references presented in Table 3.

In a different paper, Gomez-Martin and co-authors [45] showed that the interlayer distance correlates well with the reversible capacity, in particular with the flat plateau region, while Meng et al. [193] improved the HC reversible capacity through closed porosity tuning. In particular, it was found that the capacity of the plateau region is increasing with the percentage of closed porosity. Therefore, it has been reported to be more appropriate to correlate HC properties with either the slope or the plateau capacity, instead of the reversible capacity delivered by HC materials.

4.6.Different hard carbon properties influence on plateau/slope capacity

Several authors have studied the impact of different hard carbon properties (e.g., d_{002}, I_D/I_G, closed porosity, etc.) on both the slope and flat plateau capacity regions. Figure 26 gathers the most important findings reported in the literature in this direction. Gomez-Martin et al. [45] reported a direct correlation between d-spacing and plateau capacity when using HC derived from olive stones, heat-treated between 800 and 2000 ° C [45]. One can see in Figure 26.a that the plateau capacity increases with the d_{002} value, the best performance being obtained for the material pyrolyzed at 1400 °C. When the temperature increases further to 2000 °C, the capacity decreases progressively, due to the decrease in d_{002}. Therefore, a temperature between 1400-1600 °C seems ideal to achieve the highest capacity. Escamilla-Pérez et al. [174] reported a similar trend ($R^2 = 90$), only that in this case the authors could show the importance of precursor origin instead of the annealing temperature (Figure 26.b). It was found that for a series of HCs derived from biopolymers, heat-treated at the same temperature (i.e., 1500 °C), the capacity gained in the plateau region is more important when the d-spacing is enlarged.

Also important, the same study revealed that the closed porosity of the material can impact the capacity of the plateau. Figure 26.c shows that the limited presence of closed porosity is beneficial to the gain of capacity in the low voltage plateau region ($R^2 = 0.88$). Other authors found an opposite trend, that is, an increase in plateau capacity with closed pores [273]. The reason for the discrepancy be related to the properties of the materials synthesised under very different conditions (precursors and temperature) and the indirect quantification of closed porosity via He density/gas adsorption and SAXS, which both present their own limitations. From a more general point of view, there is still no consensus on the closed-pore contribution to the plateau region, as will be detailed later in the mechanism part.

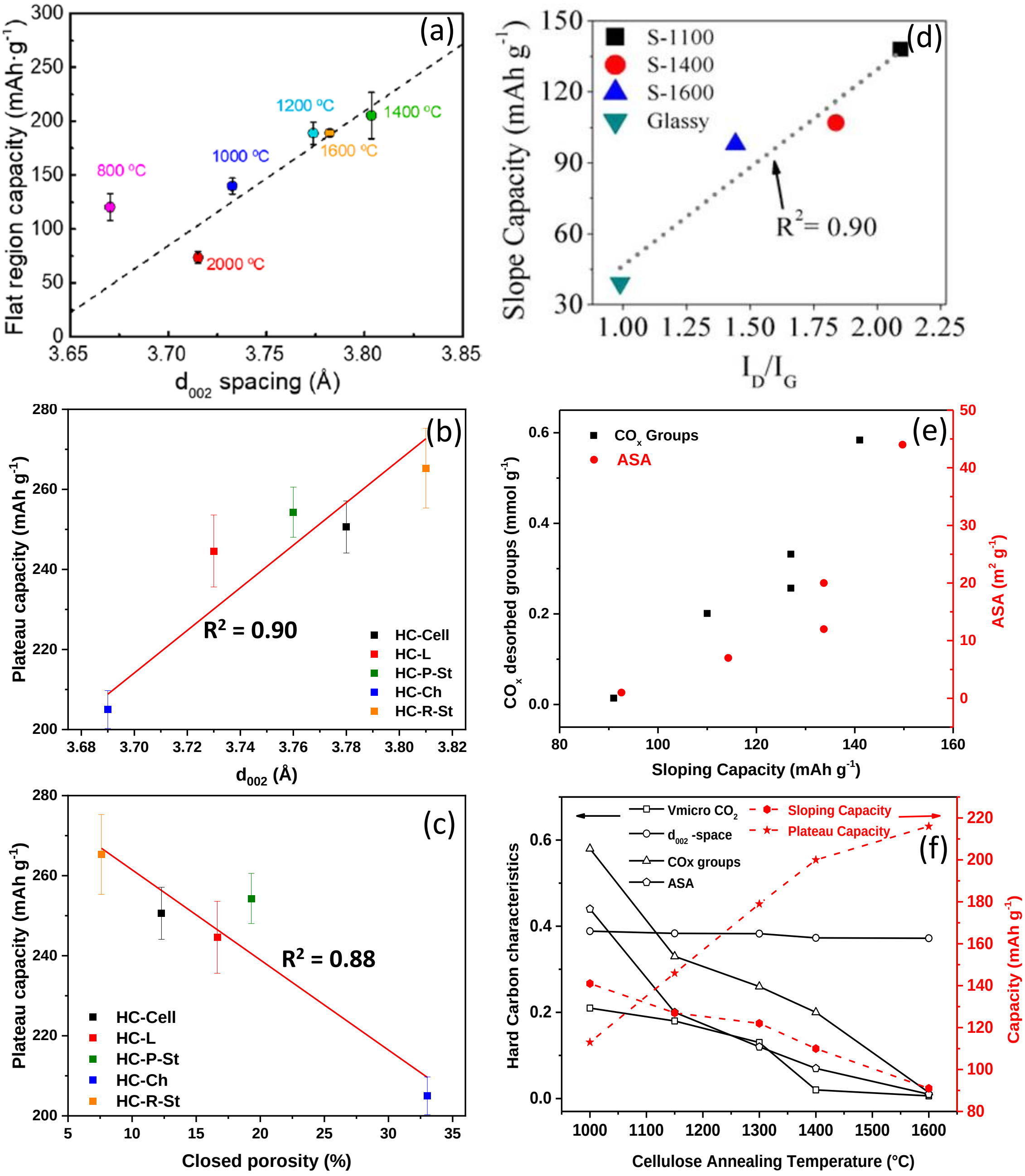

Figure 26: (a) Correlation between the plateau capacity and the graphitic interlayer spacing (d_{002}). Reprinted with permission from [45], Copyright 2019, American Chemical Society. Relationship between the plateau capacity of different HCs and (b) d_{002} and (c) closed porosity. Reprinted with permission from [174], Copyright 2023, American Chemical Society. (d) Plot of the sloping capacity vs. the I_D/I_G ratio. Reprinted with permission from [43], Copyright 2015, American Chemical Society. (e) Correlations between sloping capacity and the total amounts of CO_x groups (desorbed during TPD measurements) and ASA and (f) Evolution of different hard carbons characteristics vs. sloping and plateau capacities and the annealing temperature of a cellulose-derived HC. Reprinted with the permission from [40],Copyright 2018, Elsevier.

In which concerns the slope capacity, a relationship was found *vs*. the degree of the disorder (I_D/I_G ratio), as reported by Bommier et al. [43]. A linear trend can be seen in Figure 26.d (R^2 = 0.9) showing that the slope capacity increases with increasing I_D/I_G ratio. The degree of disorder was found to decrease as the annealing temperature increased. Therefore, a lower temperature ensures better capacity. Other authors tried to link the slope capacity with the active sites (ASA), and oxygen surface functional groups (CO_x) [40]. Figure 26.e shows that the slope capacity is dependent on both the parameters mentioned above. For the selected HCs (derived from cellulose), higher capacity is gained in the sloping region when materials possess more active sites and CO_x groups. The same authors collected all the physicochemical properties of the HCs (i.e., structure, porosity and surface chemistry) and cleverly presented them as a function of slope and plateau capacity (Figure 26.f). The slope capacity was found to be directly proportional to the active surface area (ASA), the surface functional groups (CO_x), and the micropore volume determined by CO_2 gas adsorption (V_{micro} CO_2). On the contrary, the plateau capacity shows an inversely proportional trend with the slope capacity and therefore increases while the HC's above-mentioned parameters decrease. Thus, the highest plateau capacity is achieved when the materials are exempted from porosity, surface groups, and active sites and when the d_{002} interlayer spaces correspond to the HC obtained between 1400 and 1600 °C (~ 0.37 nm).

It should be mentioned that most of the work reports the gravimetric capacity of HC materials, and only a limited number of works dealt with the volumetric capacity. This parameter is very important when the HC is placed in a real SIB, since its volume must be reduced as much as possible. One detailed work on this topic showed that the volumetric capacity depends on a few parameters, the most important being the electrode porosity after calendaring, and lower porosity inducing higher volumetric capacity[98]. It was shown that the porosity of the electrode after calendaring can be linearly decreased by increasing the interlayer space. Other factors affecting volumetric capacity were found to be intrinsic HC porosity and particle size. Contrary to what was expected, the tapped density did not impact the volumetric capacity.

5 Sodium Storage Mechanisms in Hard Carbons

The Na storage mechanism into hard carbon is still controversial and under debate [43, 274-279]. The interpretation may differ, depending on the different employed carbon precursors. The choice of the precursor (e.g., different varieties of biomass, biopolymers, synthetic precursors, etc.) for hard carbon synthesis plays a critical role in their electrochemical performance due to the difference in the carbon microstructure as well as variations in biomass chemical composition and inorganic impurities present in the precursors [280]. Additionally, the interpretation of the mechanism may differ from one characterization technique to another due to the different probing time scales, bulk and surface sensitivities and hard carbon microstructures.

5.1 Sodium storage mechanism

As mentioned earlier, assigning and interpreting a particular process to a certain potential range is still a matter of debate. During the sodiation of hard carbons, four different types of processes are expected: adsorption, intercalation, pore filling and electrolyte decomposition (Figure 27). Adsorption of Na^+ ions can take place at the hard carbon surface, defect sites or heteroatoms. Intercalation of Na^+ ions into the graphitic layers is expected. The formation of clusters or pooling of Na atoms takes place in the pores of the hard carbons, filling the open as well as closed pores. Finally, electrolyte decomposition on the carbon surface occurs during initial sodiation, leading to the formation of the solid-electrolyte interphase (SEI) and irreversibly trapping a portion of the Na inventory.

As both adsorption and filling occur in the pores, it is important to emphasize that the kinetics of both processes are highly dependent on the type of porosity. Adsorption takes place in the open type porosity, characterized by a capacitive-dominant behavior often associated with the sloping region of charge/discharge curves. In contrast, pores filling occurs in closed pores through a diffusion-dominant process resulting in the formation of quasi-metallic Na clusters, occurring in the low-voltage plateau region of the charge/discharge curves, as proposed by some others [191, 281]. However, there is not full agreement on this fact.

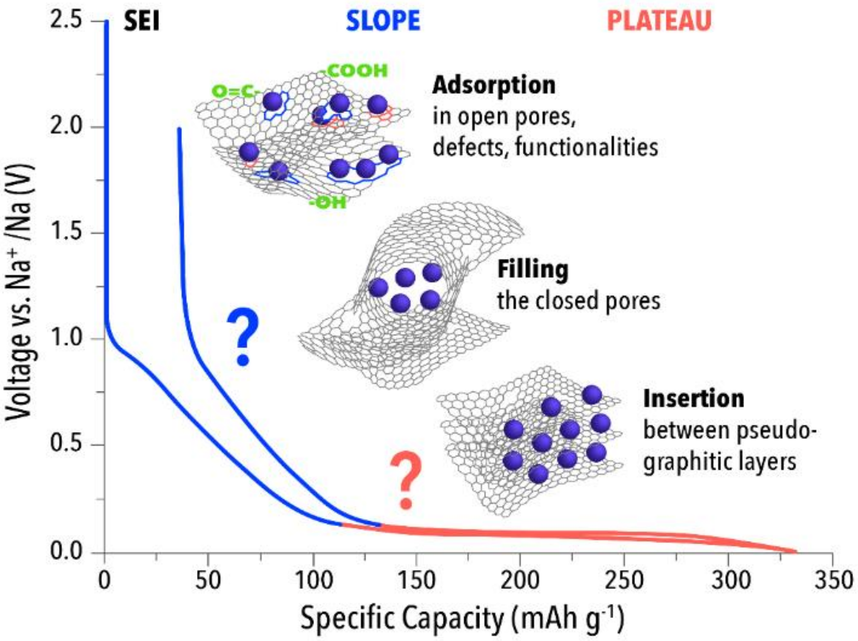

Figure 27: Schematic representation of all possible Na-ion storage mechanisms, as proposed by the authors of this work.

Unlike the surface-controlled capacitive adsorption process at the surface of open pores, Na^+ storage in closed pores is regarded as a diffusion-dominant process, as bulk diffusion is essential for Na^+ ion to access the closed pores in HC, corresponding to the plateau region in the charge/discharge curves. However, some disparities appear in the research community, whether Na appears in ionic or metallic state during pore filling [191]. In addition, it is not well understood how Na^+-ions or Na clusters are filling the closed pores because these pores are inaccessible to gases and liquids.

The study by Kim et al. [281] observed that a multitude of bulk-chemisorbed ions occupied nanometer-scale closed pores surrounded by graphitic domains (Figure 28.a). At approximately 0 V, weakly chemisorbed ions are released from the defective surface, resulting in a two-phase clustering process within the ion-saturated inner surfaces of the closed pores. The clustering reaction is constrained by the closed pore volume. The disorder parameter (f_a) values obtained from SAXS, associated with the shape and order of closed pores, indicated a transition from a random two-phase mixture to randomly spread globular pores with increasing annealing temperature. This transition disrupted Na^+-ion diffusion into the overall closed pores, leading to limited plateau capacities, particularly at higher annealing temperatures. This is a very insightful observation, which might suggest that the closed pore filling mechanisms are different depending on the HC annealing temperatures and might explain in some extent the contradictory results observed between different works using different materials.

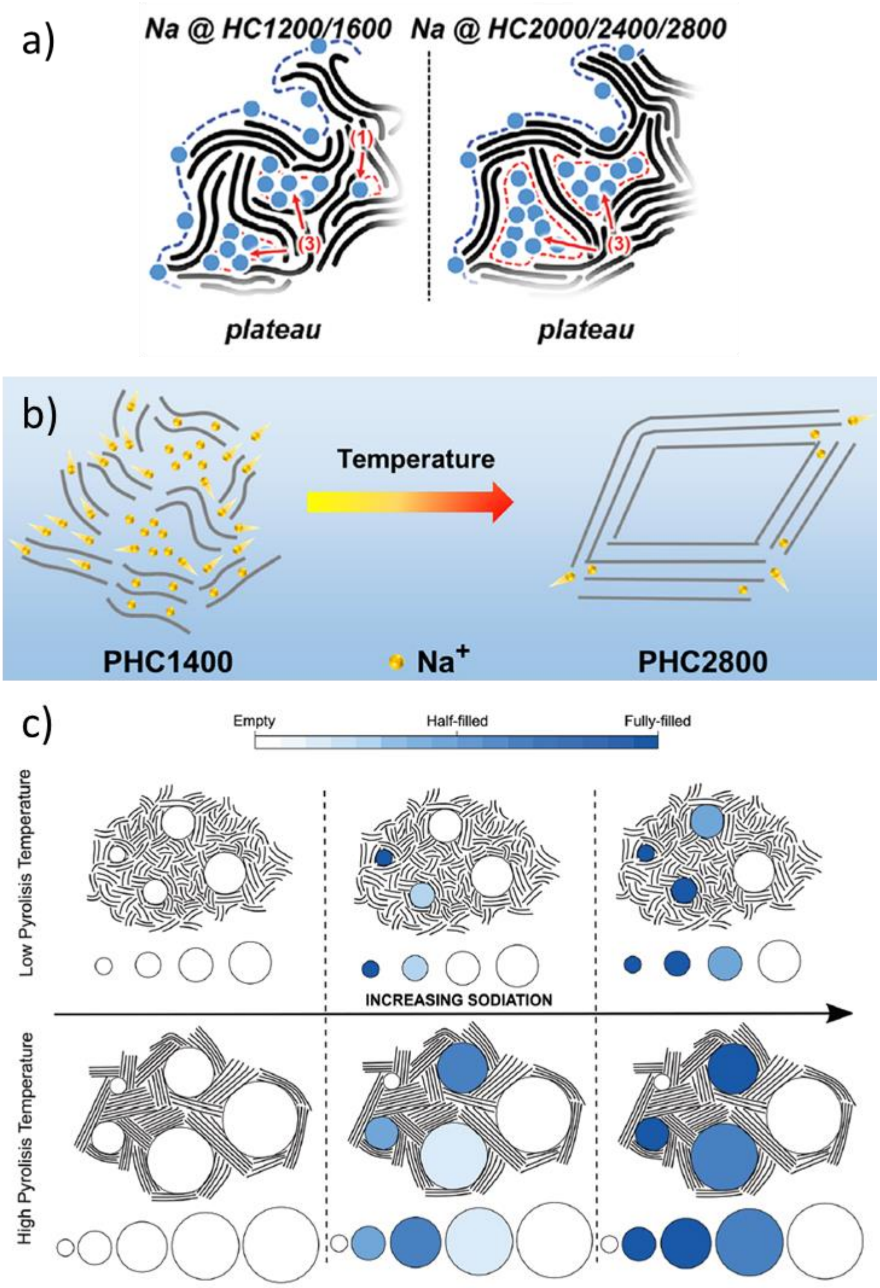

Figure 28: a) Schematics of the sodium storage mechanism based on the microstructural changes of the HC by thermal annealing: 1) bulk chemisorption and 3) clustering. Reprinted with permission from [281]*, Copyright 2023, John Wiley and Sons; b) Schematic illustration of the transformation of accessible closed pores. Reprinted with permission from* [282]*, Copyright 2022, American Chemical Society; and c) Schematic representation of the microstructure and the storage of* Na^+*-ions in closed pores for HCs synthesized at different pyrolysis temperatures. The circles represent closed pores whereas the black lines represent graphene layers. The blue scale represents the extent to which the pores are filled with sodium ions; white indicates empty pores while dark blue indicates fully filled pores. Reprinted with permission from* [283]*, Copyright 2023, John Wiley and Sons.*

The study of Yuan et al. [282] corroborates the metallic nature of Na during pore filling. *Ex situ* XPS analysis was employed to examine the binding state of sodium in pitch-derived HC. The Na *1s* spectrum for PHC1400 exhibited a stronger peak at 1071.7 eV, shifting to a higher binding energy during discharge to 0.01 V. This indicates the presence of quasi-metallic clusters, serving as evidence for sodium filling in closed pores.

The reversible transformation of the Na *1s* spectrum during desodiation confirms the reversibility of closed pore filling. However, the authors propose that not all closed pores offer effective active sites for Na storage, and the accessibility of closed pores depends on diffusion through graphite domains. The size of pseudo-graphite domains, rather than interlayer spacing, plays a significant role in determining whether or not Na^+ ions can enter closed pores. Increased pseudo-graphite domain size reduces channels for Na^+ ion diffusion, making closed pores less accessible (Figure 28.b). However, in many cases, the increase in the lateral size of pseudo-graphitic layers (La), is accompanied by the decrease of interlayer space (see Figures 9 and 10), therefore, both parameters might impact the closed-pore filling.

Meanwhile, Iglesias et al.[283] report that the nature of Na during pore filling is highly dependent on the pyrolysis temperature. At lower pyrolysis temperatures, smaller pores fill preferentially, while higher temperatures lead to preferential filling of medium-sized pores. They propose the pore filling mechanism proceeds in sequential steps: Na adsorption to defect sites in pore walls, followed by cluster growth. Higher defect concentration in lower temperature HC favors smaller pore filling, maintaining mainly ionic Na character. Only when this is done, the filling of larger pores occurs, leading to the formation of small clusters. For high-temperature obtained HC, where the defect concentration is lower, the medium size pores fill first, and have an increased pseudo-metallic sodium character. The authors conclude that the defect concentration and pore characteristics influence Na cluster size and storage capacity (Figure 28.c).

Bearing this in mind, the Na storage mechanism can be classified into four distinctive models currently accepted in the Na battery community (Figure 29) [58, 279]. Before describing the individual models, it should be noted that electrolyte decomposition and subsequent SEI formation are not included in the mechanism since they are not associated with charge storage processes. However, the formation of a stable and robust SEI is essential for the satisfactory performance of hard carbons.

The first model can be described as the intercalation-filling process. Within this model, the sloping region is attributed to Na^+ ion intercalation into graphitic layers. The plateau region is due to Na atom insertion into the hard carbon micropores [20, 284]. The second model can be described as the adsorption-intercalation process. In the sloping region, the possible storage sites for the adsorption of Na^+ ions are the hard carbon surface, defect sites, and edges of graphite-like domains or heteroatoms, whereas in the plateau region, intercalation into the graphitic layers takes place [92, 116]. The third model can be designated as the adsorption-filling process. Within this model, Na^+ ions are adsorbed to the surface/defects/edges/heteroatoms in the sloping region, and Na atoms fill the micropores in the plateau region [75, 153]. The last and fourth model can be described as a three-stage process. In this model, the galvanostatic curve is divided into three reaction regions. In the sloping region, Na^+ ions are adsorbed to the surface/defects/edges/heteroatoms; in the plateau region, Na^+ ions intercalate into the graphitic layers; and at the end of the plateau close to the cut-off voltage, Na atoms fill the micropores [43].

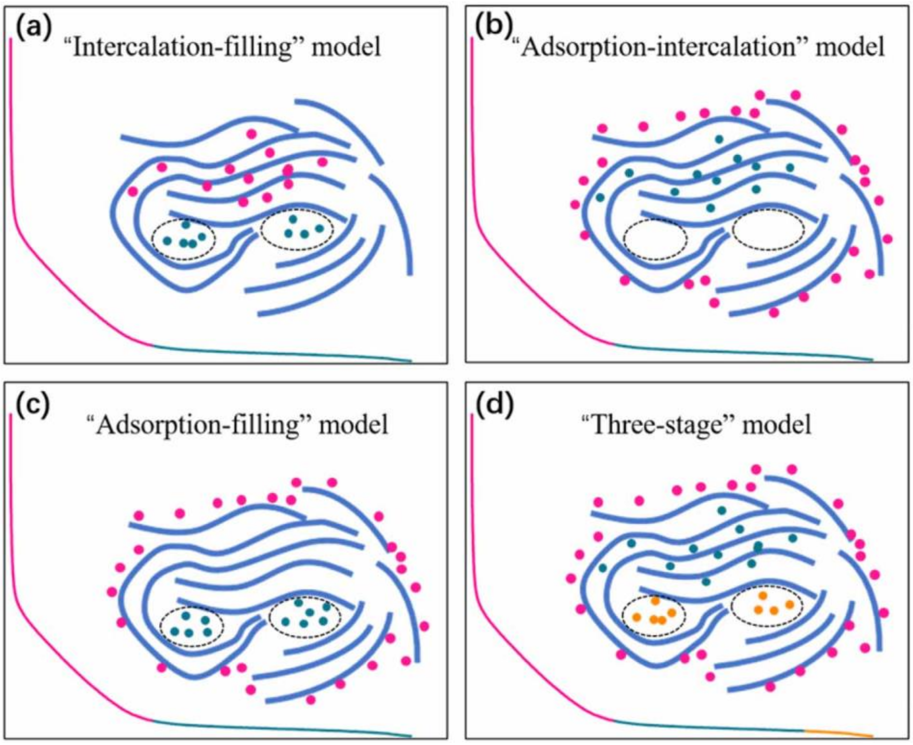

Figure 29: Na storage mechanism divided into four distinctive models: a) intercalation-filling process, b) adsorption-intercalation process, c) adsorption-filling process and d) three-stage process. Reprinted under Creative Commons Attribution 4.0 license [58]. Copyright 2020, The Authors. Published by IOPscience.

Most of the literature agrees with the model by Stevens and Dahn dedicated to alkali metals [20, 23, 284]. The model was mainly based on *in situ* XRD, small-angle X-ray scattering (SAXS) and wide-angle X-ray scattering (WAXS) data. Stevens and Dahn proposed a model consisting of a two-stage Na^+ ion insertion mechanism (Figure 30.a-b) as part of a broader structural model known as the “house of cards” or “falling cards” model. Stevens and Dahn distinguished two regions on the electrochemical potential curve, namely, the sloping region at potentials higher than 0.1 V *vs.* Na/Na^+ and the plateau region at potentials lower than 0.1 V *vs.* Na/Na^+. According to the model, the sodium ions are inserted between nearly parallel layers of carbon in the sloping region, followed by pore filling in the plateau potential region [284]. From a structural point of view, Stevens and Dahn described the hard carbons as a combination of pseudo-graphitic sp^2 hybridized nanodomains (2 to 3 graphene layers according to the “house of cards” model [284], up to 5 layers according to other literature [46, 202]) and sp^3 hybridized amorphous regions (vacancies, Stone–Wales defects).

The intercalation-filling model was further supported by Komaba et al. [285] using *ex situ* XRD (Figure 30.c) to observe that the (*002*) reflection peak shifts to a lower angle when the hard carbon is sodiated up to 0.1 V. They discussed that the interlayer distance increases during the sodiation process, which proves that the insertion of the charge carriers inside the graphitic domains occurs in the sloping region. Furthermore, *ex situ* SAXS (Figure 30.d) was used on a sodiated sample below 0.2 V. SAXS revealed a decrease in scattering intensity at approximately 0.03 to 0.07 $Å^{-1}$ originating from the hard carbon nanopores. This decrease is attributed to the Na^+ ions inserted into the nanovoids within the lower potential range [284, 285]. Additionally, it was assumed that sodium storage at a low potential (5 mV) close to the metal deposition would result in sodium clustering with the metallic character of the Na^+ ions. This metallic pooling was proven by Stratford et al. [286] using *operando* ^{23}Na solid-state nuclear magnetic resonance (ssNMR). Based on *operando* ^{23}Na ssNMR, they proposed a two-stage mechanism (Figure 30.e). The sloping region, where ionic Na^+ ions are formed, consists of charge localization near defects. They claim that the defects are responsible for larger interplanar distances, and therefore, insertion may commence in this sloping region, which is associated with charge localization. This was further supported by pair distribution function (PDF) data, which indicates that turbostratically disordered graphene-like fragments affect the interlayer arrangements. At low potentials, where a plateau is present due to intercalation and Na pooling, they observed a quasi-metallic nature of Na ions or atoms as clusters with domains of coherence lengths superior to 10 Å (Figure 30.e). Surprisingly, using the same technique for *ex situ* measurements with electron paramagnetic resonance, the quasi-metallic sodium environment was not detected in closed nanopores at the end of discharge (0 V *vs.* Na/Na^+). They proposed that this discrepancy between *operando* and *ex situ* NMR results could arise due to the extreme reactivity of sodiated hard carbon [287]. Morita et al. [288] refuted this hypothesis by showing that extracted sodiated electrodes show reversible desodiation when mounted in a fresh cell. Another possible explanation for this disparity could be that the near-metallic state of sodium in the micropores is in the metastable phase. Operando ssNMR is sensitive towards metastable states occurring during cycling, which would not otherwise be detected by *ex situ* experiments since the Na metal could have disappeared before the hard carbon electrode was collected for characterization [289]. Complementary works using ^{23}Na NMR technique to understand the Na$^+$-ion storage are nicely gathered in the review of Gotoh [290].

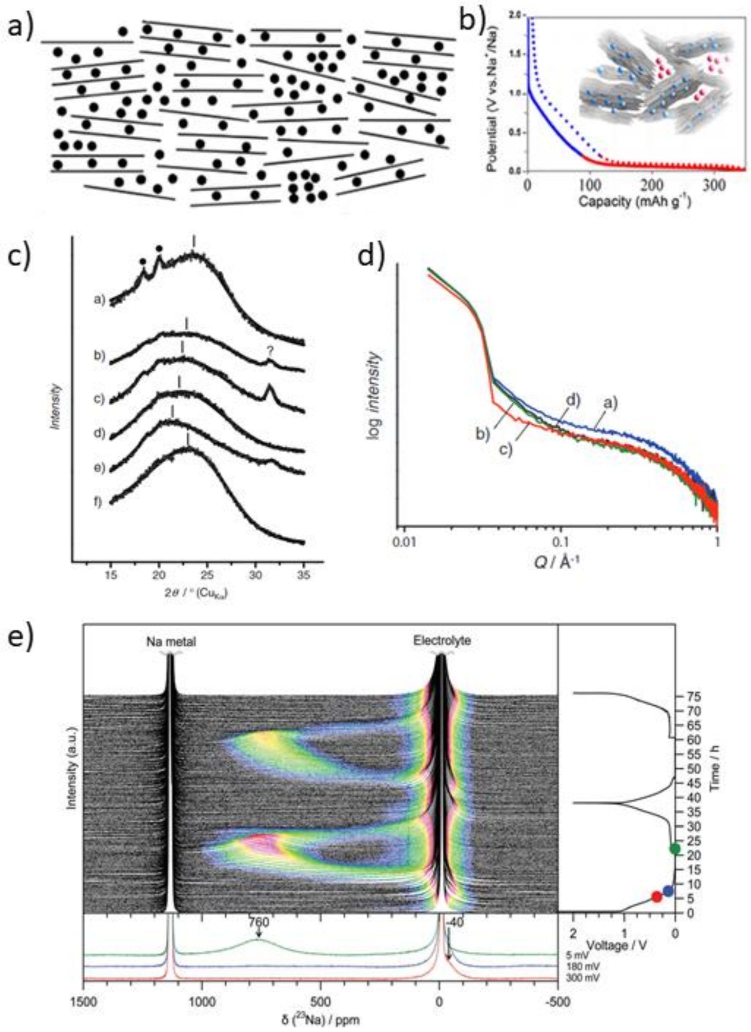

Figure 30: a) Representative sketch of the falling card model. Reproduced by permission from [284]. Copyright 2000, IOP Publishing Ltd, b) galvanostatic curve representing falling card model. Reprinted with permission from [43], Copyright 2015 American Chemical Society. c) ex situ XRD for hard carbon electrodes at different potentials and d) ex situ SAXS for hard carbon electrodes at different potentials. Reprinted with the permission from [285]. Copyright 2011, John Wiley & Sons and e) operando ^{23}Na solid-state NMR. Reprinted under the terms of CC BY 3.0 DEED licence [286], Copyright 2016, The Authors, Published by Royal society of Chemistry.

These findings and contradictions make the plateau region difficult to ascribe to a process with full certainty, and more models have been suggested [20, 43, 75, 92, 153, 278, 291, 292]. The "falling cards" model based on the intercalation–adsorption model did not take into account the presence of defects, heteroatoms and/or functional groups at the edges of graphite-like domains as storage sites for sodium at high voltages. These defects vary from surface dangling bonds at the edge of the turbostratic nanodomains (TNDs) to monovacancies, divacancies, Stone–Wales defects and curvatures in graphene sheets with the presence of sp^3-linking carbons that connect the randomly oriented nanodomains [43]. The apparent contradiction between several reports proposing that Na^+ ion pore filling occurs first and then a pooling mechanism against adsorption followed by interlayer intercalation indicates that both mechanisms of intercalation and pore filling could occur simultaneously at the plateau region [293].

To fill the missing gaps of the "falling cards" model, a three-stage model was proposed (Figure 31). It consists of defect adsorption of Na^+ in the sloping region, whereas the plateau region is characterized by Na^+ ion intercalation into the graphitic layers followed by pore filling in the nanopores at lower voltage ranges prior to sodium plating. This model was suggested by Bommier et al. [43] when a sucrose source was pyrolyzed at different temperatures. They suggested that the sloping capacity increases due to the higher defect concentration expressed by the integrated I_D/I_G ratio when a linear relationship was reported between the slope of the capacity and the concentration of the defects. The high sloping capacity was attributed to the hard carbon that contains the highest defect concentration. Other supplementary techniques were used to investigate the sodiation mechanism, namely, the galvanostatic intermittent titration technique (GITT) and *ex situ* XRD measurements. The former was used to prove that the storage mechanism changes in the lower voltage range before reaching the cut-off potential. Meanwhile, the latter was used to investigate the change in the graphitic layer stacking during the sodiation/desodiation process. From the GITT data, it was reported that the diffusion associated with the sloping potentials is much faster than in the plateau region, which confirms that the initial sodiation happens on readily accessible sites of amorphous carbon edges. When further sodiation takes place at lower voltages, the Na^+ ions will diffuse inside the graphitic layers. This step is considered energetically demanding since Na^+ ions have to overcome the repulsive charge gradient from the previously bound Na^+ ions to the TND edges to finally intercalate between the graphitic sheets. Therefore, adsorption on the defect sites occurs at higher potential values prior to intercalation. Based on the same aforementioned techniques, the sodiation mechanism was extensively investigated for the plateau region. They deduced that the steep drop in the diffusivity, as well as the reversible expansion and contraction of the d-spacing for a voltage window from 0.2 to 0.01 V *vs.* Na/Na$^+$, are indicators of the intercalation process. The observed GITT measurements from 0.05 V to the cut-off voltage suggested that the sodiation of the charge carriers at the plateau region could not be attributed to the sole intercalation process between the graphitic sheets. The measurements show that the diffusivity values increase, described as a U-turn-like reversal shape, below 0.05 V instead of being continuously low upon sodiation. This was explained by the fact that the binding energy at the nanodomain edges becomes weaker in the low potential range. Due to the higher kinetics, the pore filling mechanism is more favoured compared to intercalation.

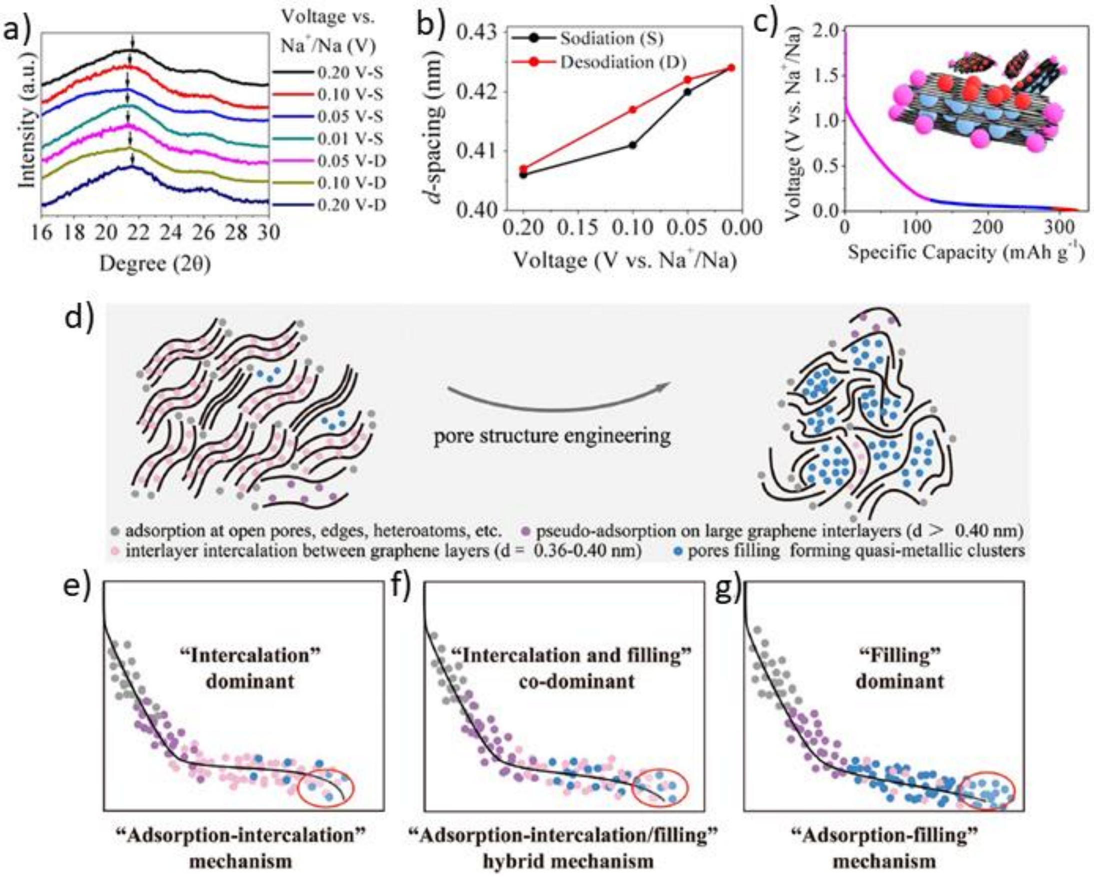

Figure 31: a) Ex situ XRD patterns for different sodiation and desodiation conditions, b) d-spacing plots, c) galvanostatic curve for the three-stage process. Reprinted with permission from [43], Copyright 2015, American Chemical Society, d-g) schematic illustration of the improved three-stage process, a so-called microstructure-dependent mechanism ("adsorption – intercalation/filling" hybrid mechanism). Reprinted with the permission from [293], Copyright 2022, John Wiley & Sons.

This hypothesis was further corroborated using the *ex situ* XRD technique (Figure 31.a-b), which does not show any expansion/contraction of the two adjacent graphene layers close to the cut-off potential. Therefore, the last storing mechanism is attributed to the pore filling process that occurs at very low potential close to the metal plating, which takes place at –0.02 V *vs.* Na/Na^+ [43].

More recently, based on new findings [293] an improved three-stage process, the so-called microstructure-dependent mechanism ("adsorption-intercalation/filling" hybrid mechanism), was proposed (Figure 31.d-g). It was suggested that interlayer intercalation and micropore filling concurrently contributed to the plateau region of the hard carbon. Cao et al. concluded that if hard carbon has abundant pseudo-graphitic nanodomains, intercalation is the main driving force in the plateau, and pore filling occurs at the end of discharge (Figure 31.e). On the other hand, if hard carbon is rich in micropores, the plateau capacity is due to micropore filling and few-layer intercalation (Figure 31.g).

An alternative multistage storage mechanism concept was recently suggested based on *in situ* Raman scattering, density functional theory (DFT) and band structure calculations [292]. According to the research group [292], sodium insertion into hard carbon occurs in four different stages (Figure 32). First, adsorption on defects and reactive surface sites takes place at the very beginning of sodiation. Second, the intercalation takes place initially at defect sites between the layers, followed by the filling of the remaining layers up to a maximum amount of NaC_{24} in terms of stoichiometry, which theoretically results in 93 mAh g^{-1} of gravimetric capacity at the sloping region. Finally, in the plateau region, Na^+ ion pooling into nanopores takes place. The authors [292] suggested that defects are essential to initiate sodium insertion and that the obtained capacity in the sloping region depends on the defect concentration with a maximum amount of NaC_{24}. Additionally, excessive defect concentration has a detrimental effect because the activation barriers for sodium diffusion increase close to the defect sites. They speculated that this could be one of the reasons for the irreversible capacity of trapping the adsorbed sodium. Finally, it is suggested that the plateau capacity depends on the nanopores, therefore, optimization of the hard carbon pore structure and volume could result in an increase in capacity.

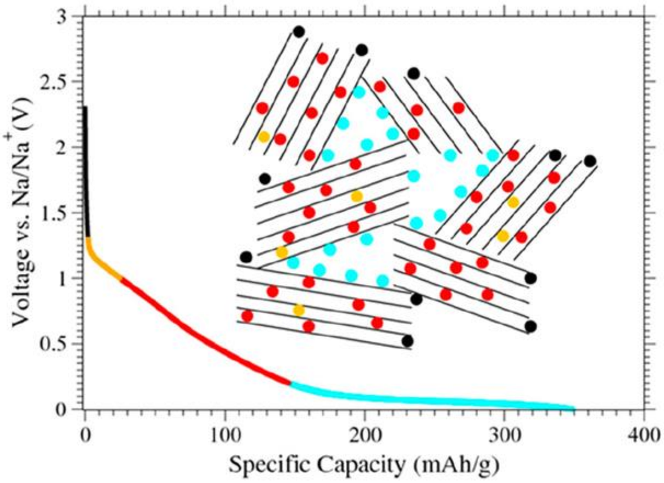

Figure 32: Schematic representation of the multistage storage mechanism concept: adsorption on surface sites (black), filling of defects in graphitic layers (orange), filling of the layers (red), and adsorption on nanopores (light blue). Reprinted with permission from [292], Copyright 2018, American Chemical Society.

This type of model was also reported by Titirici et al. [274] when hard carbon structures were synthesized using hydrothermal treatment of glucose with citric acid as a catalyst and further carbonized at different temperatures ranging from 1000 °C to 1900 °C. In this study, the electrode volume expansion during cycling was investigated using *in situ* electrochemical dilatometry (ECD) as a novel technique to investigate sodium ion storage. They found that the volume expansion of the electrode is more significant in the sloping region compared to the plateau. Based on this result, the authors hypothesized that in the sloping region, adsorption of Na^+ ions on the disordered graphene layers occurs. Consequently, Na^+ ion adsorption leads to material expansion. Following adsorption, intercalation into graphene layers with suitable spacing takes place, forming a low voltage plateau. Finally, in the plateau region, Na^+ ion storage dominates over pore filling [274]. More recently, it has been shown by in operando SAXS measurements that closed pore filling and intercalation of Na^+ occurs simultaneously in the plateau region[283]. Apparently, not all pores are filled, suggesting that plateau capacities can still be improved.

A detailed understanding of the mechanism processes (Table 5) as well as establishing a potential dependence of these processes upon sodiation is crucial for the development of advanced and high-performance hard carbon anodes. However, it appears that during studies of the Na storage mechanism, discrepancies arise due to the large variety of hard carbons and the different processing parameters used. Even with the same characterization techniques, contradictory results are obtained: Zhang and Bommier both performed *in situ* XRD measurements and obtained different results. Zhang produced carbon nanofibers derived from a PAN precursor and did not observe any shifts in the position of the *(002)* peak [75]. Meanwhile, Bommier produced sucrose-based hard carbons and observed notable shifts in the position of the *(002)* peak [43]. Therefore, a consensus on one absolute Na storage mechanism in hard carbons appears hardly achievable. Instead, research should focus on generalizing the Na storage mechanism based on the various microstructures that can be obtained by the pyrolysis process. Below is a descriptive table (Table 5) overviewing the aforementioned references that used different techniques to decipher and shape the Na^+ ion storage models.

Table 5: Different storage mechanisms reported by several studies

Model Type	Voltage region	Characterization technique
Intercalation Filling	Sloping: graphitic intercalation	SAXS WAXS [23, 284], *ex situ* XRD [285], *operando* Na NMR [275, 286]
	Plateau: micro pore filling	
Adsorption Intercalation	Sloping: adsorption on defect sites	*in situ* XRD[213], *ex situ* NMR, EPR [46, 116], ab initio simulations [240]
	Plateau: graphitic intercalation	
Adsorption Filling	Sloping: adsorption on defect sites	N_2, O_2, CO_2 gas sorption [180], TPD–MS [40], XPS[75]
	Plateau: micro pore filling	
Three stages Process	Sloping: adsorption onto defect sites	Raman spectroscopy [43, 293], Neutron PDF[43], GITT [43, 293], *ex situ* XRD half-cell testing [43], *operando* SAXS[283]
	Plateau: intercalation, followed by pore filling	
Multi stages Process	Sloping adsorption on defect sites. Insertion between the layers followed by filling up of the layers	*in situ* Raman scattering [292], DFT band structure calculations [292], *in situ* ECD [274]
	Plateau adsorption on pore walls, followed by metal pooling	

5.2 Solid electrolyte interphase (SEI)

While the determination of the Na storage mechanism is of paramount importance, an in-depth understanding of another process, briefly introduced at the beginning of this section, is also indispensable in the formulation of hard carbons. This process is the decomposition of the electrolyte at the carbon surface, resulting in the formation of the solid electrolyte interphase (SEI). It is one of the most important parameters concerning anodic materials in general, as it determines the amount of active material consumed in the initial sodiation step and tailors/determines the subsequent stable cycling.

The concept of SEI formation was first proposed by Peled in 1979 [294]. He proposed that a passivation layer is formed on the surface of the alkali/alkaline metal, composed of insoluble products, because of side reactions upon contact of the metal with the electrolyte solution. According to Peled, the SEI possesses the properties of a solid electrolyte, acting simultaneously as an ionic conductor and an electronic insulator, hence the name “solid-electrolyte” interphase. Even at that time, nearly 50 years ago, Peled stated that a proper anodic SEI is the key to the operation of nonaqueous batteries, which remains true even today [294]. Research on SEI formation in Li-ion batteries has received enormous attention. Meanwhile, research on SEI formation in Na-ion batteries began at the beginning of the previous decade, concurrent with intensive research on hard carbons [295]. As in the case of other cell components, especially cathode materials, one would expect that the chemistry of SEI formation is analogous for both systems. However, the phenomenon of SEI formation is very distinctive from one system to another due to the different physical and chemical properties of Li^+ and Na^+ ions, including the ionic radius, solvent energy and redox potential [296]. In general, an ideal SEI must satisfy several demands such as:[297]

- → Acting as an electronically insulating material to prevent continuous electrolyte decomposition;
- → Good ionic conductivity to facilitate the transport of Na^+;
- → Allow desolvation of Na^+;
- → Being insoluble in the cell operation environment to prevent continuous degradation.

The process of SEI formation can be divided into four parts, Figure 33. Initially, solvated Na^+ transport from the bulk electrolyte to the outer surface of the electrode. Thereafter, the Na^+ ions desolvate and migrate to the surface of the electrode. In the next step, a portion of Na^+ is consumed to form the SEI layer through an irreversible reaction. Finally, the remaining ions are able to pass through the formed layer and insert into the host electrode [298].

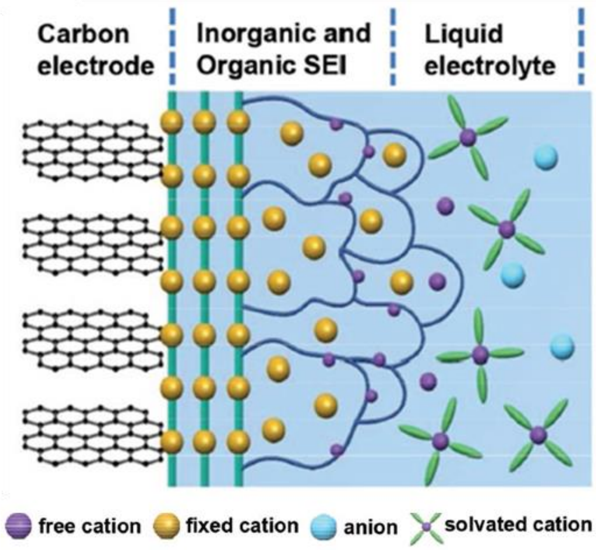

Figure 33: Transfer of Na$^+$ from the bulk electrolyte through the SEI layer to the host electrode Reprinted with the permission from [298]. Copyright 2017, John Wiley and Sons.

Several authors performed X-ray photoelectron spectroscopy (XPS) analysis of cycled hard carbon electrodes and concluded that the SEI is composed of a mixture of inorganic (NaF, NaCl, Na_2CO_3 and Na_2O) and organic (alkali carbonates, carboxylates, carbonyls, ethers and epoxides) compounds [127, 285, 299-303]. Some authors have also reported the formation of sodium ethylene dicarbonate (NEDC) as the main decomposition product of carbonate-based solvents [301, 302]. However, the SEI composition is closely connected to the choice of electrolyte. The majority of electrolytes used in SIBs are based on sodium salts, such as $NaClO_4$, $NaPF_6$ and NaTFSI, dissolved in carbonate-based organic solvents, such as ethylene carbonate (EC), propylene carbonate (PC), dimethyl carbonate (DMC) and diethyl carbonate (DEC) [127, 301, 304]. Furthermore, additives, such as fluoroethylene carbonate (FEC) and vinyl carbonate (VC), have been added to improve the SEI stability [301, 305]. Eshetu *et al.* [300] studied the influence of different salt anions on SEI formation. They found that the degradation of electrolyte salt dictates the composition of the inorganic species in the SEI. Additionally, they showed that the thickness of the SEI is dependent on the salt anion. In this regard, $NaClO_4$-based electrolytes form thicker SEIs, and $NaPF_6$- and NaTFSI-based electrolytes form thinner SEI layers. On the other hand, in another work, Eshetu *et al.* [17] showed that the composition of organic species is highly dependent on the reduction of linear carbonates, particularly DEC and DMC.

Reports suggest that the solubility of the SEI in Na-ion batteries is more severe because the SEI components are mainly unstable organometallic compounds that are highly soluble in organic electrolytes. The continuous dissolution of the SEI leads to increased self-discharge of the cell. Moreover, the dissolution of the SEI exposes the carbon surface to the electrolyte, leading to further electrolyte degradation. The ensuing growth of the SEI additionally consumes the active material, leading to low Coulombic efficiencies in the subsequent cycles. Therefore, the solubility, morphology, structure, and composition of the SEI layer were studied by several techniques, as seen in Figure 34.

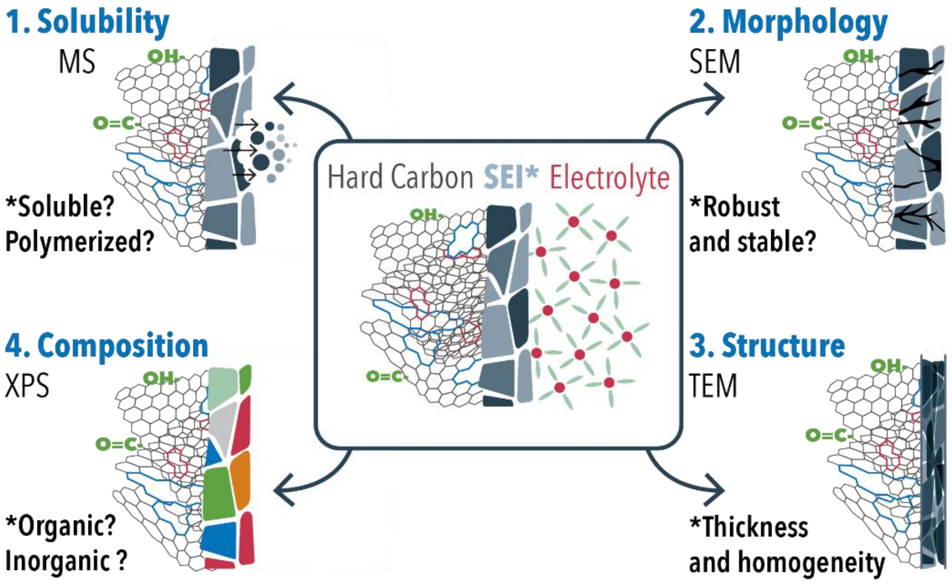

Figure 34: Representation of SEI layer at the surface of HC and the main techniques used to determine its properties, as proposed by the authors of this work.

Mogensen *et al.* [297] studied SEI dissolution on high-surface-area SuperP anodes via galvanostatic cycling combined with prolonged pause periods (Figure 35.a). They compared the charge capacities of the last cycle before the pause period and the second cycle following the pause period. In this way, they were able to monitor the static stability of the SEI without influences from volume expansion and polarization. From the rate of self-discharge, they were able to calculate the amount of capacity lost due to SEI dissolution. They concluded that in cells with Na metal electrodes, the capacity loss amounted to approximately 80% of the overall cell capacity compared to only 20% capacity loss for cells with Li-metal electrodes (Figure 35.a).

Additionally, synchrotron-based hard X-ray photoelectron spectroscopy (HAXPES) was performed on the SuperP electrode cycled in a Na-half cell after a prolonged period of pause (72 h or 168 h). From the obtained data, they observed a decrease in SEI thickness, indicating the dissolution of the SEI when in contact with the electrolyte. Ma *et al*. [306] adopted a similar protocol to study the SEI solubility in different solvents; 1M $NaPF_6$ was employed as the electrolyte salt in different solvents, namely, PC, EC:PC, and EC:DEC, and they concluded that

EC:PC consumed the least capacity for SEI formation, while PC consumed the most (Figure 35.b). However, EC:DEC exhibited the lowest SEI dissolution rate, while PC again exhibited the worst performance (Figure 35.c). Finally, the solubilities of Na_2CO_3 and NaF and their lithium analogues in PC and EC:DEC were studied by ICP–OES. The solubilities of sodium inorganic compounds are an order of magnitude higher than those of their lithium analogues.

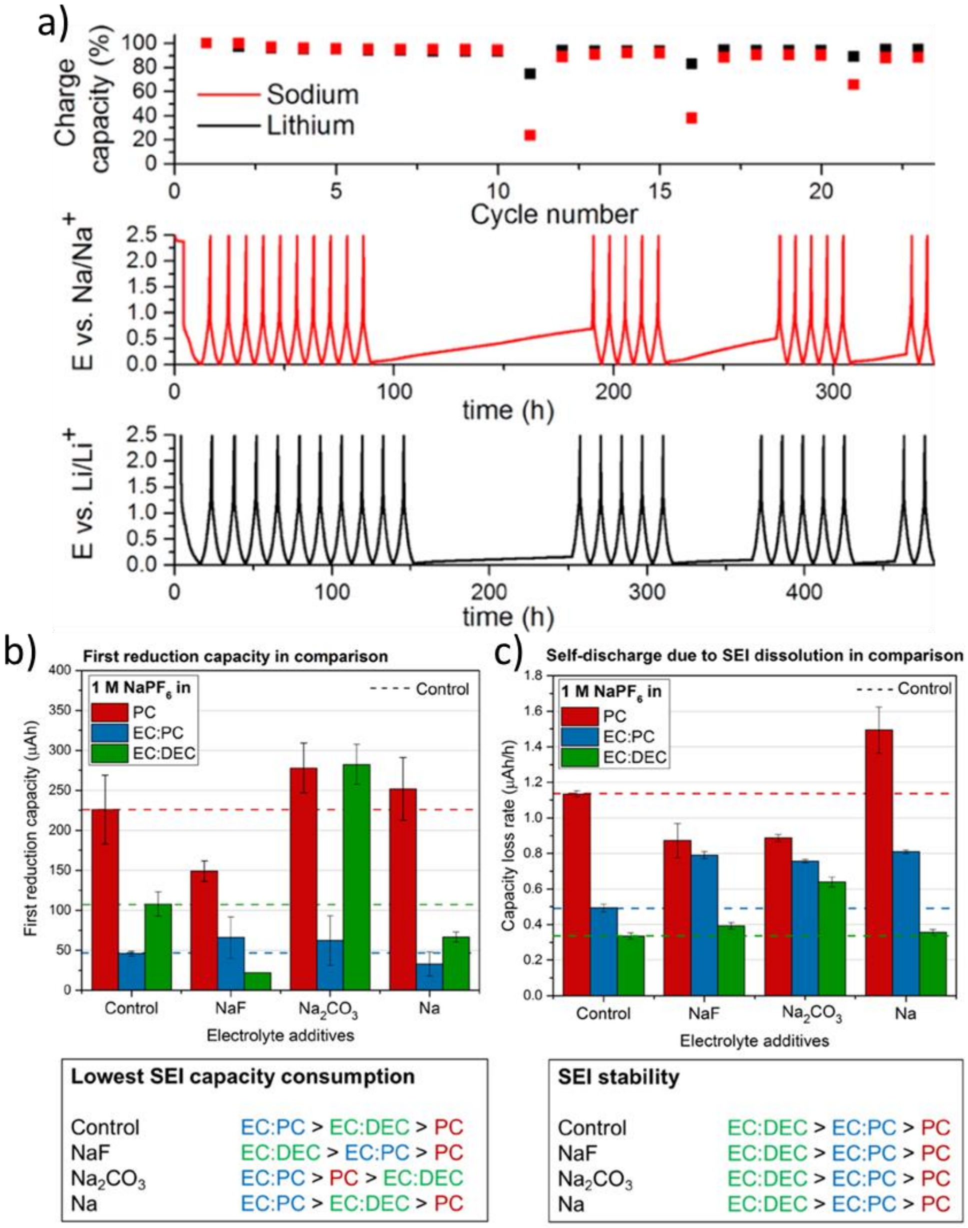

Figure 35: a) Comparison of SEI dissolution in Na- and Li-based cells. Reprinted with permission from [297], Copyright 2016, American Chemical Society. b) Effect of different solvents on the consumed capacity for SEI formation and c) effect of different solvents on the SEI dissolution rate. Reprinted under the terms of CC BY 4.0 DEED licence [306].Copyright 2020, The Authors, Published by Wiley-VCH GmbH.

Solutions to mitigate continuous SEI growth ranging from adapted cycling protocols, rational electrode design and electrolyte additives, have already been explored [307]. Among them, the addition of sacrificial compounds to the electrolyte is the most attractive option, and understanding the effect of electrolyte additives on the formation of the SEI is crucial in the quest to mitigate its continuous growth. The most well-known and studied electrolyte additive is fluoroethylene carbonate (FEC). Komaba *et al.* [295] were the first to report the benefits of FEC addition in Na-ion batteries. They showed that the addition of 2 wt% FEC to a solution of 1 M $NaClO_4$ in PC results in more stable long-term cycling (Figure 36.a, curve b in inset). However, when increasing the amount of FEC to 10 wt%, a detrimental effect was observed as the electrochemical performance decreased. Finally, they concluded that other additives, such as difluoroethylene carbonate (DFEC) and vinylene carbonate (VC), do not improve cycling stability. Rather, a decrease in the reversible capacity of hard carbon electrodes was observed. Since then, several research groups have followed this example and studied the effect of FEC in Na-ion batteries. However, contradictory reports have arisen on its effect on the performance of hard carbons. Dahbi et al. showed that the addition of 0.5 wt% FEC to a solution of 1 M $NaPF_6$ in PC and PC:EC increases the initial Coulombic efficiency and improves the long-term cycling stability (Figure 36.b, curves a and b). Using HAXPES, they concluded that similar chemical species are formed at the hard carbon surface independent of the FEC addition. However, they claimed that with the addition of FEC, a more desirable passivation layer formed, simultaneously suppressing the accumulation of decomposition products of PC and $NaPF_6$ at the hard carbon surface [299]. The same observations were corroborated by Fondard *et al.* [301]. They studied the effect of the addition of small amounts of FEC and DMCF on the cycle life and SEI composition. Improved cycle life was observed with the addition of FEC, while the DMCF addition did not provide any improvements (Figure 36.c). The electrolyte with FEC formed an SEI with increased amounts of sodium ethylene dicarbonate (NEDC) and NaF. They postulated that NEDC is the principal Na^+ conducting species. Meanwhile, the increased amount of NaF leads to better cycling stability, yet its exact role is still unclear. They hypothesized that an increased amount of an insoluble species, such as NaF, stabilizes the SEI and limits the solubility of other compounds. On the other hand, Ponrouch *et al.* [308] observed increased polarization and lower iCE when 2 wt% FEC was added to a mixture of 1 M $NaClO_4$ in PC:EC (Figure 36.d). Dugas *et al.* [305], however, postulated that the detrimental effects of FEC arise from the kinetic limitations of the Na metal electrode rather than the hard carbon. With the addition of 3 wt% FEC to the mixture of 1 M $NaPF_6$ in EC:DMC, increased impedance was observed in Na symmetrical cells, leading to larger overpotentials and less stable stripping/deposition processes (Figure 36.e). When performing electrochemical measurements with hard carbon electrodes, a slight increase in irreversible capacity was observed with the FEC electrolyte. Nevertheless, they claimed that overall, the addition of FEC is beneficial because it limits Na reactivity towards the electrolyte via the growth of a passivation layer. This was further confirmed by gas chromatography–mass spectrometry (GC–MS) and gas evolution experiments, where it was shown that FEC decomposed prior to other solvents, and no EC and DMC decomposition products were detected.

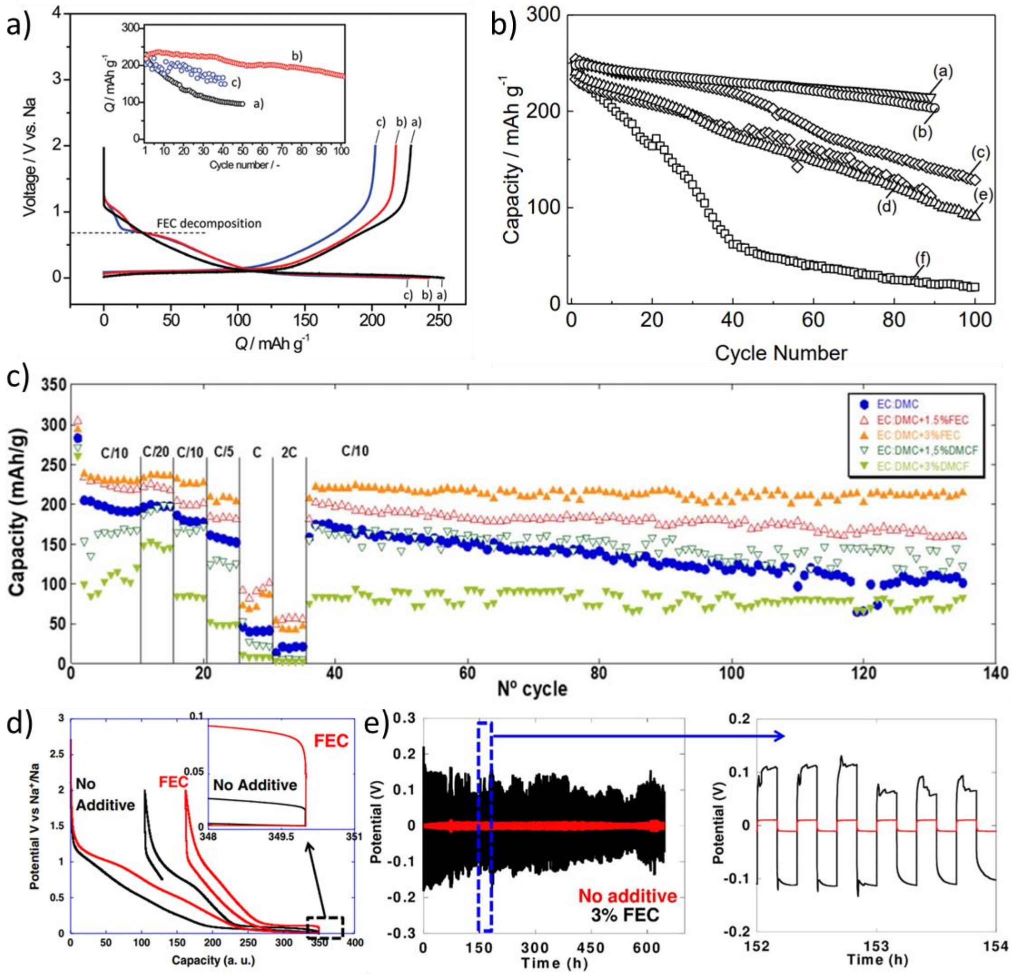

Figure 36: improved cycle life and stability with FEC addition: a) reprinted with permission from [295] Copyright 2011, American Chemical Society. b) reprinted with permission form [299]. Copyright 2016, John Wiley and Sons, c) reprinted under the terms of CC BY-NC-ND 4.0 DEED licence [301], Copyright 2020, The Authors, Published by IOPscience. d) lower iCE and increased polarization in FEC electrolyte. Reprinted with permission from [308] Copyright 2013, Elsevier and e) increased polarization in FEC electrolyte during stripping/deposition of Na symmetrical cells. Reprinted under the terms of CC BY-NC-ND 4.0 DEED licence [305], Copyright 2016, The Authors, Published by IOPscience.

Other reports also suggest that the main reason for capacity fading in Na-ion batteries is not the degradation of hard carbon electrodes but rather the reactivity of the Na metal electrode towards the electrolyte. Indeed, the work performed by Iermakova *et al.* [309] showed that cycling of Na symmetrical cells presents large overpotentials, resembling the behaviour of diffusion-limited processes (Figure 37.a). Meanwhile, stripping/deposition measurements of Li symmetrical cells exhibit low polarization and smooth curves. Moreover, scanning electron microscopy (SEM) images of Na electrodes were taken upon immersion for 24 h and after CV measurements. Rough surfaces were observed, and large particles detaching from the substrate were observed after CV measurements.

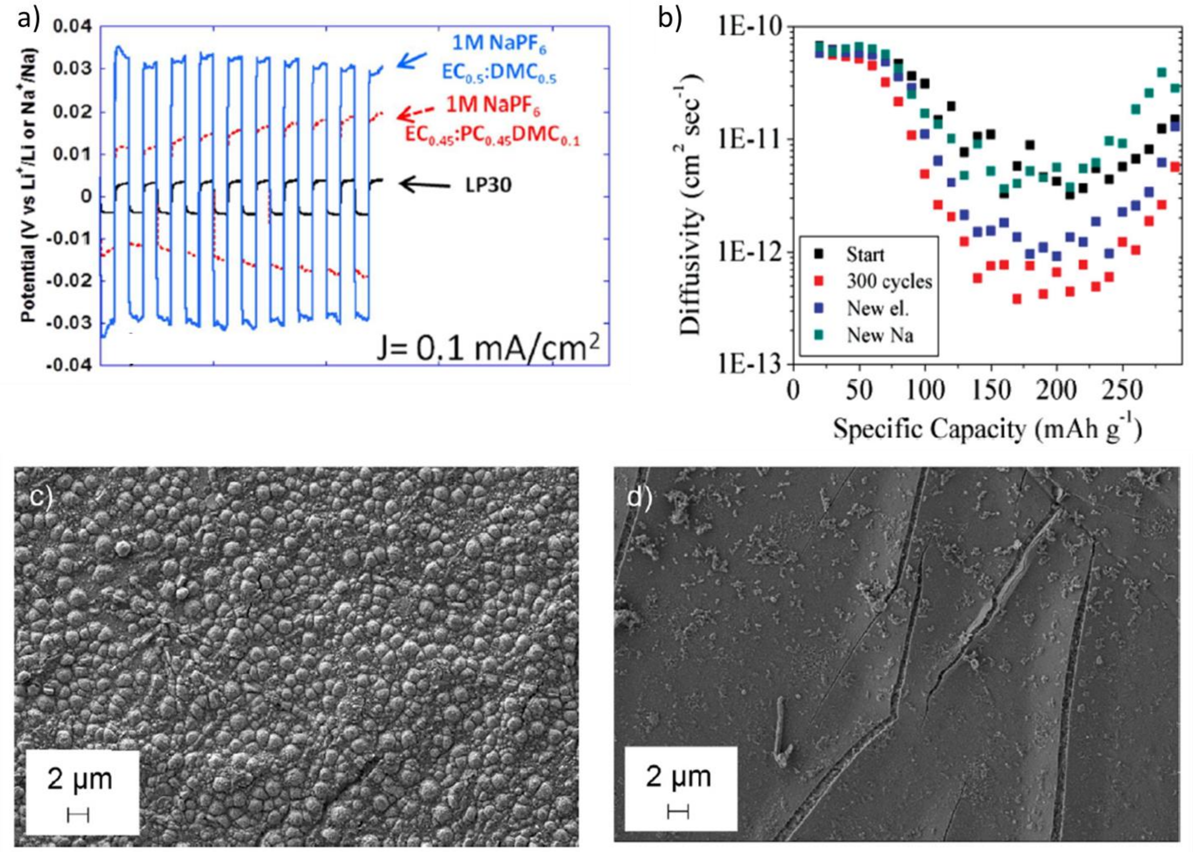

Figure 37: a) Large overpotentials of Na–Na symmetrical cells in carbonate-based electrolyte. Reprinted under the terms of CC BY-NC-ND 4.0 DEED licence [309]*, Copyright 2015, the authors, Published by IOPscience, b) diffusivity values with the fresh Na metal electrode. Reprinted with the permission from* [310]*. Copyright 2016, John Wiley & Sons, c) surface of the Na metal electrode after the 1st cycle and d) surface of the Na metal electrode after the 16th cycle Reprinted with permission from* [311]*, Copyright 2020, Elsevier.*

Bommier *et al.* [310] studied the effect of cell component degradation after prolonged cycling. Upon GITT measurements, they observed that the diffusivity values almost completely recovered when a fresh Na counter electrode was introduced (Figure 37.b). Moreover, 95% of the starting capacity was also achieved. From this, they concluded that the capacity fading was not due to the hard carbon electrodes. Finally, they soaked the Na metal in a carbonate-based electrolyte for three months and afterwards performed Fourier transform infrared spectroscopy (FTIR). They observed that the SEI formed without electrochemical cycling, showing the instability of Na metal electrodes in conventional carbonate electrolytes.

Mandl et al. [311] studied the evolution of the SEI formed on the Na metal surface throughout cycling. They observed the disappearance of different compounds over the first five cycles of *ex situ* XPS measurements. This was additionally corroborated with SEM imaging—spherical particles were observed on the surface after the first cycle (Figure 37.c) and were not observed in the subsequent cycles (Figure 37.d). The observed changes in morphology and surface chemistry indicate the formation of an unstable SEI.

Computational simulations of SEI formation have also been performed to support the experimental data and better understand its formation mechanism. Takenaka *et al.* [312] used a hybrid Monte Carlo (MC)/molecular dynamic (MC) method or the so-called Red moon method to simulate SEI formation at a carbon anode in an electrolyte with and without the addition of FEC (Figure 38). They observed that the FEC electrolyte forms a smoother and thinner SEI layer (3.9 nm compared to 5.7 nm without FEC). The SEI layer is also more compact and dense, preventing solvent molecules from reaching the carbon surface and effectively suppressing electrolyte decomposition. They concluded that the effect of FEC can be described by the modification of elementary chemical reaction processes during SEI formation and the suppression of unstable film growth. Continuing the work from Takenaka, Bouibes *et al.* [312] studied the effect of the amount of FEC added to the electrolyte. The red moon method showed increased SEI structural stability when a small amount of FEC was added via the reduction of dissolved reaction products into the bulk electrolyte. By increasing the FEC amount, the film growth became more unstable due to the suppression of organic dimer formation. Yildirim *et al.* [313] performed DFT calculations of the ion diffusion characteristics of LiF and NaF. The calculations showed high diffusion barriers for both compounds, explaining the kinetic limitations affecting the rate performance of batteries. Additionally, the ionic conductivity of NaF is several orders of magnitude lower than that of LiF. Nevertheless, the conductivities of both LiF and NaF are significantly lower than that of Li_2CO_3, highlighting that various SEI components present different conductivities. Ionic conductivity values of Na_2CO_3 could not be obtained from the literature. The high diffusion barriers obtained from DFT calculations of the ion diffusion characteristics of different SEI components were further corroborated by Soto et al. [298].

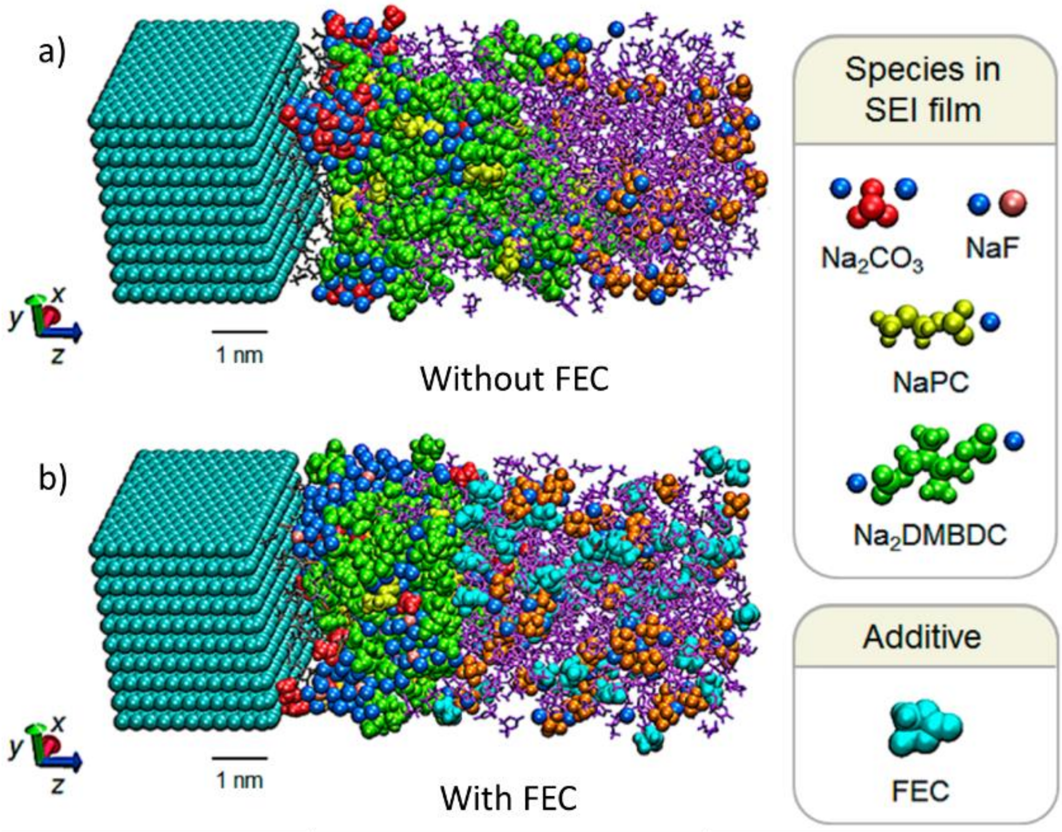

Figure 38: Computational simulation of SEI film formation on a carbon anode surface in a $NaPF_6$-PC electrolyte: a) without FEC and b) with FEC. Reprinted with permission from [312]*, Copyright 2018, American Chemical Society.*

Enabling swift Na^+ ions transport and ensuring stability of the electrode/electrolyte interface are key considerations of electrolyte design in NIBs. The formation of a stable SEI relies on the precise compatibility of electrolyte and electrode materials. The choice of solvents, additives, and electrode components plays a pivotal role in determining the phase interface's stability. Components such as solvents, additives, and electrode constituents significantly influence the electrochemical performance of HC, such as iCE, rate performance, cycling stability, and safety. However, conventional electrolytes suffer from drawbacks like high volatility, flammability, a limited electrochemical window, susceptibility to moisture and temperature, and safety concerns. Thus, current battery research emphasizes the identification of optimal electrolyte formulations to mitigate interface reactions and simultaneously enhance cell performance and safety [300].

Optimal electrolyte characteristics in battery systems include: (i) high ionic conductivity, (ii) a wide electrochemical window, and (iii) non-reactivity with cell components. The adoption of ethylene carbonate in electrolytes emerges as a favored approach to enhance the overall conductivity of solvent mixtures, resulting in batteries exhibiting enhanced electrochemical performance. A comprehensive review of the literature underscores the prevalence of ethylene carbonate in electrolytes, utilized in binary or ternary mixtures with other solvents [314].

The prospect of conducting a meta-analysis, consolidating electrochemical performance data from various papers into a broader study on electrolytes, faces challenges. Parameters such as the specific HC material used, the selection of electrolyte, and variations in electrochemical characterization protocols differ substantially across different research papers, posing significant challenges to achieving a comprehensive analysis [307].

While uncertainties persist regarding the ideal electrolyte characteristics, a handful of studies have attempted to elucidate this area. One noteworthy early exploration into electrolyte selection was conducted by Ponrouch et al. in 2012 [304], encompassing a diverse range of solvents. Through systematic assessments of parameters such as potential windows, thermal stability, and cycling stability, the researchers found that EC:PC emerged as a favorable electrolyte solvent (Figure 39.a). Interestingly, the choice of $NaClO_4$ or $NaPF_6$ as an electrolyte salt made little difference (Figure 39.b). The authors further fine-tuned the choice of an optimal solvent to $EC_{0.45}$:$PC_{0.45}$:$DMC_{0.1}$, complemented by a Na salt (Figure 39.c). According to their findings, this ternary mixture exhibited high ionic conductivity, minimized ion pairing, low viscosity, and most notably, facilitated the formation of a well-suited solid electrolyte interface (SEI) layer [315].

The abovementioned choice of electrolyte and the subsequent SEI formation strongly influence some key electrochemical properties of hard carbons such as rate capability, cycling stability and self-discharge.

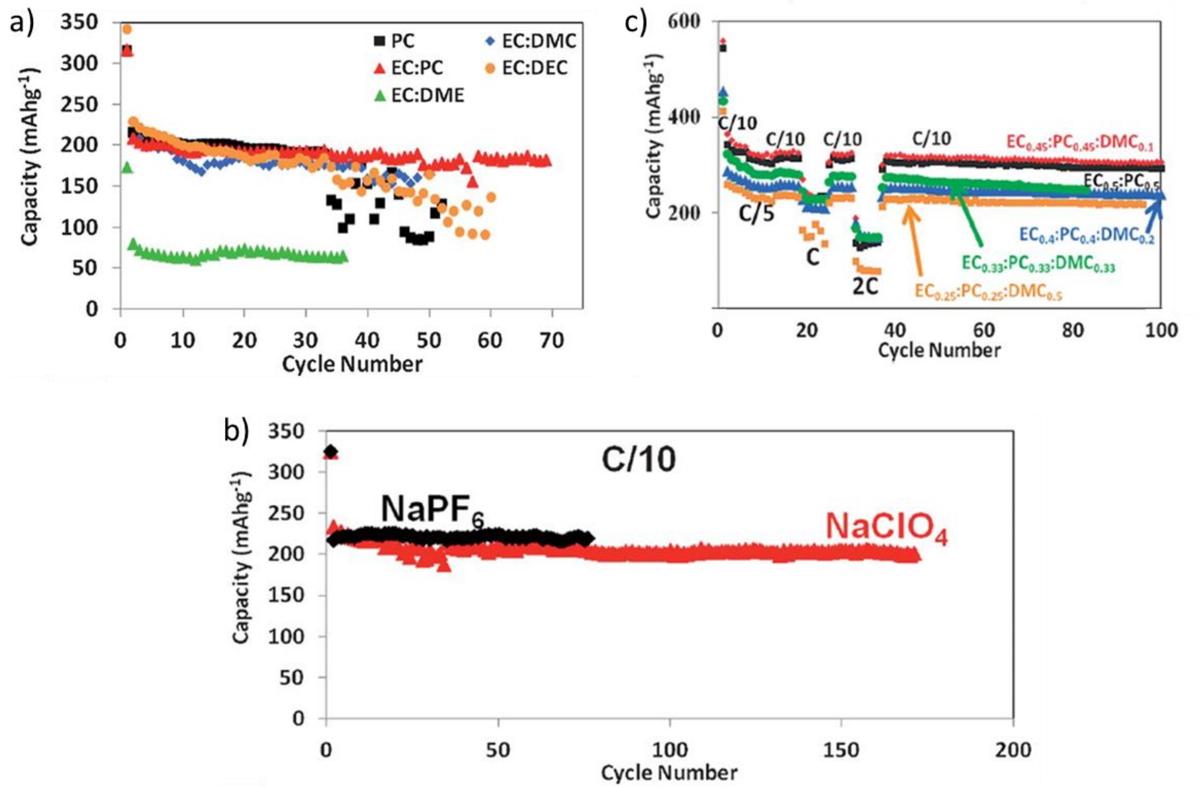

Figure 39: a) Cycling stability of HC electrodes in 1M NaClO$_4$ and various solvent mixtures. Reprinted with permission from[304]. Copyright 2012, John Wiley and Sons; b) Rate capability of HC electrodes using different electrolytes. Reprinted with permission from[315] Copyright 2013, John Wiley and Sons; and c) Cycling stability of HC electrodes with 1M NaPF$_6$ and 1M NaClO$_4$ in EC:PC based electrolytes. Reprinted with permission from [304]. Copyright 2012, John Wiley and Sons.

In general, HCs do not achieve satisfactory rate capabilities as evident from Figure 39.c. The subpar rate performance (compared to graphite in LIBs) is ascribed to a substantial reduction in plateau capacity under high current densities, where elevated overpotentials compel the batteries to reach the cut-off voltage prematurely before achieving full sodiation. As discussed earlier, the plateau capacity stems from either the intercalation or the pore-filling mechanism, both intricately governed by the diffusion process of Na$^+$ ions. The larger size of Na$^+$ ions hinders the kinetic process, leading to slower diffusion, thereby adversely affecting the rate performance of HCs [275, 316]. Additionally, the transport properties of Na$^+$ ions through the SEI are heavily contingent on the ionic conductivity of the formed SEI. The ionic conductivity is further dependent on the thickness and composition of the SEI, both properties closely linked to the chosen electrolyte [317].

Concurrently, the cycling stability of HC materials proves to be challenging, particularly for carbons with a high plateau capacity [318]. The capacity loss observed in the charge/discharge cycle does not arise from the irreversible destruction of the microstructure, given the tightly cross-linked internal structure of HC. Research by Hu et al. [67]. demonstrated that the capacity is restored upon the renewal of the electrolytes. Therefore, the cycling stability of HC is predominantly influenced by the stability of the electrolyte/electrode interface, closely tied to the composition of the electrolytes [317]. The instability of the SEI can result in continuous electrolyte decomposition, leading to a pronounced capacity loss during cycling. SEI instability arises from the decomposition of Na salt and solvents at low voltage, generating a highly soluble and unstable organic-rich SEI layer[319]. Furthermore, high dissolution rates of the SEI contribute to pronounced self-discharge of the cell [306,297].The research performed on SEI formation in Na-ion batteries is still scarce compared to Li-ion batteries, limiting our understanding of the interfacial processes taking place during cell operation. An in-depth understanding of the effect of individual SEI components is crucial for designing novel electrolytes to prevent dissolution and cracking of the SEI layer, and improve rate performance and cycling stability.

6 HC full cell test performance

6.1 HC full cell test performance

The electrochemical characterization of hard carbon is first carried out in a coin cell (versus Na metal) at low current rates permitting full sodiation/desodiation. Identifying the hard carbon's first sodiation capacity and the reversible capacity provides preliminary insights to establish an adequately balanced full cell.

After mounting the full cell, which comprises a cathode as the working electrode and hard carbon as the counter electrode, electrode–electrolyte interphases are formed (Figure 38). The solid electrolyte interface (SEI) forms at the anode of Na-ion batteries, and the cathode–electrolyte interface (CEI) forms at the cathode of Na-ion batteries (formation cycles) and is critical in maintaining the long-term cycling/lifetime of the full cell. The hard carbon performance is crucial since the applied current during formation can vary from that used during capacity characterization. This means that the hard carbon kinetics and rate capability are detrimental to this step.

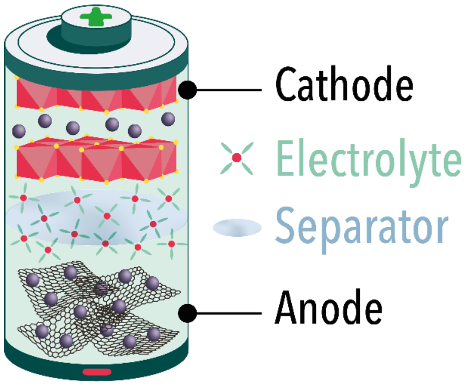

Figure 38: Schematic representation of a Na-ion battery full cell showing the main components, as proposed by the authors of this work.

Several hard carbons can perform well in coin cells *vs.* Na-metal (as in specific capacity and irreversible capacity loss). However, they can fail to provide proper electrochemical performance in full cell configurations. The latter can be due to the poor rate capability performance of the hard carbon, the heat generation as it passes through resistive elements induced by the SEI and the hard carbon itself, the instability of the SEI (leading to its ongoing formation), the poor mechanical adhesion of the electrode (due to the nature of the hard carbon), and finally a poor long-term cyclability due to plating and the collapsing of the hard carbon structure and its pores.

Engineering hard carbon electrodes as a function of the application required can provide solutions for high-power density and others for high-energy density. In addition, the electrode porosity, calendering and mechanical adhesion can ensure different application requirements.

Table 6 illustrates the performance of different hard carbons synthesized from different precursors at a lab-scale or commercial level with varying cathode technologies available, which are well reported. The reversible capacity of the hard carbon was identified versus Na-metal. However, in a full cell with various cathode active materials, the irreversible capacity differs, and this is mainly attributed to factors, including the nature of the electrolyte and its additives and hence the SEI layer, the rate of formation of the interphases, the temperature of formation, and the balancing of the cell.

As noticed in Table 6, the majority of HC characterization was carried out in coin cells (half-cells versus Na-metal) and then balanced with a counter electrode for full cell testing (2 or 3 electrodes). The coin cell testing can be carried out at low current rates or by adding a constant voltage step at low potential (HC plateau) to ensure full sodiation. Due to the coin cell's intrinsic high resistance, high current rates would lead to a high polarization and undervaluation of the hard carbon specific capacity.

The battery format plays a significant role in the overall cell resistance, and moving from coin cells to pouch cells to cylindrical cells and prismatic cells, this overall resistance decreases respectively. The resistance decrease is related to the battery format rather than the active materials used. Hence, the HC-specific capacity can be attained in all battery formats if the right current rate/cycling program is applied.

Finally, the various cathode active materials reported in Table 6 are divided into three sections: polyanionic cathode materials, layered/transition metal oxide cathode materials, and Prussian blue analogues—this variety of cathode materials have different specific capacities, average voltages, densities, and cycling stabilities. In Section 2, we discuss different company strategies that principally use other cathode materials for diverse applications.

Table 6. Hard carbon anode material testing with varying cathode technologies, electrolytes and current rates

Hard Carbon Source	**HC *vs.* Na-metal Reversible capacity mAh g^{-1}**	**Cathode Active Material**	**Cathode *vs.* Na-metal Reversible capacity mAh g^{-1}**	**Electrolyte Composition**	**Current Rate**	**Full cell iCE**	**Format tested**
Polyanionic cathodes							
Commercial HC	250	$Na_3V_2(PO_4)_2F_3$	128	EC_{50}/DMC_{50} + 1 M $NaPF_6$	C/10	83% [320]	Coin cells
Commercial HC	250	$Na_3V_2(PO_4)_2F_3$	128	Diglyme + 1 M $NaPF_6$	C/10	77% [320]	Coin cells
Naiades HC	300	$Na_3V_2(PO_4)_2F_3$	129	$EC_{49.25}/DMC_{49.25}/FEC_{1.5}$ + 1 M $NaPF_6$	C/10	79% [321]	Coin cells Cylindrical cells
Naiades HC	300	$Na_3V_2(PO_4)_2F_3$	~130	EC_{50}/DMC_{50} + 1 M $NaPF_6$	n.a.	77% [322]	Coin cells Cylindrical cells
Commercial HC	257	$Na_3V_2(PO_4)_2F_3$	128	EC_{49}/DMC_{49} + 1%FEC + 1 M $NaPF_6$	C/10	78% [323]	Coin cells
Biosourced HC*	300	$Na_3V_2(PO_4)_2F_3$	128	TIAMAT Electrolyte	n.a.	80%	Coin cells Pouch cells Cylindrical cells Prismatic cells
Phenolic resin HCS 1500	294	$Na_3V_2(PO_4)_2F_3$	124	EC_{50}/DMC_{50} + 1 M $NaPF_6$	C/5	86% [98]	Coin cells
Tannin-polyphenols HCMG1600	313	$Na_3V_2(PO_4)_2F_3$	120	EC_{50}/DMC_{50} + 1 M $NaPF_6$	C/5	80% [115]	Coin cells
Pyroprotein HCGs-2000	300	$Na_{1.5}VPO_{4.8}F_{0.7}$	100	DEGDME + 1 M $NaPF_6$	0.1 A/g	88% [324]	Coin cells
Layered/transition metal oxides cathodes							
Aekyung Petrochemical HC	310	$NaNi_{0.45}Zn_{0.05}Mn_{0.4}Ti_{0.1}O_2/C$	180	EC_{50}/DMC_{50} + 1 M $NaPF_6$	C/10	n.a. [325]	Coin cells
Biosourced HC*	300	O3- $Na_aNi_{1-x-y-z}M1_xM2_yM3_zO_2$	180	EC_{50}/DMC_{50} + 1 M $NaPF_6$	n.a.	85%	Coin cells Pouch cells Cylindrical cells Prismatic cells
Faradion HC	280	O3/P2 $Na_aNi_{1-x-yz}M1_xM2_yM3_zO_2$	157	Faradion Electrolyte	n.a.	91% [326]	Pouch cells
Sucrose-HCS1600	300	$Na_{2/3}Ni_{1/3}Mn_{2/3}O_2$	200	EC_{50}/DMC_{50} + 1 M $NaClO_4$	C/10	76% [76]	Coin cells
Cotton	315	O3-$Na_{0.9}(Cu_{0.22}Fe_{0.3}Mn_{0.48})O_2$	100 [9]	EC_{50}/DMC_{50} + 0.8 M $NaPF_6$	C/5	73% [153]	Coin cells
Poplar Wood PHC-1400	330	$Na(Cu_{1/9}Ni_{2/9}Fe_{1/3}Mn_{1/3})O_2$	118 mAh/g	EC_{50}/DMC_{50} + 1 M $NaPF_6$	C/10	75% [327]	Coin cells

Prussian Blue Analogues (PBAs)							
Kureha HC	260	$Na_{1.89}MnFe(CN)_6$	150	EC_{50}/DEC_{50} + 1 M $NaClO_4$	C/10	80% [328]	Coin cells
Kureha HC	260	$Na_{1.92}Fe_2(CN)_6$	155	EC_{50}/DEC_{50} + 1 M $NaPF_6$	10 mA/g	78% [329]	Coin cells
Kuranode HC	330	$Na_2Fe[Fe(CN)_6]$	169	$EC_{47.5}/DEC_{47.5}$ + 5% FEC + 1 M $NaClO_4$	C/10	Presodiated HC [330]	Swagelok cells
Shaddock Peels HC	280	$Na_2Fe_4[Fe(CN)_6]_3$	125	EC_{45}/DEC_{455} + 10% FEC + 1 M $NaClO_4$	2C	Presodiated HC [331]	Coin cells
*Commercial HC used by TIAMAT							

6.2 Applications of SIBs in real-life devices

Rechargeable batteries are omnipresent since they are the sole wireless energy providers in smartphones, laptops and other portable electronic devices, along with powering electric and hybrid electric vehicles (electric vehicles and hybrid electric vehicles) [332]. For SIBs, the abundance of materials is an unequivocal reason why sodium ions are attractive as charge carriers in rechargeable batteries for various applications. Furthermore, the main driver of the sodium-ion market is the increasing demand for clean energy with increasing greenhouse gas emissions worldwide.

The application of SIBs in real-life devices can be divided into two principal axes: stationary energy storage and transport applications. The stationary application's success results from the higher cost assurances provided by SIBs and the operation of the battery at extreme temperatures. The realization of SIBs in stationary energy storage is in response to several intrinsic weaknesses of SIBs when compared to lithium-ion batteries (LIBs); Na has three times the atomic weight of Li and has a 300 mV higher redox potential, so the energy density of Na-ion technology is at least 30% lower compared to that of Li-ion technology [333].

The never-ending increase in electricity demand and electrical energy storage (wind and solar photovoltaic power) is likely to drive a large part of the sodium-ion market (the projected stationary storage demand for solar and wind renewable energy by 2030 accounts for 50% of the total electricity generation in several countries) [334]. Stationary storage includes storage systems in industrial and residential environments and/or telecommunications networks and data centre power supplies (backup energy), as shown in Figure 39.

Figure 39: A 1 MWh SIB-based energy storage system put into operation by HiNa Battery Technology Co., Ltd.. Reprinted with the permission from [335]*, Copyright HiNa Battery Technology Co., Ltd.*

The reasonably medium charge rates required for stationary applications (residential, commercial, industrial), principally as emergency power supplies and off-grid power consumption, are governed mainly through high-energy density cathode materials (layered oxide cathode materials [9]) or long-cycle life and low-cost cathode materials (Prussian Blue (PB)) [336]. The sodium-ion prototyping and fabrication of mobile/automotive or stationary energy storage take similar formats to that of lithium-ion batteries (pouch, cylindrical and prismatic cells), as shown in Figure 40.

Figure 40: High-energy density Na-ion batteries provided by Faradion (pouch, prismatic and cylindrical formats). Reprinted with permission from [337]. Copyrights Faradion.

Furthermore, SIBs show possible automotive applications and can govern several transport applications. High-power density cathode materials (polyanionic cathode materials [315]) and a long cycle life ensure automotive applications. Furthermore, high-power SIBs can be assembled in a 48 V battery pack for mild hybrid vehicle (MHEV) applications or used in nonautomotive applications, such as power tools (cylindrical cells), as illustrated in Figure 41.

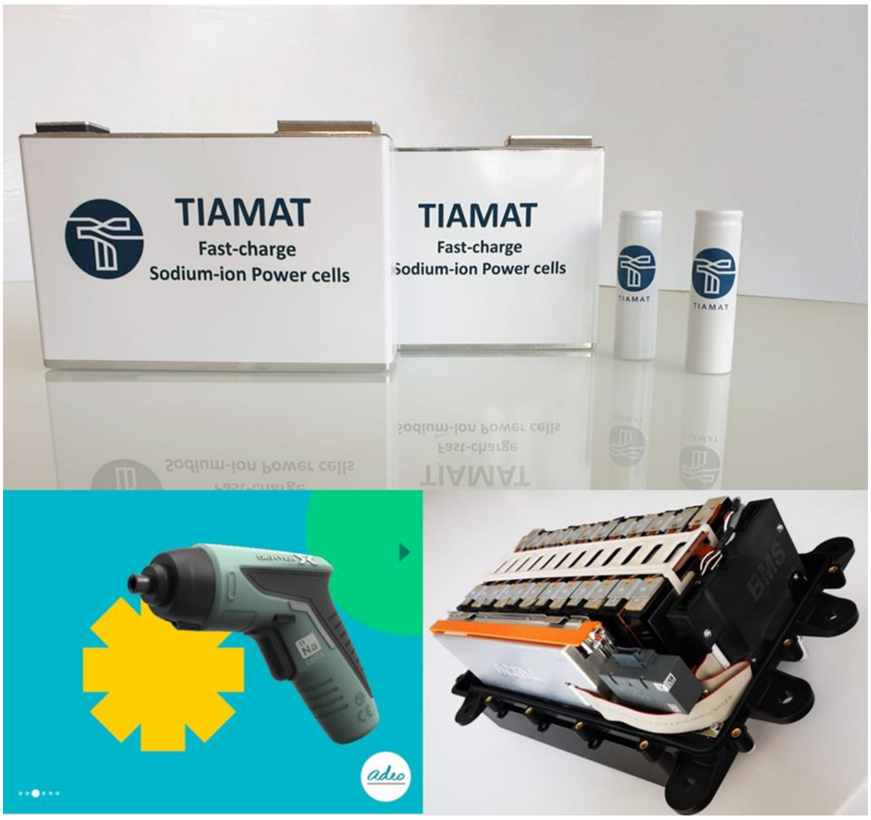

Figure 41: High-power density Na-ion batteries are provided by TIAMAT (prismatic and cylindrical formats) implemented in power tools and 48 V battery packs. Reproduce with the permission from [338,339], Copyright Tiamat.

Other solutions can be provided by combining SIBs and LIBs, such as those announced by Contemporary Amperex Technology Co., Ltd. (CATL) (Figure 42). The former is an AB battery pack solution that integrates sodium-ion and lithium-ion cells into one pack. The cathode material used and presented by CATL is a Prussian white cathode material [340].

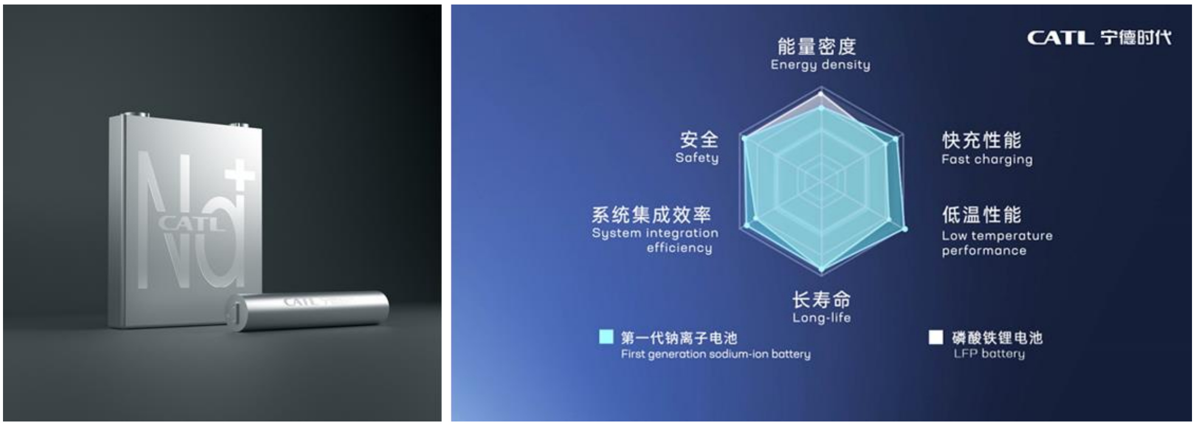

Figure 42: Generation 1 SIB provided by CATL (prismatic and cylindrical formats). Reprinted from [340]. Copyrights CATL.

Finally, and for the first time, sodium-ion batteries in electric vehicles (Sehol E10X test vehicles) were revealed in China by HiNA Battery Technology Co., Ltd. (February 2022). The test vehicle (Figure 43) is equipped with a battery pack with a capacity of 25 kWh and an energy density of 120 Wh kg^{-1}. This model has a range of 252 km and supports fast charging from 3C to 4C. The battery pack uses cells with an energy density of 140 Wh kg^{-1} [341, 342].

Figure 43: First-time sodium-ion batteries in electric vehicles (Sehol E10X test vehicle) by HiNa Battery Technology Co., Ltd.. Reprinted with the permission from[341]. Copyright HiNa Battery Technology Co., Ltd. and Sehol.

6.3 History of SIB enterprises

Several enterprises are producing HC on a large scale using different precursors. As this topic was well reviewed recently in the literature [37], we focus the last part of this review on the SIB enterprises. In this part a short review a SIB is presented. Several SIB enterprises have been established over time; some are spin-offs from universities and academic work, some are companies developing only SIBs, and others are already LIB producers. Some enterprises declared bankruptcy and sold/gave up their patents, while others are still active.

1- Aquion Energy (2008)

Aquion Energy was established in 2008 as a spin-off from Carnegie Mellon University. Their battery was based on a sodium titanium phosphate anode, a manganese dioxide cathode, and a sodium perchlorate electrolyte. The company filed for bankruptcy in 2017 after receiving government and private loans. That property was sold to the Chinese manufacturer Julyine-Titans, who gave up most of their Aquion patents.

2- Faradion (2011)

Faradion was established in 2011 by Dr Jerry Barker, Dr Chris Wright and Ashwin Kumaraswamy. Faradion is a subsidiary of Reliance Industries, India. Faradion's SIB cell design uses a hard carbon anode and a lamellar oxide cathode with a liquid electrolyte. The company's pouch cells have energy densities comparable to commercial lithium-ion batteries (160 Wh/kg at the cell level) with a rate performance up to 3C. The SIB claimed to have 1,000 cycles (80% depth of discharge). In 2021, Faradion announced a collaboration and licensing deal with AMTE Power [337]. On December 5, 2022, Farradion installed the first nationwide sodium-ion battery in New South Wales, Australia [343].

3- TIAMAT (2012)

TIAMAT is a spin-off from the sodium-ion task force of the CNRS/CEA established in 2012 and its H2020-EU project called NAIADES. The scientific board of TIAMAT includes leaders in academic research on energy storage materials (Professor Jean Marie Tarascon, Professor Christian Masquilier, Professor Patrice Simon, Dr Laurence Croguinec, and Dr Mathieu Morcrette). Two-generation SIBs were developed at TIAMAT in different formats (18650 cylindrical format, prismatic cells, and pouch cells). Generation 1 cathode materials are based on polyanion materials with achieved energy densities of 100 Wh/kg to 120 Wh/kg [338]. The high power density and long lifetime cyclability (5000 cycles to 80% and 10000 cycles to 70% capacity at high current density charging in less than 30 min and fast discharge in 12 min), along with battery safety, are breakthrough technologies behind SIBs. The safe transport of sodium-ion batteries under 0 V conditions eliminates the risk of commercial transport of such batteries. Generation 2 cathode materials are based on lamellar oxide materials with energy densities reaching 140 Wh/kg and are projected to increase upon further development to 180 Wh/kg. Generation 2 cathode materials were first introduced in the H2020-EU project, NAIMA, in 2022 [344].

4- Natron Energy (2012)

A Stanford University spin-off, Natron Energy, uses an analogue of Prussian blue for both the cathode and anode with an aqueous electrolyte. Natron Energy claims to be the world's leading provider of high-performance, long-life, cost-effective Prussian blue sodium-ion battery solutions for critical power and industrial applications, material handling equipment for centres and electric UPS systems. In 2020, Natron announced the world's first sodium-ion battery as it obtained its UL listing for its battery products in 1973 and began commercial shipments to customers in the data centre, forklift, and EV quick charger markets [345].

5- HiNA Battery Technology Co. Ltd (2017)

HiNa Battery Technology Co., Ltd. was founded in 2017 and was a spin-off of the Chinese Academy of Sciences (CAS). It leverages research conducted by Professor Hu Yong-Sheng's group at the CAS Institute of Physics. HiNa's SIB products are based on a unique copper (Cu)-based oxide chemistry and anthracite-derived soft carbon as the cathode and anode materials [346]. In 2014, the research team at HiNa first discovered the electrochemical activity of the Cu^{3+}/Cu^{2+} redox couple in a P2-phase $Na_{0.68}Cu_{0.34}Mn_{0.66}O_2$ material [347]. As a result, they can provide an energy density of 120 Wh/kg. In 2022, the MWh SIB-based energy storage system was put into operation by HiNa Battery Technology.

6- Altris AB (2017)

Altris AB is a spin-off of Angström Advanced Battery Center and Prof. Kristina Edstrom of Uppsala University in Sweden. The use of Prussian blue analogues as anode and cathode materials with nonaqueous electrolytes distinguishes the technology of this enterprise. The raw material availability, safety and cyclability are the main advantages of Altris batteries and counterbalance the low-energy density of these SIBs.

7- Contemporary Amperex Technology Co., Ltd. (2021)

The Contemporary Amperex Technology Co., Ltd. (CATL) Chinese battery maker announced in 2021 that it would launch a sodium-ion-based battery by 2023. A Prussian white analogue is used for the cathode, and carbon is used for the anode [340]. An AB battery pack solution can integrate sodium-ion cells and lithium-ion cells into one pack.

Conclusions and perspectives

Na-ion batteries have gained significant popularity in the last decade. Research in this field has intensified mainly because of the necessity to find alternatives to current LIB technology. Many critical battery components and their uneven distribution along with geopolitical tensions contribute to the quest to find abundant, long-lasting, and cost-effective energy storage systems. SIBs perfectly meet these criteria, and their development has known an accelerated tendency. Hard carbons, which can be obtained from various precursors such as biomass, biopolymers, and synthetic polymers, have become the most appealing anode materials for these batteries. The properties of HC are closely related to the parent precursors but are also significantly affected by the synthesis conditions (pyrolysis temperature, gas flow rate, synthesis pathway, etc.). Therefore, the structure (graphitic interlayer space, defects, and graphitic domain arrangement), the porosity (specific surface area, pore size and volume), the morphology (particle shape and size), and surface chemistry (nature and amount of functional groups) can be tuned by the synthesis conditions. In general, it was observed that the HC properties are precursor dependent; however, biomass results in materials with higher porosity, interlayer space, and surface chemistry, synthetic polymer leads to lower values of these properties, while biopolymers fall in between these two categories. In addition, the pyrolysis temperature affects carbon properties in a similar manner, and the values of many properties typically decrease with increasing temperature. Some exceptions are to be noted, such as the increase of closed porosity with the pyrolysis temperature. Several syntheses - properties dependent relationships - were shown in this direction in this review.

The electrochemical performance of HC materials (initial Coulombic efficiency, capacity, and stability) was found to be strongly impacted by the HC properties. For example, the iCE is strongly related to the specific surface area, surface functionalities, and inorganic impurities. All these properties lead to electrolyte decomposition, the formation of the SEI layer, and low values of iCE. Therefore, the best iCE obtained is linked to materials that present limited porosity and chemistry. The composition and properties of the SEI layer are not yet fully understood; however, the formation of inorganic and organic species is more likely to govern the carbon/electrolyte interphase. With regard to the storage capacity, several works demonstrated that the mechanisms are connected with the adsorption-insertion phenomena of Na^+ on the carbon surface and in the structure. Although these mechanisms are still far from being fully understood, the insertion between the graphitic interlayer space and the adsorption on carbon defects are mostly contributing to Na-storage.

Based on the knowledge gained from all these literature studies, an "ideal" HC should have a low specific surface area (< 10 m g^{-1}), convenient graphitic interlayer space (3.7 – 3.8 Å) and no inorganic impurities, to ensure low iCE and high capacity and stability. However, other properties such as defects, heteroatoms and closed pores can be tuned to improve HC performance, but their role could not be precisely established/quantified yet.

In addition to the carbon properties, the electrochemical conditions (electrode formulation, electrolyte/solvent type, and testing conditions) play an important role in the performance. The lack of standardisation of such tests makes the comparison between the data in the literature difficult. Despite this inconvenience, this work presented several interesting property-performance correlations, which allow the readers to have a general overview in this direction. The reversible capacity of HC is rather high (> 300 mA h^{-1}), approaching that of graphite in LIBs, while the iCE was progressively improved (max. 92%), it can still be enhanced by increasing the purity of HC, by selecting convenient electrolytes and electrochemical testing conditions. The main challenges to address are the stability and rate capability of HC. As many tests are done versus metallic Na, performance of HC in full cells are more than required. We reviewed some of them herein, and moreover, the history of SIBs prototypes and enterprises was as well described. As the SIB market begins to develop, this will induce more research and development on hard carbon, electrolytes, and cathodes, which will favour the implementation of renewable and abundant materials, low cost SIB devices, and low CO_2 emission applications.

Acknowledgements

This work was financially supported by the European Union's Horizon 2020 Program (project NAIMA, call: LC-BAT-02, Contract no. 875629), Slovenian Research and Innovation Agency (ARIS) under research program P2-0423 and project N2-0266, and French National Research Agency (STORE-EX Labex Project ANR-10-LABX-76-01) for financial support. We acknowledge Julia Coffre for the help provided with the design of the figures, and Omar Rahmouni for the literature data base collection.

Conflict of interest

The authors declare no conflict of interest

Authors contributions

CMG conceptualization, project administration, funding acquisition, supervision, writing-original draft, writing review & editing.

AB investigation, supervision, writing-original draft, writing, review & editing.

BR data curation, formal analysis, resources, writing review & editing.

HEM data curation, formal analysis, writing-original draft, writing – review & editing.

AV investigation, writing-original draft, writing review & editing;

BT investigation, writing-original draft, writing review & editing;

LS data curation, formal analysis, funding acquisition, writing review & editing;

JM data curation, writing review & editing.

RD investigation, writing review & editing, funding acquisition

Author Biography

Dr. Camélia MATEI GHIMBEU is a Research Director at the Material Science Institute in Mulhouse (IS2M), CNRS, France. She is the head of "Carbon and Hybrid Materials" group at IS2M and member of French network of Electrochemical Storage of Energy (RS2E). She received her Ph.D. in 2007 from the University of Metz, France. Her research interests focus on the design of new carbon-based materials with controlled properties, their multiscale characterization, and their application in energy storage and environmental applications. For more than ten years, she has greatly contributed to the field of hard carbon materials for sodium ion batteries.

Dr. Adrian BEDA is currently a Research Engineer at Mulhouse Materials Science Institute (IS2M), in France, involved in several national and international projects. After graduating from his engineering studies, he continued his academic track with a Master in Science from the University of Poitiers, France, and a PhD in Material Chemistry from the University of Haute-Alsace, France. At the moment, his main research interest focuses on developing and optimizing new hard carbon anode materials for sodium-ion batteries.

Eng. Bénédicte RETY is a research engineer at the Mulhouse Materials Science Institute (IS2M), a CNRS-University mixed research unit in France. She is part of the French Research network on Electrochemical Energy Storage (RS2E). She obtained her Master's degree in Materials Science in 2015 from the University of Haute-Alsace, France. She is responsible of a TPD-MS (Thermodesorption coupled with Mass Spectrometry) and a thermal treatments platform. She works on different projects involving the synthesis, activation, functionalization and characterization of carbon materials and its applications in electrochemical energy storage, catalysis and depollution.

Dr. Hamza EL MAROUAZI is a post-doctoral researcher at the Research Laboratory *LHEEA* at Ecole Centrale de Nantes, France. In 2021, he obtained his PhD in Materials Chemistry and Physics from the University of Strasbourg, France. In 2022, he joined the Mulhouse Materials Science Institute (IS2M-France) as a post-doctoral researcher on carbon materials for Na-ion batteries in Dr. Camélia Ghimbeu's group. He is focusing on the development of materials for green energy application (solar cells, photocatalysis, hydrogen production, photo-reduction of carbon dioxide, fuel cells, energy storage and biomass valorisation).

Dr. Alen VIZINTIN is affiliated with the National Institute of Chemistry as a researcher. His research interests are in material science and electrochemistry. He has a particular emphasis on the study of carbon-based materials and nanomaterials, and has expertise in a range of characterization techniques in *operando*, *in situ*, and *ex situ* mode. In the last years his focus was on (a) carbonaceous materials synthesis and surface functionalization for Na-ion batteries, (b) electrochemistry of Na-ion and metal-S batteries, (c) studying the reaction mechanism in Na-ion, metal-S and organic batteries with *operando* spectroscopic characterization techniques.

Dr. Blaž TRATNIK is a research associate at the National Institute of Chemistry. His main research focus is the pyrolysis process and tailoring of physico-chemical properties of biomass-derived non-graphitizable carbons for Na-ion batteries. He has also dedicated his attention to conducting research on the reaction mechanisms in Na-ion batteries using various characterization techniques and exploring the electrochemical insertion of sodium into non-graphitizable carbons for Na-ion batteries.

Dr. Loic SIMONIN has been working as a research scientist and project manager in CEA-LITEN for 15 years towards the development of new cathode and anode materials for both Li-ion and Na-ion batteries. He has been working as project leader in many project involving industrial and academic partners. He has been the coordinator of a H2020 project NAIADES (grant N° 646433) which lead to the foundation of the Na-ion cells manufacturing RS2E spin-off company TIAMAT.

Dr. Julie MICHEL is a PhD student at CEA Grenoble, France, and UNESCO-IHE Delft, the Netherlands; she obtained her master degree at the Nationale Graduate School of Chemistry of Montpellier (ENSCM), France, in circular economy and biomass valorisation. Her research is focused on biomass-based carbon materials for energy storage application. During the last three years, she devoted her work to hard carbon synthesis for Na-ion battery negative electrode. In particular, to understand the fate of inorganics during biomass hydrothermal carbonisation and pyrolysis to provide the materials with the best performance.

Dr. John ABOU-RJEILY is the NAIMA H2020 European Project Coordinator and R&D Scientist at TIAMAT in France. In 2019, he was awarded a Ph.D. in Physical Chemistry and Chemistry of Materials by the University of Tours in France where he was later recruited for a postdoc fellow. At TIAMAT, he is principally working on hard carbon engineering, doping, benchmarking, and industrial collaborations with international companies. In NAIMA, his work included prototyping industrial Na-ion batteries, electrolyte optimisation, electrochemical cell testing, postmortem analysis and Coordination.

Prof. Robert DOMINKO is a Research Professor at the National Institute of Chemistry and a Professor at the University of Ljubljana. He is the head of the battery group at the National Institute of Chemistry and deputy director of the ALISTORE-ERI network. His current research interests are focused on post Li-ion batteries and the implementation of smart functionalities in battery cells. He is strongly connected with the Battery 2030+ initiative. He is a member of the Slovenian Academy of Engineering.

References

1. The global electric vehicle market in 2021: statistics & forecasts, https://www.virta.global/global-electric-vehicle-market, (accessed 30/03/2021, 2021).
2. T. Khokhar and H. Kashiwase, The future of the world's population in 4 charts, https://blogs.worldbank.org/opendata/future-world-s-population-4-charts, (accessed 05/04/2021, 2021).
3. R. Alhindawi, Y. A. Nahleh, A. Kumar and N. Shiwakoti, *Sustainability*, 2020, **12**, 9152.
4. A. Hoekstra, *Joule*, 2019, **3**, 1412-1414.
5. Batteries on wheels: the role of battery electric cars in the EU power system and beyond https://www.transportenvironment.org/sites/te/files/publications/2019_06_Element_Energy_Batteries_on_wheels_Public_report.pdf, (accessed 05/04/2021, 2021).
6. R. Eisenberg, *Acs Energy Letters*, 2018, **3**, 1521-1522.
7. S. Lu and J. Frith, Will the Real Lithium Demand Please Stand Up? Challenging the 1Mt-by-2025 Orthodoxy, https://about.bnef.com/blog/will-the-real-lithium-demand-please-stand-up-challenging-the-1mt-by-2025-orthodoxy, (accessed 16/03/2021, 2021).
8. T. C. Wanger, *Conservation Letters*, 2011, **4**, 202-206.
9. N. Yabuuchi, K. Kubota, M. Dahbi and S. Komaba, *Chemical Reviews*, 2014, **114**, 11636-11682.
10. J. L. Song, W. Y. Yan, H. B. Cao, Q. B. Song, H. Ding, Z. Lv, Y. Zhang and Z. Sun, *Journal of Cleaner Production*, 2019, **215**, 570-581.
11. G. Montgomery, Can metals supply keep up with electric vehicle demand? Battery raw materials could face supply crunch by mid-2020s, https://www.woodmac.com/news/opinion/can-metals-supply-keep-up-with-electric-vehicle-demand/, (accessed 16/03/2021, 2021).
12. L. Oliveira, M. Messagie, S. Rangaraju, J. Sanfelix, M. H. Rivas and J. Van Mierlo, *Journal of Cleaner Production*, 2015, **108**, 354-362.
13. J. C. Kelly, M. Wang, Q. Dai and O. Winjobi, *Resources Conservation and Recycling*, 2021, **174**.
14. G. Harper, R. Sommerville, E. Kendrick, L. Driscoll, P. Slater, R. Stolkin, A. Walton, P. Christensen, O. Heidrich, S. Lambert, A. Abbott, K. Ryder, L. Gaines and P. Anderson, *Nature*, 2019, **575**, 75–86.
15. M. Walter, M. V. Kovalenko and K. V. Kravchyk, *New Journal of Chemistry*, 2020, **44**, 1677-1683.
16. A. El Kharbachi, O. Zavorotynska, M. Latroche, F. Cuevas, V. Yartys and M. Fichtner, *Journal of Alloys and Compounds*, 2020, **817**, 153261.
17. G. G. Eshetu, S. Grugeon, H. Kim, S. Jeong, L. M. Wu, G. Gachot, S. Laruelle, M. Armand and S. Passerini, *Chemsuschem*, 2016, **9**, 462-471.
18. M. Dahbi, N. Yabuuchi, K. Kubota, K. Tokiwa and S. Komaba, *Phys Chem Chem Phys*, 2014, **16**, 15007-15028.
19. WO2016027082A1, 2016.
20. D. A. Stevens and J. R. Dahn, *Journal of The Electrochemical Society*, 2001, **148**, A803-A811.
21. Y. Liu, B. V. Merinov and W. A. Goddard, *Proceedings of the National Academy of Sciences*, 2016, **113**, 3735-3739.
22. H. Kim, J. Hong, Y. U. Park, J. Kim, I. Hwang and K. Kang, *Advanced Functional Materials*, 2015, **25**, 534-541.
23. E. R. Buiel, A. E. George and J. R. Dahn, *Carbon*, 1999, **37**, 1399-1407.
24. M. Dahbi, M. Kiso, K. Kubota, T. Horiba, T. Chafik, K. Hida, T. Matsuyama and S. Komaba, *Journal of Materials Chemistry A*, 2017, **5**, 9917-9928.
25. K. Wang, Y. Jin, S. Sun, Y. Huang, J. Peng, J. Luo, Q. Zhang, Y. Qiu, C. Fang and J. Han, *ACS Omega*, 2017, **2**, 1687-1695.
26. N. Zhang, Q. Liu, W. L. Chen, M. Wan, X. C. Li, L. L. Wang, L. H. Xue and W. X. Zhang, *Journal of Power Sources*, 2018, **378**, 331-337.

27. X. M. Zhu, X. Y. Jiang, X. L. Liu, L. F. Xiao and Y. L. Cao, *Green Energy & Environment*, 2017, **2**, 310-315.
28. C. Bommier, W. Luo, W.-Y. Gao, A. Greaney, S. Ma and X. Ji, *Carbon*, 2014, **76**, 165-174.
29. J. M. Conder, C. Vaulot, C. Marino, C. Villevieille and C. M. Ghimbeu, *ACS Applied Energy Materials*, 2019, **2**, 4841–4852.
30. C. Matei Ghimbeu, B. Zhang, A. Martinez de Yuso, B. Rety and J.-M. Tarascon, *Carbon*, 2019, **153**, 634-647.
31. V. Simone, A. Boulineau, A. de Geyer, D. Rouchon, L. Simonin and S. Martinet, *J Energy Chem*, 2016, **25**, 761-768.
32. A. Beda, P.-L. Taberna, P. Simon and C. Matei Ghimbeu, *Carbon*, 2018, **139**, 248-257.
33. Y. Li, L. Mu, Y.-S. Hu, H. Li, L. Chen and X. Huang, *Energy Storage Materials*, 2016, **2**, 139-145.
34. P.-Y. Zhao, B.-J. Yu, S. Sun, Y. Guo, Z.-Z. Chang, Q. Li and C.-Y. Wang, *Electrochimica Acta*, 2017, **232**, 348-356.
35. H. Liu, Z. Xu, Z. Guo, J. Feng, H. Li, T. Qiu and M. Titirici, *Philosophical Transactions of the Royal Society a-Mathematical Physical and Engineering Sciences*, 2021, **379**.
36. ESG of graphite: how do synthetic graphite and natural graphite compare?, https://source.benchmarkminerals.com/article/esg-of-graphite-how-do-synthetic-graphite-and-natural-graphite-compare, (accessed 23/01/2024, 2024).
37. H. T. Liu, M. Baumann, X. W. Dou, J. Klemens, L. Schneider, A. K. Wurba, M. Häringer, P. Scharfer, H. Ehrenberg, W. Schabel, J. Fleischer, N. von der Assen and M. Weil, *Journal of Energy Storage*, 2022, **56**, 105964.
38. G. Hasegawa, K. Kanamori, N. Kannari, J.-i. Ozaki, K. Nakanishi and T. Abe, *ChemElectroChem*, **2**, 1917-1920.
39. I. Izanzar, M. Dahbi, M. Kiso, S. Doubaji, S. Komaba and I. Saadoune, *Carbon*, 2018, **137**, 165-173.
40. C. Matei Ghimbeu, J. Górka, V. Simone, L. Simonin, S. Martinet and C. Vix-Guterl, *Nano Energy*, 2018, **44**, 327-335.
41. Y. Morikawa, S. Nishimura, R. Hashimoto, M. Ohnuma and A. Yamada, *Advanced Energy Materials*, 2020, **10**, 1903176.
42. Z. Q. Xu, J. H. Liu, C. Chen, H. Potapenko and M. Q. Wu, *Journal of Power Sources*, 2019, **427**, 62-69.
43. C. Bommier, T. W. Surta, M. Dolgos and X. Ji, *Nano Letters*, 2015, **15**, 5888-5892.
44. C. del Mar Saavedra Rios, A. Beda, L. Simonin and C. Matei Ghimbeu, *Hard Carbon for Na-ion Batteries: From Synthesis to Performance and Storage Mechanism. In Na-ion Batteries (eds L. Monconduit and L. Croguennec).* ISTE Ltd 2020. Published by ISTE Ltd and John Wiley & Sons, Inc., 2021.
45. A. Gomez-Martin, J. Martinez-Fernandez, M. Ruttert, M. Winter, T. Placke and J. Ramirez-Rico, *Chemistry of Materials*, 2019, **31**, 7288-7299.
46. S. Qiu, L. Xiao, M. L. Sushko, K. S. Han, Y. Shao, M. Yan, X. Liang, L. Mai, J. Feng, Y. Cao, X. Ai, H. Yang and J. Liu, *Advanced Energy Materials*, 2017, **7**, 1700403.
47. X. Chen, C. Liu, Y. Fang, X. Ai, F. Zhong, H. Yang and Y. Cao, *Carbon Energy*, 2022, **4**, 1133-1150.
48. D. Chen, W. Zhang, K. Luo, Y. Song, Y. Zhong, Y. Liu, G. Wang, B. Zhong, Z. Wu and X. Guo, *Energy & Environmental Science*, 2021, **14**, 2244-2262.
49. J.-Y. Hwang, S.-T. Myung and Y.-K. Sun, *Chem. Soc. Rev*, 2017, **46**, 3529-3614.
50. K. Kubota and S. Komaba, *Journal of The Electrochemical Society*, 2015, **162**, A2538-A2550.
51. Y. Liu, X. Liu, T. Wang, L.-Z. Fan and L. Jiao, *Sustainable Energy & Fuels*, 2017, **1**, 986-1006.
52. M. D. Slater, D. Kim, E. Lee and C. S. Johnson, *Advanced Functional Materials*, 2013, **23**, 947-958.
53. Y. J. Fang, L. F. Xiao, Z. X. Chen, X. P. Ai, Y. L. Cao and H. X. Yang, *Electrochemical Energy Reviews*, 2018, **1**, 294-323.
54. W. Zhang, F. Zhang, F. Ming and H. N. Alshareef, *Energychem*, 2019, **1**.
55. H. Hou, X. Qiu, W. Wei, Y. Zhang and X. Ji, *Advanced Energy Materials*, 2017, **7**, 1602898.

56. D. Saurel, B. Orayech, B. Xiao, D. Carriazo, X. Li and T. Rojo, *Advanced Energy Materials*, 2018, **8**, 1703268.
57. B. Xiao, T. Rojo and X. Li, *ChemSusChem*, 2019, **12**, 133-144.
58. F. Xie, Z. Xu, Z. Guo and M. Titirici, *Progress in Energy*, 2020, **2**, 042002.
59. J. Górka, C. Vix-Guterl and C. Matei Ghimbeu, *C*, 2016, **2**, 24.
60. T. Liu and X. Li, *Materials Technology*, 2019, **34**, 232-245.
61. Y. H. Wan, Y. Liu, D. L. Chao, W. Li and D. Y. Zhao, *Nano Materials Science*, 2023, **5**, 189-201.
62. P. Liu, Y. M. Li, Y. S. Hu, H. Li, L. Q. Chen and X. J. Huang, *Journal of Materials Chemistry A*, 2016, **4**, 13046-13052.
63. B. Tratnik, N. van de Velde, I. Jerman, G. Kapun, E. Tchernychova, M. Tomsic, A. Jamnik, B. Genorio, A. Vizintin and R. Dominko, *Acs Applied Energy Materials*, 2022, **5**, 10667-10679.
64. W. Lv, F. Wen, J. Xiang, J. Zhao, L. Li, L. Wang, Z. Liu and Y. Tian, *Electrochimica Acta*, 2015, **176**, 533-541.
65. Y. H. Zheng, Y. S. Wang, Y. X. Lu, Y. S. Hu and J. Li, *Nano Energy*, 2017, **39**, 489-498.
66. Y. J. Zhang, X. Li, P. Dong, G. Wu, J. Xiao, X. Y. Zeng, Y. J. Zhang and X. L. Sun, *Acs Applied Materials & Interfaces*, 2018, **10**, 42796-42803.
67. Y. H. Zheng, Y. X. Lu, X. G. Qi, Y. S. Wang, L. Q. Mu, Y. M. Li, Q. Ma, J. Li and Y. S. Hu, *Energy Storage Materials*, 2019, **18**, 269-279.
68. D. R. Kumar, I. Kanagaraj, G. Dhakal, A. S. Prakash and J. J. Shim, *Journal of Environmental Chemical Engineering*, 2021, **9**, 105698.
69. K. Kubota, S. Shimadzu, N. Yabuuchi, S. Tominaka, S. Shiraishi, M. Abreu-Sepulveda, A. Manivannan, K. Gotoh, M. Fukunishi, M. Dahbi and S. Komaba, *Chemistry of Materials*, 2020, **32**, 2961-2977.
70. R. Väli, A. Jänes, T. Thomberg and E. Lust, *Electrochimica Acta*, 2017, **253**, 536-544.
71. X. Y. Lin, Y. Z. Liu, H. Tan and B. Zhang, *Carbon*, 2020, **157**, 316-323.
72. Z. R. X. Guan, H. Liu, B. Xu, X. Hao, Z. X. Wang and L. Q. Chen, *Journal of Materials Chemistry A*, 2015, **3**, 7849-7854.
73. N. Daher, D. Huo, C. Davoisne, P. Meunier and R. Janot, *Acs Applied Energy Materials*, 2020, **3**, 6501-6510.
74. Y. Bai, Z. Wang, C. Wu, R. Xu, F. Wu, Y. Liu, H. Li, Y. Li, J. Lu and K. Amine, *ACS Applied Materials & Interfaces*, 2015, **7**, 5598-5604.
75. B. Zhang, C. M. Ghimbeu, C. Laberty, C. Vix-Guterl and J.-M. Tarascon, *Advanced Energy Materials*, 2016, **6**, 1501588.
76. Y. Li, S. Xu, X. Wu, J. Yu, Y. Wang, Y.-S. Hu, H. Li, L. Chen and X. Huang, *Journal of Materials Chemistry A*, 2015, **3**, 71-77.
77. H. Y. Lu, S. F. Sun, L. F. Xiao, J. F. Qian, X. P. Ai, H. X. Yang, A. H. Lu and Y. L. Cao, *Acs Applied Energy Materials*, 2019, **2**, 729-735.
78. J. Choi, M. E. Lee, S. Lee, H. J. Jin and Y. S. Yun, *Acs Applied Energy Materials*, 2019, **2**, 1185-1191.
79. G. Hasegawa, K. Kanamori, N. Kannari, J.-i. Ozaki, K. Nakanishi and T. Abe, *Journal of Power Sources*, 2016, **318**, 41-48.
80. N. Q. Ren, L. F. Wang, X. D. He, L. M. Zhang, J. M. Dong, F. Chen, J. C. Xiao, B. C. Pan and C. H. Chen, *Acs Applied Materials & Interfaces*, 2021, **13**, 46813-46820.
81. J. Xiang, W. Lv, C. Mu, J. Zhao and B. Wang, *Journal of Alloys and Compounds*, 2017, **701**, 870-874.
82. C. Marino, J. Cabanero, M. Povia and C. Villevieille, *J Electrochem Soc*, 2018, **165**, A1400-A1408.
83. X.-S. Wu, X.-L. Dong, B.-Y. Wang, J.-L. Xia and W.-C. Li, *Renewable Energy*, 2022, **189**, 630-638.
84. S. F. Huang, Y. Lv, W. Wen, T. Xue, P. Jia, J. Wang, J. J. Zhang and Y. F. Zhao, *Materials Today Energy*, 2021, **20**, 100673.
85. S. Alvin, D. Yoon, C. Chandra, H. S. Cahyadi, J. H. Park, W. Chang, K. Y. Chung and J. Kim, *Carbon*, 2019, **145**, 67-81.

86. Q. Jiang, Z. H. Zhang, S. Y. Yin, Z. P. Guo, S. Q. Wang and C. Q. Feng, *Applied Surface Science*, 2016, **379**, 73-82.
87. W. Nie, X. L. Liu, Q. M. Xiao, L. X. Li, G. X. Chen, D. Li, M. Zeng and S. W. Zhong, *Chemelectrochem*, 2020, **7**.
88. C.-C. Wang and W.-L. Su, *Surface & Coatings Technology*, 2021, **415**.
89. Q. Wang, X. Zhu, Y. Liu, Y. Fang, X. Zhou and J. Bao, *Carbon*, 2018, **127**, 658-666.
90. X. W. Dou, I. Hasa, D. Saurel, M. Jauregui, D. Buchholz, T. Rojo and S. Passerini, *Chemsuschem*, 2018, **11**, 3276-3285.
91. T. Zhang, J. Mao, X. Liu, M. Xuan, K. Bi, X. L. Zhang, J. Hu, J. Fan, S. Chen and G. Shao, *RSC Advances*, 2017, **7**, 41504-41511.
92. J. Ding, H. Wang, Z. Li, A. Kohandehghan, K. Cui, Z. Xu, B. Zahiri, X. Tan, E. M. Lotfabad, B. C. Olsen and D. Mitlin, *ACS Nano*, 2013, **7**, 11004-11015.
93. P. Wang, B. Qiao, Y. Du, Y. Li, X. Zhou and Z. Dai, *J Phys Chem C*, 2015, **119**, 21336-21344.
94. D. Sun, B. Luo, H. Y. Wang, Y. G. Tang, X. B. Ji and L. Z. Wang, *Nano Energy*, 2019, **64**, 103937.
95. L. F. Xiao, H. Y. Lu, Y. J. Fang, M. L. Sushko, Y. L. Cao, X. P. Ai, H. X. Yang and J. Liu, *Advanced Energy Materials*, 2018, **8**, 1703238.
96. Y. Huang, Y. Q. Wang, P. X. Bai and Y. H. Xu, *Acs Applied Materials & Interfaces*, 2021, **13**, 38441-38449.
97. X. Zhao, Y. Ding, Q. Xu, X. Yu, Y. Liu and H. Shen, *Advanced Energy Materials*, 2019, **9**, 1803648.
98. A. Beda, F. Rabuel, M. Morcrette, S. Knopf, P. L. Taberna, P. Simon and C. Matei Ghimbeu, *J Mater Chem A*, 2021, **9**, 1743-1758
99. L. Yang, M. X. Hu, Q. Lv, H. W. Zhang, W. Yang and R. T. Lv, *Carbon*, 2020, **163**, 288-296.
100. Z. Xu, J. Wang, Z. Y. Guo, F. Xie, H. Y. Liu, H. Yadegari, M. Tebyetekerwa, M. P. Ryan, Y. S. Hu and M. M. Titirici, *Advanced Energy Materials*, 2022, **12**, 2200208.
101. F. Xie, Z. Xu, A. C. S. Jensen, F. X. Ding, H. Au, J. Y. Feng, H. Luo, M. Qiao, Z. Y. Guo, Y. X. Lu, A. J. Drew, Y. S. Hu and M. M. Titirici, *Journal of Materials Chemistry A*, 2019, **7**, 27567-27575.
102. A. F. Qatarneh, C. Dupont, J. Michel, L. Simonin, A. Beda, C. M. Ghimbeu, V. Ruiz-Villanueva, D. da Silva, H. Piegay and M. J. Franca, *Journal of Environmental Chemical Engineering*, 2021, **9**, 106604.
103. C.-C. Wang and W.-L. Su, *Acs Applied Energy Materials*, 2022, **5**, 1052-1064.
104. P. Zheng, T. Liu, X. Y. Yuan, L. F. Zhang, Y. Liu, J. F. Huang and S. W. Guo, *Scientific Reports*, 2016, **6**, 26246.
105. P. Y. Zhao, J. Zhang, Q. Li and C. Y. Wang, *Journal of Power Sources*, 2016, **334**, 170-178.
106. C. F. Ding, L. B. Huang, J. L. Lan, Y. H. Yu, W. H. Zhong and X. P. Yang, *Small*, 2020, **16**, 1906883.
107. L. Zeng, W. Li, J. Cheng, J. Wang, X. Liu and Y. Yu, *RSC Advances*, 2014, **4**, 16920-16927.
108. D. Xu, C. Chen, J. Xie, B. Zhang, L. Miao, J. Cai, Y. Huang and L. Zhang, *Advanced Energy Materials*, 2016, **6**, 1501929.
109. H. D. Asfaw, R. Gond, A. Kotronia, C. W. Tai and R. Younesi, *Sustainable Materials and Technologies*, 2022, **32**, e00407.
110. H. Wang, F. Sun, Z. Qu, K. Wang, L. Wang, X. Pi, J. Gao and G. Zhao, *Acs Sustainable Chemistry & Engineering*, 2019, **7**, 18554-18565.
111. G. Hasegawa, N. Kanamori, J.-I. Ozaki, K. Nakanishi and T. Abe, *ChemElectroChem*, 2015, **2**, 1917-1920.
112. Z. Wang, B. L. Liu, J. Xie, J. D. Hu, Z. J. Lu and Y. L. Cao, *Journal of Alloys and Compounds*, 2022, **911**, 164979.
113. Z. Wei, H. X. Zhao, Y. B. Niu, S. Y. Zhang, Y. B. Wu, H. J. Yan, S. Xin, Y. X. Yin and Y. G. Guo, *Materials Chemistry Frontiers*, 2021, **5**, 3911-3917.
114. G. Zhang, L. Zhang, Q. Ren, L. Yan, F. Zhang, W. Lv and Z. Shi, *Acs Applied Materials & Interfaces*, 2021, **13**, 31650-31659.

115. A. Beda, F. Rabuel, O. Rahmouni, M. Morcrette and C. M. Ghimbeu, *Journal of Materials Chemistry A*, 2023, **11**, 4365-4383.
116. Y. Cao, L. Xiao, M. Sushko, W. Wang, B. Schwenzer, J. Xiao, Z. Nie, L. Saraf, Z. Yang and J. Liu, *Nano Lett*, 2012, **12**, 3783-3787.
117. H. Liu, M. Q. Jia, N. Sun, B. Cao, R. J. Chen, Q. Z. Zhu, F. Wu, N. Qiao and B. Xu, *Acs Applied Materials & Interfaces*, 2015, **7**, 27124-27130.
118. M. Y. Hao, N. Xiao, Y. W. Wang, H. Q. Li, Y. Zhou, C. Liu and J. S. Qiu, *Fuel Processing Technology*, 2018, **177**, 328-335.
119. Y. Li, Y.-S. Hu, H. Li, L. Chen and X. Huang, *Journal of Materials Chemistry A*, 2015, **4**, 96-104.
120. D. Qiu, T. F. Cao, J. Zhang, S. W. Zhang, D. Q. Zheng, H. L. Wu, W. Lv, F. Y. Kang and Q. H. Yang, *Journal of Energy Chemistry*, 2019, **31**, 101-106.
121. S. B. Yang, W. Dong, D. Shen, S. N. Li, W. Sun, X. D. Hong, M. Wang and Y. Q. Mao, *Chemical Engineering Journal*, 2017, **309**, 674-681.
122. Y. F. Du, G. H. Sun, Y. Li, J. Y. Cheng, J. P. Chen, G. Song, Q. Q. Kong, L. J. Xie and C. M. Chen, *Carbon*, 2021, **178**, 243-255.
123. T. K. Kumaresan, S. A. Masilamani, K. Raman, S. Z. Karazhanov and R. Subashchandrabose, *Electrochimica Acta*, 2021, **368**, 137574.
124. K. H. Yu, X. R. Wang, H. Y. Yang, Y. Bai and C. Wu, *Journal of Energy Chemistry*, 2021, **55**, 499-508.
125. L. J. Fu, K. Tang, K. P. Song, P. A. van Aken, Y. Yu and J. Maier, *Nanoscale*, 2014, **6**, 1384-1389.
126. E. Lotfabad, J. Ding, K. Cui, A. Kohandehghan, P. Kalisvaart, M. Hazelton and D. Mitlin, *ASC Nano*, 2014, **8**, 7115-7129.
127. M. Carboni, J. Manzi, A. R. Armstrong, J. Billaud, S. Brutti and R. Younesi, *Chemelectrochem*, 2019, **6**, 1745-1753.
128. L. Wu, D. Buchholz, C. Vaalma, G. A. Giffin and S. Passerini, *ChemElectroChem*, 2016, **3**, 292-298.
129. I. K. Ilic, K. Schutjajew, W. Y. Zhang and M. Oschatz, *Carbon*, 2022, **186**, 55-63.
130. X. Dou, I. Hasa, D. Saurel, C. Vaalma, L. Wu, D. Buchholz, D. Bresser, S. Komaba and S. Passerini, *Materials Today*, 2019, **23**, 87-104.
131. E. Gibertini, F. Liberale, C. Dossi, G. Binda, B. Mattioli, R. Bettinetti, A. Maspero, M. Fiore, R. Ruffo and L. Magagnin, *Journal of Applied Electrochemistry*, 2021, **51**, 1665-1673.
132. Z. Zhu, F. Liang, Z. Zhou, X. Zeng, D. Wang, P. Dong, J. Zhao, S. Sun, Y. Zhang and X. Li, *Journal of Materials Chemistry A*, 2018, **6**, 1513-1522.
133. M. K. Rybarczyk, Y. M. Li, M. Qiao, Y. S. Hu, M. M. Titirici and M. Lieder, *Journal of Energy Chemistry*, 2019, **29**, 17-22.
134. U. Kumar, J. Wu, N. Sharma and V. Sahajwalla, *Energy & Fuels*, 2021, **35**, 1820-1830.
135. C. d. M. S. Rios, L. Simonin, C. M. Ghimbeu, C. Vaulot, D. d. S. Perez and C. Dupont, *Fuel Processing Technology*, 2022, **231**, 107223.
136. R. F. Susanti, S. Alvin and J. Kim, *Journal of Industrial and Engineering Chemistry*, 2020, **91**, 317-329.
137. A. Beda, J. M. Le Meins, P. L. Taberna, P. Simon and C. M. Ghimbeu, *Sustainable Materials and Technologies*, 2020, **26**, e00227.
138. L. Xiao, Y. Cao, W. A. Henderson, M. L. Sushko, Y. Shao, J. Xiao, W. Wang, M. H. Engelhard, Z. Nie and J. Liu, *Nano Energy*, 2016, **19**, 279-288.
139. V. G. Pol, E. Lee, D. H. Zhou, F. Dogan, J. M. Calderon-Moreno and C. S. Johnson, *Electrochimica Acta*, 2014, **127**, 61-67.
140. J. L. Xia, D. Yan, L. P. Guo, X. L. Dong, W. C. Li and A. H. Lu, *Advanced Materials*, 2020, **32**, 2000447.
141. C. Liu, N. Xiao, Y. W. Wang, H. Q. Li, G. Wang, Q. Dong, J. P. Bai, J. Xiao and J. S. Qiu, *Fuel Processing Technology*, 2018, **180**, 173-179.
142. R. Väli, A. Jänes, T. Thomberg and E. Lust, *Journal of The Electrochemical Society*, 2016, **163**, A1619-A1626.
143. Nagmani and S. Puravankara, *Acs Applied Energy Materials*, 2020, **3**, 10045-10052.

144. H.-l. Wang, Z.-q. Shi, J. Jin, C.-b. Chong and C.-y. Wang, *Journal of Electroanalytical Chemistry*, 2015, **755**, 87-91.
145. K. Tang, L. Fu, R. J. White, L. Yu, M.-M. Titirici, M. Antonietti and J. Maier, *Advanced Energy Materials*, 2012, **2**, 873-877.
146. Z. H. Wang, L. Qie, L. X. Yuan, W. X. Zhang, X. L. Hu and Y. H. Huang, *Carbon*, 2013, **55**, 328-334.
147. S. Wang, L. Xia, L. Yu, L. Zhang, H. Wang and X. W. D. Lou, *Advanced Energy Materials*, 2016, **6**, 1502217.
148. S. Wenzel, T. Hara, J. Janek and P. Adelhelm, *Energy & Environmental Science*, 2011, **4**, 3342-3345.
149. Y. Q. Li, Y. X. Lu, Q. S. Meng, A. C. S. Jensen, Q. Q. Zhang, Q. H. Zhang, Y. X. Tong, Y. R. Qi, L. Gu, M. M. Titirici and Y. S. Hu, *Advanced Energy Materials*, 2019, **9**, 1902852.
150. R. S. Babu and M. Pyo, *Journal of the Electrochemical Society*, 2014, **161**, A1045-A1050.
151. L. C. Yue, H. T. Zhao, Z. G. Wu, J. Liang, S. Y. Lu, G. Chen, S. Y. Gao, B. H. Zhong, X. D. Guo and X. P. Sun, *Journal of Materials Chemistry A*, 2020, **8**, 11493-11510.
152. B. A. Zhang, M. Deschamps, M. R. Ammar, E. Raymundo-Pinero, L. Hennet, D. Batuk and J. M. Tarascon, *Advanced Materials Technologies*, 2017, **2**, 1600227.
153. Y. Li, Y.-S. Hu, M.-M. Titirici, L. Chen and X. Huang, *Advanced Energy Materials*, 2016, **6**, 1600659.
154. C. Nita, B. Zhang, J. Dentzer and C. M. Ghimbeu, *Journal of Energy Chemistry*, 2021, **58**, 207-218.
155. H. Yu, Y. H. Wang, Y. Jing, J. M. Ma, C. F. Du and Q. Y. Yan, *Small*, 2019, **15**, 1970133.
156. R. E. Franklin, *Proceedings of the Royal Society of London Series a-Mathematical and Physical Sciences*, 1951, **209**, 196-218.
157. P. J. F. Harris, *Interdisciplinary Science Reviews*, 2001, **26**, 204-210.
158. P. J. F. Harris, *Journal of Materials Science*, 2013, **48**, 565-577.
159. A. P. Terzyk, S. Furmaniak, P. J. F. Harris, P. A. Gauden, J. Wloch, P. Kowalczyk and G. Rychlicki, *Physical Chemistry Chemical Physics*, 2007, **9**, 5919-5927.
160. J. Q. Li, C. Peng, J. Li, J. K. Wang and H. L. Zhang, *Energy & Fuels*, 2022, **36**, 5937-5952.
161. H. K. Cheng, Z. R. Tang, X. Z. Luo and Z. Zheng, *Science of the Total Environment*, 2021, **777**, 146120.
162. W. Luo, Z. L. Jian, Z. Y. Xing, W. Wang, C. Bommier, M. M. Lerner and X. L. Ji, *Acs Central Science*, 2015, **1**, 516-522.
163. D. A. Stevens, 2000.
164. Y. M. Feng, L. Tao, Z. F. Zheng, H. B. Huang and F. Lin, *Energy Storage Materials*, 2020, **31**, 274-309.
165. J. Qian, F. Wu, Y. S. Ye, M. L. Zhang, Y. X. Huang, Y. Xing, W. Qu, L. Li and R. J. Chen, *Advanced Energy Materials*, 2018, **8**, 1703159.
166. L. C. Kong, Y. Li and W. Feng, *Transactions of Tianjin University*, 2022, **28**, 123-131.
167. N. Sun, Z. Guan, Y. Liu, Y. Cao, Q. Zhu, H. Liu, Z. Wang, P. Zhang and B. Xu, *Advanced Energy Materials*, 2019, **9**, 1901351.
168. C. d. M. Saavedra Rios, V. Simone, L. Simonin, S. Martinet and C. Dupont, *Biomass and Bioenergy*, 2018, **117**, 32-37.
169. D. Q. Chen, K. Y. Luo, Z. W. Yang, Y. J. Zhong, Z. G. Wu, Y. Song, G. Chen, G. K. Wang, B. H. Zhong and X. D. Guo, *Carbon*, 2021, **173**, 253-261.
170. P. Thomas and D. Billaud, *Electrochimica Acta*, 2002, **47**, 3303-3307.
171. J. R. Dahn, W. Xing and Y. Gao, *Carbon*, 1997, **35**, 825-830.
172. H. Tonnoir, D. Huo, R. L. S. Canevesi, V. Fierro, A. Celzard and R. Janot, *Materials Today Chemistry*, 2022, **23**, 100614.
173. Z. Tang, S. Y. Zhou, P. F. Wu, H. Wang, Y. C. Huang, Y. M. Zhang, D. Sun, Y. G. Tang and H. Y. Wang, *Chemical Engineering Journal*, 2022, **441**, 135899.
174. A. M. Escamilla-Perez, A. Beda, L. Simonin, M. L. Grapotte, J. M. Le-Meins and C. M. Ghimbeu, *Acs Applied Energy Materials*, 2023, **6**, 7419-7432.
175. Y. Zhen, Y. Chen, F. Li, Z. Guo, Z. Hong and M.-M. Titirici, *Proceedings of the National Academy of Sciences of the United States of America*, 2021, **118**, e2111119118.

176. A. Beda, C. Vaulot and C. M. Ghimbeu, *Journal of Materials Chemistry A*, 2021, **9**, 937-943.
177. D. Saurel, J. Segalini, M. Jauregui, A. Pendashteh, B. Daffos, P. Simon and M. Casas-Cabanas, *Energy Storage Materials*, 2019, **21**, 162-173.
178. M. Thommes, K. Kaneko, A. V. Neimark, J. P. Olivier, F. Rodriguez-Reinoso, J. Rouquerol and K. S. W. Sing, *Pure and Applied Chemistry*, 2015, **87**, 1051–1069.
179. M. Seredych, J. Jagiello and T. J. Bandosz, *Carbon*, 2014, **74**, 207-217.
180. A. Beda, C. Voulot, F. Rabuel, M. Morcrette and C. Matei Ghimbeu, *Energy Advances*, 2022, **1**, 185-190.
181. S. Alvin, H. S. Cahyadi, J. Hwang, W. Chang, S. K. Kwak and J. Kim, *Advanced Energy Materials*, 2020, **10**, 2000283.
182. F. Wu, M. H. Zhang, Y. Bai, X. R. Wang, R. Q. Dong and C. Wu, *Acs Applied Materials & Interfaces*, 2019, **11**, 12554-12561.
183. F. Xie, Z. Xu, A. C. S. Jensen, H. Au, Y. X. Lu, V. Araullo-Peters, A. J. Drew, Y. S. Hu and M. M. Titirici, *Advanced Functional Materials*, 2019, **29**, 1901072.
184. Y. Li, M. P. Paranthaman, K. Akato, A. K. Naskar, A. M. Levine, R. J. Lee, S.-O. Kim, J. Zhang, S. Dai and A. Manthiram, *Journal of Power Sources*, 2016, **316**, 232-238.
185. E. Irisarri, N. Amini, S. Tennison, C. M. Ghimbeu, J. Gorka, C. Vix-Guterl, A. Ponrouch and M. R. Palacin, *Journal of The Electrochemical Society*, 2018, **165**, A4058-A4066.
186. E. Irisarri, A. Ponrouch and M. R. Palacin, *Journal of The Electrochemical Society*, 2015, **162**, A2476-A2482.
187. S. Guo, Y. M. Chen, L. P. Tong, Y. Cao, H. Jiao, Z. Long and X. Q. Qiu, *Electrochimica Acta*, 2022, **410**, 140017.
188. Y. C. Zhen, Y. Chen, F. Li, Z. Y. Guo, Z. S. Hong and M. M. Titirici, *Proceedings of the National Academy of Sciences of the United States of America*, 2021, **118**, e2111119118.
189. A. Beda, A. M. Escamilla-Perez, L. Simonin and C. M. Ghimbeu, *Acs Applied Energy Materials*, 2022, **5**, 4774-4787.
190. C. D. S. Rios, L. Simonin, A. de Geyer, C. M. Ghimbeu and C. Dupont, *Energies*, 2020, **13**, 3513.
191. N. Sun, J. Qiu and B. Xu, *Advanced Energy Materials*, 2022, **12**, 2200715.
192. K. Wang, F. Sun, H. Wang, D. Wu, Y. Chao, J. Gao and G. Zhao, *Advanced Functional Materials*, 2022, **32**, 2203725.
193. Q. S. Meng, Y. X. Lu, F. X. Ding, Q. Q. Zhang, L. Q. Chen and Y. S. Hu, *Acs Energy Letters*, 2019, **4**, 2608–2612.
194. S. Y. Zhou, Z. Tang, Z. Y. Pan, Y. C. Huang, L. Zhao, X. Zhang, D. Sun, Y. G. Tang, A. S. Dhmees and H. Y. Wang, *Susmat*, 2022, **2**, 357-367.
195. 2016.
196. K. Wang, Y. Xu, Y. Li, V. Dravid, J. Wu and Y. Huang, *Journal of Materials Chemistry A*, 2019, **7**, 3327-3335.
197. N. Sun, H. Liu and B. Xu, *Journal of Materials Chemistry A*, 2015, **3**, 20560-20566.
198. B. Yang, J. Wang, Y. Zhu, K. Ji, C. Wang, D. Ruan and Y. Xia, *Journal of Power Sources*, 2021, **492**, 229656.
199. Y. Y. Zhu, M. M. Chen, Q. Li, C. Yuan and C. Y. Wang, *Carbon*, 2017, **123**, 727-734.
200. K. L. Hong, L. Qie, R. Zeng, Z. Q. Yi, W. Zhang, D. Wang, W. Yin, C. Wu, Q. J. Fan, W. X. Zhang and Y. H. Huang, *Journal of Materials Chemistry A*, 2014, **2**, 12733-12738.
201. N. Li, Q. Y. Yang, Y. X. Wei, R. C. Rao, Y. P. Wang, M. L. Sha, X. H. Ma, L. L. Wang and Y. T. Qian, *Journal of Materials Chemistry A*, 2020, **8**, 20486-20492.
202. S. Alvin, C. Chandra and J. Kim, *Chemical Engineering Journal*, 2020, **391**, 123576.
203. L. A. Romero-Cano, H. Garcia-Rosero, F. Carrasco-Marin, A. F. Perez-Cadenas, L. V. Gonzalez-Gutierrez, A. I. Zarate-Guzman and G. Ramos-Sanchez, *Electrochimica Acta*, 2019, **326**, 134973.
204. Y. Wang, Y. Li, S. S. Mao, D. X. Ye, W. Liu, R. Guo, Z. H. Feng, J. L. Kong and J. Y. Xie, *Sustainable Energy & Fuels*, 2019, **3**, 717-722.
205. Z. Li, C. Bommier, Z. S. Chong, Z. Jian, T. W. Surta, X. Wang, Z. Xing, J. C. Neuefeind, W. F. Stickle, M. Dolgos, P. A. Greaney and X. Ji, *Advanced Energy Materials*, 2017, **7**, 1602894.

206. R. Muruganantham, F. M. Wang and W. R. Liu, *Electrochimica Acta*, 2022, **424**.
207. P. Brender, R. Gadiou, J. C. Rietsch, P. Fioux, J. Dentzer, A. Ponche and C. Vix-Guterl, *Anal. Chem*, 2012, **84**, 2147-2153.
208. J. L. Figueiredo, M. F. R. Pereira, M. M. A. Freitas and J. J. M. Órfão, *Carbon*, 1999, **37**, 1379-1389.
209. F. Salvador, M. J. Sanchez-Montero, A. Salvador and M. J. Martin, *Applied Surface Science*, 2005, **252**, 641-646.
210. J. H. Zhou, Z. J. Sui, J. Zhu, P. Li, D. Chen, Y. C. Dai and W. K. Yuan, *Carbon*, 2007, **45**, 785-796.
211. M. S. Shafeeyan, W. M. A. W. Daud, A. Houshmand and A. Shamiri, *Journal of Analytical and Applied Pyrolysis*, 2010, **89**, 143-151.
212. N. Li, X. Ma, Q. Zha, K. Kim, Y. Chen and C. Song, *Carbon*, 2011, **49**, 5002-5013.
213. A. Beda, C. Villevieille, P. L. Taberna, P. Simon and C. M. Ghimbeu, *Journal of Materials Chemistry A*, 2020, **8**, 5558-5571.
214. E. Olsson, J. Cottom and Q. Cai, *Small*, 2021, **17**, 2007652.
215. S. M. Lee, J. H. Kim and J. H. Ahn, *Materials Today*, 2015, **18**, 336-344.
216. J. Ma, D. Alfe, A. Michaelides and E. Wang, *Physical Review B*, 2009, **80**, 033407.
217. S. Malola, H. Hakkinen and P. Koskinen, *Physical Review B*, 2010, **81**, 165447.
218. M. D. Bhatt, H. Kim and G. Kim, *Rsc Advances*, 2022, **12**, 21520-21547.
219. X. Wang, J. Chen, C. Dong, D. Wang and Z. Mao, *Chemelectrochem*, 2022, **9**, e202101613.
220. Y. Youn, B. Gao, A. Kamiyama, K. Kubota, S. Komaba and Y. Tateyama, *Npj Computational Materials*, 2021, **7**, 48.
221. A. C. Ferrari, *Solid State Communications*, 2007, **143**, 47-57.
222. A. C. Ferrari and J. Robertson, *Physical Review B*, 2000, **61**, 14095 -14107.
223. R. Beams, L. G. Cancado and L. Novotny, *Journal of Physics-Condensed Matter*, 2015, **27**, 083002.
224. M. S. Dresselhaus, A. Jorio, A. G. Souza Filho and R. Saito, *Philosophical Transactions of the Royal Society a-Mathematical Physical and Engineering Sciences*, 2010, **368**, 5355-5377.
225. L. G. Cancado, A. Jorio, E. H. Martins Ferreira, F. Stavale, C. A. Achete, R. B. Capaz, M. V. O. Moutinho, A. Lombardo, T. S. Kulmala and A. C. Ferrari, *Nano Letters*, 2011, **11**, 3190-3196.
226. A. Sadezky, H. Muckenhuber, H. Grothe, R. Niessner and U. Poschl, *Carbon*, 2005, **43**, 1731-1742.
227. S. Tao, W. Xu, J. Zheng, F. Kong, P. Cui, D. Wu, B. Qian, S. Chen and L. Song, *Carbon*, 2021, **178**, 233-242.
228. L. Xiao, H. Lu, Y. Fang, M. L. Sushko, Y. Cao, X. Ai, H. Yang and J. Liu, *Advanced Energy Materials*, 2018, **8**, 1703238.
229. X. K. Wang, J. Shi, L. W. Mi, Y. P. Zhai, J. Y. Zhang, X. M. Feng, Z. J. Wu and W. H. Chen, *Rare Metals*, 2020, **39**, 1053-1062.
230. D. Y. Wu, F. Sun, Z. B. Qu, H. Wang, Z. J. Lou, B. Wu and G. B. Zhao, *Journal of Materials Chemistry A*, 2022, **10**, 17225-17236.
231. N. T. Aristote, C. Liu, X. L. Deng, H. Q. Liu, J. Q. Gao, W. T. Deng, H. S. Hou and X. B. Ji, *Journal of Electroanalytical Chemistry*, 2022, **923**, 116769.
232. A. Agrawal, S. Janakiraman, K. Biswas, A. Venimadhav, S. K. Srivastava and S. Ghosh, *Electrochimica Acta*, 2019, **317**, 164-172.
233. Y. Z. Zhang, L. Chen, Y. Meng, X. P. Li, Y. Guo and D. Xiao, *Rsc Advances*, 2016, **6**, 110850-110857.
234. H. Wan, X. Shen, H. Jiang, C. Zhang, K. Jiang, T. Chen, L. Shi, L. Dong, C. He, Y. Xu, J. Li and Y. Chen, *Energy*, 2021, **231**, 121102.
235. H. S. Yang, S. W. Kim, K. H. Kim, S. H. Yoon, M. J. Ha and J. Kang, *Applied Sciences-Basel*, 2021, **11**, 12007.
236. K. W. Lu, S. Lu, T. T. Gu, X. J. Zheng, K. Ke, X. W. Li and R. Z. Yang, *Electrochemistry Communications*, 2019, **103**, 22-26.
237. D. C. Qin, Z. Y. Liu, Y. Z. Zhao, G. Y. Xu, F. Zhang and X. G. Zhang, *Carbon*, 2018, **130**, 664-671.

238. C. Vix-Guterl, M. Couzi, J. Dentzer, M. Trinquecoste and P. Delhaes, *Journal of Physical Chemistry B*, 2004, **108**, 19361-19367.
239. N. R. Laine, F. J. Vastola and J. P. L. Walker, *J. Phys. Chem*, 1963, **67**, 2030-2034.
240. P.-C. Tsai, S.-C. Chung, S.-K. Lin and A. Yamada, *J. Mater. Chem. A*, 2015, **3**, 9763-9768.
241. X. Dou, C. Geng, D. Buchholz and S. Passerini, *APL Materials*, 2018, **6**, 047501.
242. X. Meng, P. E. Savage and D. Deng, *Environmental Science & Technology*, 2015, **49**, 12543-12550.
243. G. Q. Zou, Z. D. Huang, G. G. Zhao, S. M. Li, H. S. Hou, X. Q. Qiu and X. B. Ji, *Journal of the Electrochemical Society*, 2017, **164**, A1431-A1437.
244. M. Dar, K. Majid and M. Wahid, *Journal of Electroanalytical Chemistry*, 2021, **899**, 115669.
245. T. Y. Lyu, X. X. Lan, L. Z. Liang, X. Lin, C. Hao, Z. Y. Pan, Z. Q. Tian and P. K. Shen, *Electrochimica Acta*, 2021, **365**, 137356.
246. Z. E. Yu, Y. C. Lyu, Y. T. Wang, S. Y. Xu, H. Y. Cheng, X. Y. Mu, J. Q. Chu, R. M. Chen, Y. Liu and B. K. Guo, *Chemical Communications*, 2020, **56**, 778-781.
247. X. Lin, X. Du, P. S. Tsui, J.-Q. Huang, H. Tan and B. Zhang, *Electrochimica Acta*, 2019, **316**, 60-68.
248. C. C. Wang and W. L. Su, *Acs Applied Energy Materials*, 2022, **5**, 1052-1064.
249. W. F. Jing, M. Wang, Y. Li, H. R. Li, H. N. Zhang, S. L. Hu, H. Q. Wang and Y. B. He, *Electrochimica Acta*, 2021, **391**, 139000.
250. Z. Y. Zhu, W. T. Zhong, Y. J. Zhang, P. Dong, S. G. Sun, Y. J. Zhang and X. Li, *Carbon Energy*, 2021, **3**, 541-553.
251. J. Ding, Y. Zhang, Y. D. Huang, X. C. Wang, Y. Sun, Y. Guo, D. Z. Jia and X. C. Tang, *Journal of Alloys and Compounds*, 2021, **851**, 156791.
252. D. Yan, C. Y. Yu, X. J. Zhang, W. Qin, T. Lu, B. W. Hu, H. L. Li and L. K. Pan, *Electrochimica Acta*, 2016, **191**, 385-391.
253. H. Bensouda, C. Hakim, H. Aziam, A. Bacaoui and I. Saadoune, Mohammed VI Polytechn Univ, Benguerir, MOROCCO, 2020.
254. P. C. Rath, J. Patra, H. T. Huang, D. Bresser, T. Y. Wu and J. K. Chang, *Chemsuschem*, 2019, **12**, 2302-2309.
255. D. Yoon, J. Hwang, W. Chang and J. Kim, *Acs Applied Materials & Interfaces*, 2018, **10**, 569-581.
256. S. Alvin, C. Chandra and J. Kim, *Chemical Engineering Journal*, 2021, **411**, 128490.
257. G. Lee, M. E. Lee, S.-S. Kim, H.-I. Joh and S. Lee, *Journal of Industrial and Engineering Chemistry*, 2022, **105**, 268-277.
258. L. Qie, W. Chen, X. Xiong, C. Hu, F. Zou, P. Hu and Y. Huang, *Advanced Science*, 2015, **2**, 1500195.
259. H. Zhang, W. Zhang and F. Huang, *Chemical Engineering Journal*, 2022, **434**, 134503.
260. Y. Y. Xue, X. Guo, H. F. Zhou and J. S. Zhou, *Carbon*, 2019, **154**, 219-229.
261. M. X. Hu, L. Yang, K. Zhou, C. S. Zhou, Z. H. Huang, F. Y. Kang and R. T. Lv, *Carbon*, 2017, **122**, 680-686.
262. S. M. Hong, V. Etacheri, C. N. Hong, S. W. Choi, K. B. Lee and V. G. Pol, *Acs Applied Materials & Interfaces*, 2017, **9**, 18790-18798.
263. Z. Yuan, L. Si and X. Zhu, *Journal of Materials Chemistry A*, 2015, **3**, 23403-23411.
264. Hard carbon - BSHC series, https://www.btrchina.com/en/NegativeProducts/info.aspx?itemid=1063).
265. J. Zhao, L. W. Zhao, K. Chihara, S. Okada, J. Yamaki, S. Matsumoto, S. Kuze and K. Nakane, *Journal of Power Sources*, 2013, **244**, 752-757.
266. T. Yamamoto, T. Yamaguchi, T. Nohira, R. Hagiwara, A. Fukunaga, S. Sakai and K. Nitta, *Electrochemistry*, 2017, **85**, 391-396.
267. High-performance Anode Material, CARBOTRON®P, https://www.kureha.co.jp/development/story/pdf/catalog_hc_eg_20120924.pdf, (accessed 16/01/2024, 2024).
268. Hard carbon anode materials, JFE Chemical Corporation, https://www.jfe-chem.com/en/product/battery/carbon/, (accessed 16/01/2024, 2024).

269. F. Linsenmann, D. Pritzl and H. A. Gasteiger, *Journal of the Electrochemical Society*, 2021, **168**, 010506.
270. KURANODE ™ BIOHARDCARBON, https://www.calgoncarbon.com/app/uploads/KN-brochure-EN-002.pdf, (accessed 16/01/2024, 2024).
271. Hard Carbon, BSG Best Graphite, http://www.cdbsg.com/index/news/detail.html?id=127&cid=15&pid=3, (accessed 16/01/2024, 2024).
272. X. W. Zhong, Y. Z. Li, L. Z. Zhang, J. Tang, X. N. Li, C. Liu, M. M. Shao, Z. G. Lu, H. Pan and B. M. Xu, *Acs Applied Materials & Interfaces*, 2019, **11**, 2970-2977.
273. Q. W. Meng, B. Y. Chen, W. B. Jian, X. S. Zhang, S. R. Sun, T. J. Wang and W. L. Zhang, *Journal of Power Sources*, 2023, **581**, 233475.
274. H. Alptekin, H. Au, A. C. S. Jensen, E. Olsson, M. Goktas, T. F. Headen, P. Adelhelm, Q. Cai, A. J. Drew and M. M. Titirici, *Acs Applied Energy Materials*, 2020, **3**, 9918-9927.
275. H. Au, H. Alptekin, A. C. S. Jensen, E. Olsson, C. A. O'Keefe, T. Smith, M. Crespo-Ribadeneyra, T. F. Headen, C. P. Grey, Q. Cai, A. J. Drew and M. M. Titirici, *Energy & Environmental Science*, 2020, **13**, 3469-3479.
276. P. Bai, Y. He, X. Zou, X. Zhao, P. Xiong and Y. Xu, *Advanced Energy Materials*, 2018, **8**, 1703217.
277. Z. V. Bobyleva, O. A. Drozhzhin, K. A. Dosaev, A. Kamiyama, S. V. Ryazantsev, S. Komaba and E. V. Antipov, *Electrochimica Acta*, 2020, **354**, 136647.
278. D. A. Stevens and J. R. Dahn, *Journal of The Electrochemical Society*, 2000, **147**, 1271-1273.
279. M. Thompson, Q. Xia, Z. Hu and X. S. Zhao, *Materials Advances*, 2021, **2**, 5881-5905.
280. C. del Mar Saavedra Rios, L. Simonin, A. de Geyer, C. Matei Ghimbeu and C. Dupont, *Energies*, 2020, **13(14)**, 3513.
281. H. Kim, J. C. Hyun, D. Kim, J. H. Kwak, J. B. Lee, J. H. Moon, J. Choi, H. D. Lim, S. J. Yang, H. M. Jin, D. J. Ahn, K. Kang, H. J. Jin, H. K. Lim and Y. S. Yun, *Advanced Materials*, 2023, **35**, 2209128.
282. M. Yuan, B. Cao, H. Liu, C. Y. Meng, J. P. Wu, S. Zhang, A. Li, X. H. Chen and H. H. Song, *Chemistry of Materials*, 2022, **34**, 3489-3500.
283. L. K. Iglesias, E. N. Antonio, T. D. Martinez, L. Zhang, Z. Q. Zhuo, S. J. Weigand, J. H. Guo and M. F. Toney, *Advanced Energy Materials*, 2023, DOI: 10.1002/aenm.202302171, 2302171.
284. D. Stevens and J. Dahn, *J Electrochem. Soc*, 2000, **147**, 1271-1273.
285. S. Komaba, W. Murata, T. Ishikawa, N. Yabuuchi, T. Ozeki, T. Nakayama, A. Ogata, K. Gotoh and K. Fujiwara, *Advanced Functional Materials*, 2011, **21**, 3859-3867.
286. J. M. Stratford, P. K. Allan, O. Pecher, P. A. Chater and C. P. Grey, *Chemical Communications*, 2016, **52**, 12430-12433.
287. K. Gotoh, T. Ishikawa, S. Shimadzu, N. Yabuuchi, S. Komaba, K. Takeda, A. Goto, K. Deguchi, S. Ohki, K. Hashi, T. Shimizu and H. Ishida, *Journal of Power Sources*, 2013, **225**, 137-140.
288. R. Morita, K. Gotoh, K. Kubota, S. Komaba, K. Hashi, T. Shimizu and H. Ishida, *Carbon*, 2019, **145**, 712-715.
289. B. Key, R. Bhattacharyya, M. Morcrette, V. Seznec, J. M. Tarascon and C. P. Grey, *Journal of the American Chemical Society*, 2009, **131**, 9239-9249.
290. K. Gotoh, *Batteries & Supercaps*, 2021, **4**, 1267-1278.
291. Y. Cao, L. Xiao, M. L. Sushko, W. Wang, B. Schwenzer, J. Xiao, Z. Nie, L. V. Saraf, Z. Yang and J. Liu, *Nano Letters*, 2012, **12**, 3783-3787.
292. M. A. Reddy, M. Helen, A. Gross, M. Fichtner and H. Euchner, *Acs Energy Letters*, 2018, **3**, 2851-2857.
293. X. Y. Chen, J. Y. Tian, P. Li, Y. L. Fang, Y. J. Fang, X. M. Liang, J. W. Feng, J. Dong, X. P. Ai, H. X. Yang and Y. L. Cao, *Advanced Energy Materials*, 2022, **12**, 2200886.
294. E. Peled, *Journal of the Electrochemical Society*, 1979, **126**, 2047-2051.
295. S. Komaba, T. Ishikawa, N. Yabuuchi, W. Murata, A. Ito and Y. Ohsawa, *Acs Applied Materials & Interfaces*, 2011, **3**, 4165-4168.

296. M. Moshkovich, Y. Gofer and D. Aurbach, *Journal of the Electrochemical Society*, 2001, **148**, E155-E167.
297. R. Mogensen, D. Brandell and R. Younesi, *ACS Energy Letters*, 2016, **1**, 1173-1178.
298. F. A. Soto, P. F. Yan, M. H. Engelhard, A. Marzouk, C. M. Wang, G. L. Xu, Z. H. Chen, K. Amine, J. Liu, V. L. Sprenkle, F. El-Mellouhi, P. B. Balbuena and X. L. Li, *Advanced Materials*, 2017, **29**, 1606860.
299. M. Dahbi, T. Nakano, N. Yabuuchi, S. Fujimura, K. Chihara, K. Kubota, J.-Y. Son, Y.-T. Cui, H. Oji and S. Komaba, *ChemElectroChem*, 2016, **3**, 1856-1867.
300. G. G. Eshetu, T. Diemant, M. Hekmatfar, S. Grugeon, R. J. Behm, S. Laruelle, M. Armand and S. Passerini, *Nano Energy*, 2019, **55**, 327-340.
301. J. Fondard, E. Irisarri, C. Courreges, M. R. Palacin, A. Ponrouch and R. Dedryvere, *Journal of the Electrochemical Society*, 2020, **167**, 070526.
302. Y. Pan, Y. Z. Zhang, B. S. Parimalam, C. C. Nguyen, G. L. Wang and B. L. Lucht, *Journal of Electroanalytical Chemistry*, 2017, **799**, 181-186.
303. B. Philippe, R. Dedryvère, J. Allouche, F. Lindgren, M. Groi, H. Rensmo, F. Gonbeau and K. Edstrom, *Chem Mater*, 2012, **24**, 1107-1115.
304. A. Ponrouch, E. Marchante, M. Courty, J.-M. Tarascon and M. R. Palacín, *Energy & Environmental Science*, 2012, **5**, 8572-8583.
305. R. Dugas, A. Ponrouch, G. Gachot, R. David, M. R. Palacin and J. M. Tarascon, *Journal of the Electrochemical Society*, 2016, **163**, A2333-A2339.
306. L. A. Ma, A. J. Naylor, L. Nyholm and R. Younesi, *Angewandte Chemie-International Edition*, 2021, **60**, 4855-4863.
307. C. Bommier and X. Ji, *Small*, 2018, **14**, 1703576.
308. A. Ponrouch, A. Goni and R. Palacin, *Electrochemistry Communications*, 2013, **27**, 85-88.
309. D. I. Iermakova, R. Dugas, M. R. Palacín and A. Ponrouch, *Journal of The Electrochemical Society*, 2015, **162**, A7060-A7066.
310. C. Bommier, D. Leonard, Z. L. Jian, W. F. Stickle, P. A. Greaney and X. L. Ji, *Advanced Materials Interfaces*, 2016, **3**, 1600449.
311. M. Mandl, J. Becherer, D. Kramer, R. Monig, T. Diemant, R. J. Behm, M. Hahn, O. Bose and M. A. Danzer, *Electrochimica Acta*, 2020, **354**, 136698.
312. A. Bouibes, N. Takenaka, T. Fujie, K. Kubota, S. Komaba and M. Nagaoka, *Acs Applied Materials & Interfaces*, 2018, **10**, 28525-28532.
313. H. Yildirim, A. Kinaci, M. K. Y. Chan and J. P. Greeley, *Acs Applied Materials & Interfaces*, 2015, **7**, 18985-18996.
314. Z. H. Lin, Q. B. Xia, W. L. Wang, W. S. Li and S. L. Chou, *Infomat*, 2019, **1**, 376-389.
315. A. Ponrouch, R. Dedryvère, D. Monti, A. E. Demet, J. M. A. Mba, L. Croguennec, C. Masquelier, P. Johansson and M. R. Palacín, *Energy & Environmental Science*, 2013, **6**, 2361-2369.
316. Y. E. Zhu, L. P. Yang, X. L. Zhou, F. Li, J. P. Wei and Z. Zhou, *Journal of Materials Chemistry A*, 2017, **5**, 9528-9532.
317. P. M. L. Le, T. D. Vo, H. L. Pan, Y. Jin, Y. He, X. Cao, H. V. Nguyen, M. H. Engelhard, C. M. Wang, J. Xiao and J. G. Zhang, *Advanced Functional Materials*, 2020, **30**, 2001151.
318. Y. M. Feng, L. Tao, Y. H. He, Q. Jin, C. G. Kuai, Y. W. Zheng, M. Q. Li, Q. P. Hou, Z. F. Zheng, F. Lin and H. B. Huang, *Journal of Materials Chemistry A*, 2019, **7**, 26954-26965.
319. Y. Jin, Y. B. Xu, P. M. L. Le, T. D. Vo, Q. Zhou, X. G. Qi, M. H. Engelhard, B. E. Matthews, H. Jia, Z. M. Nie, C. J. Niu, C. M. Wang, Y. S. Hu, H. L. Pan and J. G. Zhang, *Acs Energy Letters*, 2020, **5**, 3212-3220.
320. K. Westman, R. Dugas, P. Jankowski, W. Wieczorek, G. Gachot, M. Morcrette, E. Irisarri, A. Ponrouch, M. R. Palacin, J. M. Tarascon and P. Johansson, *Acs Applied Energy Materials*, 2018, **1**, 2671-2680.
321. L. H. B. Nguyen, P. S. Camacho, J. Fondard, D. Carlier, L. Croguennec, M. R. Palacin, A. Ponrouch, C. Courrèges, R. Dedryvère, K. Trad, C. Jordy, S. Genies, Y. Reynier and L. Simonin, *Journal of Power Sources*, 2022, **529**, 231253.

322. T. Broux, F. Fauth, N. Hall, Y. Chatillon, M. Bianchini, T. Bamine, J. B. Leriche, E. Suard, D. Carlier, Y. Reynier, L. Simonin, C. Masquelier and L. Croguennec, *Small Methods*, 2019, **3**, 1800215.
323. R. Dugas, B. Zhang, P. Rozier and J. M. Tarascon, *Journal of The Electrochemical Society*, 2016, **163**, A867-A874.
324. M. E. Lee, H. W. Kwak, H. J. Jin and Y. S. Yun, *Acs Sustainable Chemistry & Engineering*, 2019, **7**, 12734-12740.
325. S. Mariyappan, T. Marchandier, F. Rabuel, A. Iadecola, G. Rousse, A. V. Morozov, A. M. Abakumov and J. M. Tarascon, *Chemistry of Materials*, 2020, **32**, 1657-1666.
326. J. Barker, R. J. Heap, N. Roche, C. Tan, R. Sayers, J. Whitley and Y. Liu, 2016.
327. W. Shao, H. Shi, X. Jian, Z.-S. Wu and F. Hu, *Advanced Energy and Sustainability Research*, 2022, **3**, 2200009.
328. J. Song, L. Wang, Y. H. Lu, J. Liu, B. K. Guo, P. H. Xiao, J. J. Lee, X. Q. Yang, G. Henkelman and J. B. Goodenough, *Journal of the American Chemical Society*, 2015, **137**, 2658-2664.
329. L. Wang, J. Song, R. M. Qiao, L. A. Wray, M. A. Hossain, Y. D. Chuang, W. L. Yang, Y. H. Lu, D. Evans, J. J. Lee, S. Vail, X. Zhao, M. Nishijima, S. Kakimoto and J. B. Goodenough, *Journal of the American Chemical Society*, 2015, **137**, 2548-2554.
330. C. Q. X. Lim and Z. K. Tan, *Acs Applied Energy Materials*, 2021, **4**, 6214-6220.
331. M. S. Qin, W. H. Ren, R. X. Jiang, Q. Li, X. H. Yao, S. Q. Wang, Y. You and L. Q. Mai, *Acs Applied Materials & Interfaces*, 2021, **13**, 3999-4007.
332. J. Abou-Rjeily, I. Bezza, N. A. Laziz, C. Autret-Lambert, M. T. Sougrati and F. Ghamouss, *Energy Storage Materials*, 2020, **26**, 423-432.
333. J. M. Tarascon, *Joule*, 2020, **4**, 1616-1620.
334. Sodium-ion Battery Market Analysis - Industry Report - Trends, Size & Share, https://www.mordorintelligence.com/industry-reports/sodium-ion-battery-market, (accessed 23/03, 2023).
335. B. Editors, The World’s First 1 MWh Na-Ion Battery for Solar Energy Storage and Smart Microgrid System are Operating, https://medium.com/batterybits/news-the-worlds-first-1-mwh-na-ion-battery-for-solar-energy-storage-and-smart-microgrid-system-4ef14699063c, (accessed 29/08/2023, 2023).
336. M. Pasta, C. D. Wessells, N. Liu, J. Nelson, M. T. McDowell, R. A. Huggins, M. F. Toney and Y. Cui, *Nature Communications*, 2014, **5**, 3007.
337. Faradion, the world leader in sodium-ion battery technology, announces a collaboration and licensing deal with AMTE Power, https://faradion.co.uk/faradion-the-world-leader-in-sodium-ion-battery-technology-announces-a-collaboration-and-licensing-deal-with-amte-power/, (accessed 23/03, 2023).
338. Tiamat, http://www.tiamat-energy.com/, (accessed 23/03, 2023).
339. Tiamat Energy, https://www.linkedin.com/company/tiamat-energy/, (accessed 12/02/2024, 2024).
340. CATL Unveils Its Latest Breakthrough Technology by Releasing Its First Generation of Sodium-ion Batteries, https://www.catl.com/en/news/665.html, (accessed 23/03, 2023).
341. Hina Battery becomes 1st battery maker to put sodium-ion batteries in EVs in China, https://cnevpost.com/2023/02/23/hina-battery-puts-sodium-ion-batteries-in-sehol-e10x/, (accessed 23/03, 2023).
342. Electric car featuring sodium ion battery unveiled, https://www.chinadaily.com.cn/a/202302/23/WS63f76b55a31057c47ebb0873.html, (accessed 23/03, 2023).
343. First Faradion battery installed in Australia - Faradion, https://faradion.co.uk/first-faradion-battery-installed-in-australia/, (accessed 23/03, 2023).
344. HOME | NAIMA project, https://naimaproject.eu/, (accessed 23/03, 2023).
345. Natron Energy, https://natron.energy/product/, (accessed 23/03, 2023).
346. L. Zhao, T. Zhang, W. Li, T. Li, L. Zhang, X. Zhang and Z. Wang, *Engineering*, 2023, **24**, 172-183.
347. S. Y. Xu, X. Y. Wu, Y. M. Li, Y. S. Hu and L. Q. Chen, *Chinese Physics B*, 2014, **23**, 118202.